TAMPEREEN TEKNILLINEN YLIOPISTO
TAMPERE UNIVERSITY OF TECHNOLOGY

Jarkko Ojala

Monte Carlo Simulations in Quality Assurance of Dosimetry and Clinical Dose Calculations in Radiotherapy

Julkaisu 1225 • Publication 1225

Tampere 2014

Tampereen teknillinen yliopisto. Julkaisu 1225
Tampere University of Technology. Publication 1225

Jarkko Ojala

Monte Carlo Simulations in Quality Assurance of Dosimetry and Clinical Dose Calculations in Radiotherapy

Thesis for the degree of Doctor of Science in Technology to be presented with due permission for public examination and criticism in Tietotalo Building, Auditorium TB109, at Tampere University of Technology, on the 1st of August 2014, at 12 noon.

Tampereen teknillinen yliopisto - Tampere University of Technology
Tampere 2014

ISBN 978-952-15-3317-4 (printed)
ISBN 978-952-15-3326-6 (PDF)
ISSN 1459-2045

ABSTRACT

The status of radiotherapy as an important treatment modality for cancer is indisputable. In external beam radiotherapy, usually delivered with linear accelerators (linacs), there is a total uncertainty involved in the treatment process, in which the accuracy of the dose calculation is a significant factor. In patient dose calculation, the radiation beam produced by the linac is modelled and delivered to the calculation phantom, which is based on computed tomography (CT) datasets. Most of the clinical dose calculation algorithms implemented in treatment planning systems (TPSs) have been based on analytical or semi-analytical principles, but statistical Monte Carlo (MC) methods have been shown to provide the most accurate representation of dose distributions in the patient and other calculation phantoms. However, long calculation times have prohibited the implementation of full MC methods to clinical patient dose calculation.

In this study, the aim was to develop a full MC-based dose calculation tool to serve as a reference method for TPS dose calculation algorithm benchmarking, but also for dosimetry purposes. The MC-based model constructed for both photon and electron beams was first benchmarked against measurements in water. Finally, the value of the absolute dose calibrated MC model was assessed by applying it to specific problems in dosimetry and dose calculations.

The performance of the MC model in this study in a water phantom was shown to be equal or better than that reported in other studies. During the stage in which the multileaf collimator (MLC) part of the MC model was benchmarked, the MC-based results were used to assess the performance of various measurement detectors in small aperture dosimetry. Eventually, the MC model was shown to provide reference dose distributions both in virtual and CT-based phantom geometries, where accurate measurements are difficult or impossible to perform. With photon beams, the MC model was used to benchmark the TPS algorithms in cases where large uncertainties have been reported, i.e. in the stereotactic body radiotherapy (SBRT) of the lung and in the presence of high atomic number material as a metallic hip implant. With electron beams, the MC model was applied to assess the accuracy of the TPS algorithms in chest wall radiotherapy.

With the described use, in addition to performed TPS configuration data validation, the MC model has the potential to have a positive influence on the total uncertainty involved in radiotherapy. Furthermore, the MC model can be used in the development of new treatment techniques, protocols and detectors for dosimetry and dose calculation algorithms. The time when full MC-based calculations are implemented into clinical treatment planning is yet to come.

ACKNOWLEDGEMENTS

The work presented in this thesis was carried out at the Unit of Radiotherapy, Department of Oncology, Tampere University Hospital between 2009 and 2014. The Monte Carlo simulations were performed at the Tampere Center of Scientific Computing (TCSC), Tampere University of Technology (TUT).

I want to express my deepest gratitude to my supervisors, Docent Simo Hyödynmaa, chief physicist and Docent Maunu Pitkänen, department chief physicist. Without their positive attitude towards my initiative on the topic in 2009, guidance throughout the research, and support whenever it was needed, this work would never have been finished. I am also very grateful to Professor Hannu Eskola for encouragement and administrative support over the years.

I am indebted to all my co-authors for their invaluable contribution to my work over the years. I especially want to thank Petri Sipilä M.Sc., senior inspector at STUK (Radiation and Nuclear Safety Authority, Finland) who, with his knowledge of dosimetry, has enabled me to make accurate measurements even more accurate, and Docent Mika Kapanen, deputy chief physicist who, with his passionate attitude and expertise, has helped me in all aspects of research and clinical work. Also, I want to thank those colleagues and personnel who have inspired and encouraged me and created a positive working environment.

The financial support from the City of Tampere, the Elna Kaarina Savolainen Fund, the Seppo Nieminen Fund, the Nordic Association for Clinical Physics, the Finnish Association for Oncology, the International Doctoral Programme in Biomedical Engineering and Medical Physics (iBioMEP) and the former Department of Biomedical Engineering (TUT) is gratefully acknowledged.

It was an honour to have Professor Anders Ahnesjö, Department of Radiology, Oncology and Radiation Science at Uppsala University and Docent Mikko Tenhunen, chief physicist at the Department of Oncology, Helsinki University Central Hospital, as examiners of this thesis. I am also privileged to have Professor George X. Ding from the School of Medicine at Vanderbilt University as an opponent for this thesis.

To my parents, Seija and Yrjö, and sister Outi and family, without you I wouldn't be me and I wouldn't have done this – thank you. Finally, Riitta-Leena, my wife, and the wonderful Eemil, Sani and Silja – you are the light of my life and fuel for my soul.

Tampere, Finland, June 2014
Jarkko Ojala

TABLE OF CONTENTS

LIST OF ORIGINAL PUBLICATIONS

I **Ojala, J**., Hyödynmaa, S., Pitkänen, M. BEAMnrc Monte Carlo modelling of linear accelerator using parallel computing grid – validation of a common, fixed geometry model for photon and electron beams. Conference Proceedings for the XVIth International Conference on the Use of Computers in Radiation Therapy (ICCR). 2010. 4 p.

II **Ojala, J.**, Kapanen, M., Hyödynmaa, S., Wigren, T., Pitkänen, M. Performance of dose calculation algorithms from three generations in lung SBRT: comparison with full Monte Carlo-based dose distributions. J Appl Clin Med Phys, 15(2014)2, pp. 4-18.

III **Ojala, J.**, Kapanen, M., Sipilä, P., Hyödynmaa, S., Pitkänen, M. The accuracy of Acuros XB algorithm for radiation beams traversing a metallic hip implant – comparison with measurements and Monte Carlo calculations. **ACCEPTED FOR PUBLICATION to J Appl Clin Med Phys on 1 May 2014.**

IV **Ojala, J.**, Hyödynmaa, S., Barańczyk, R., Góra, E., Waligórski, M.P.R. Performance of two commercial electron beam algorithms over regions close to the lung-mediastinum interface, against Monte Carlo simulation and point dosimetry in virtual and anthropomorphic phantoms. Phys Med, 30(2014)2, pp. 147-54.

AUTHOR'S CONTRIBUTION

I The original idea for the work was the author's. The author designed and performed the experimental part and was solely responsible for the MC simulations. He analysed and visualised the results and wrote the paper as the corresponding author. All the co-authors commented on the results and the paper.

II The original idea for the work was M. Pitkänen's. The author was solely responsible for the MC simulations and part of the TPS calculations. The majority of the TPS calculations were performed by M. Pitkänen and M. Kapanen. The author analysed and visualised the results and wrote the paper in collaboration with M. Kapanen and M. Pitkänen. All the co-authors commented on the results and the paper at all stages of the process.

III The original idea for the work was the author's. The author was solely responsible for the MC simulations. The experimental work was done in collaboration with P. Sipilä. The author and M. Kapanen performed the TPS calculations. The author analysed the results in collaboration with M. Kapanen and was solely responsible for the visualisation of the results. The author wrote the paper as the corresponding author, with contribution from M. Kapanen. All the co-authors commented on the results and the paper at all stages of the process.

IV The original idea for the work was S. Hyödynmaa's. The author was solely responsible for the MC simulations and part of the experimental work. Part of the experimental work was adopted from the earlier work, as cited in the paper. M. Waligórski, R. Barańczyk and E. Góra were responsible for the TLD measurements and related discussion. S. Hyödynmaa performed the TPS calculations. The author analysed and visualised the results in collaboration with S. Hyödynmaa. The author wrote the paper as the corresponding author. All the co-authors commented on the results and the paper at all stages of the process.

LIST OF ABBREVIATIONS

1D	one-dimensional
2D	two-dimensional
3D	three-dimensional
3D-CRT	3D conformal radiotherapy
AAA	Anisotropic Analytical Algorithm
AAPM	American Association of Physicists in Medicine
AXB	Acuros XB
BCSE	bremsstrahlung cross-section enhancement
BEV	beam's eye view
CAX	central axis
CH	condensed history
CM	component module
CPU	central processing unit
CSDA	continuous slowing-down approximation
CT	computed tomography
d_{max}	depth of dose maximum
D_{max}	dose at d_{max}
$D_{m,m}$	dose-to-medium in medium
$D_{w,m}$	dose-to-water in medium
DBS	directional bremsstrahlung splitting
DTA	distance-to-agreement
DVH	dose volume histogram
EDW	enhanced dynamic wedge
EFD	electron field detector
EGS	electron gamma shower
eMC	electron Monte Carlo
EPOM	effective point of measurement
FWHM	full width at half maximum
GAI	gamma agreement index
GGPB	Generalized Gaussian Pencil Beam
GTV	gross tumour volume
GUI	graphical user interface
high-Z	high atomic number
HU	Hounsfield unit
IAEA	International Atomic Energy Agency
IC	ionisation chamber
IMRT	intensity-modulated radiotherapy
IPEM	Institute of Physics and Engineering in Medicine
LBTE	linear Boltzmann transport equation
LIC	liquid-filled ionisation chamber

linac	linear accelerator
MC	Monte Carlo
MLC	multileaf collimator
MMC	Macro Monte Carlo
MU	monitor unit
NIST	National Institute for Science and Technology
NRC	National Research Council
NTCP	normal tissue complication probability
OAR	organ-at-risk
PBC	Pencil Beam Convolution
PDD	percentage depth dose
PTV	planning target volume
QA	quality assurance
SBRT	stereotactic body radiotherapy
SBS	selective bremsstrahlung splitting
SFD	stereotactic field detector
SSD	source-to-surface/skin distance
Tays	Tampere University Hospital
TBI	total body irradiation
TCP	tumour control probability
TCSC	Tampere Center for Scientific Computing
TLD	thermoluminescence dosimetry
TPS	treatment planning system
TUT	Tampere University of Technology
UBS	uniform bremsstrahlung splitting
VMAT	volumetric modulated arc therapy
voxel	volume element

1. INTRODUCTION

Radiotherapy is one of the three most often used treatment modalities for patients diagnosed with cancer and it is usually combined with surgery and/or chemotherapy. [1] Chemotherapy acts systemically to treat the disease in all affected parts of the body, while surgery and radiotherapy aim for local control. The radiobiological effect of radiotherapy is based on the ability of the ionising radiation to harm the malignant cells so that their reproduction is inhibited and cell death follows during the course of treatment and thereafter. Ideally, only the malignant cells would be killed and healthy cells would be preserved, but unfortunately, due to the non-selective and stochastic nature of radiation energy absorption at the cellular level, normal tissue is also affected. This leads to the objective of radiotherapy that is to deliver the prescribed amount of radiation (absorbed dose) at the target volume to be treated and minimise the dose elsewhere in the body, especially in organs-at-risk (OARs). The therapeutic gain is optimised when the dose at the target volume is maximised for a given normal tissue dose ([2]).

External radiotherapy treatment can be divided into different phases, such as imaging for treatment planning, treatment planning and treatment, and each of them involves uncertainty that affects the treatment outcome. There are also various factors, not linked to the patient treatment workflow itself, but to inherent performance and calibration/configuration accuracy of treatment machines and computer software that have a direct impact on the accuracy of the treatment delivery. Most of these factors are related to dosimetric properties of the treatment machine output and to the performance of dose calculation algorithms of the treatment planning system (TPS). In the report by the American Association of Physicists in Medicine (AAPM) Task Group No. 105 (TG-105) ([2]) and in [3] it was summarised that, for example, dose differences in the order of 7% are shown to cause clinically detectable changes in treatment outcomes ([4]) and dose differences of 5% may result in substantial changes in tumour control probability (TCP) and normal tissue complication probability (NTCP) ([5-7]). The report by AAPM TG-65 ([8]) presented the effects of various sources of uncertainty in the treatment procedure on the total uncertainty involved in the treatment at present and the anticipated levels in the future. In Table 1 it can be seen that while the uncertainties related to the

absolute calibrated dose and dose calculation have had a major impact on the total uncertainty to date, correspondingly the improvements sought in the future are predicted to decrease the total uncertainty levels drastically. However, to benchmark and monitor the related accuracy levels, more advanced methods and tools for quality assurance (QA) are required.

Table 1. Estimates of uncertainty (in terms of one standard deviation) in absolute dose in the patient for the complete treatment procedure using megavoltage photons, today and in the future. ('Present' refers to the year 2004) [8]

Source of Uncertainties	Uncertainty at Present (%)	Uncertainty in Future (%)
Dose at the calibration point in water	2.5	1.0
Additional uncertainty for other points	0.6	0.3
Beam Monitor stability	1.0	0.5
Beam flatness	1.5	0.5
Patient data	1.5	1.0
Patient set up and organ motion	2.5	2.0
Overall (excluding dose calculation)	4.3	2.5
Dose calculation algorithm (multiple levels)	1.0 / 2.0 / 3.0 / 5.0	1.0 / 2.0 / 3.0
TOTAL	4.4 / 4.7 / 5.2 / 6.6	2.7 / 3.2 / 3.9

The majority of radiotherapy treatments are delivered with a linear accelerator (linac). In Figure 1 a typical medical linac is visualised and certain parts described below are numbered. Modern linacs are isocentric in construction, which means that all the parts of the linac rotate about a certain point in space, the isocentre. The gantry of the linac rotates ±180º from an upright position about a horizontal axis (dashed line in Figure 1) and the treatment couch and collimator rotation axes intersect on the horizontal axis at the isocentre. The electrons are produced by an electron gun (1) and they are accelerated in a linear standing or travelling wave accelerator guide (2). After a bending magnet system (3) the electrons enter a linac treatment head and impinge on a high-density X-ray target (4), in which a bremsstrahlung photon beam is generated. The beam is collimated to a desired size and shape with: 1) a primary collimator (5), which is located below the X-ray target and has a conical opening, 2) a secondary collimator (9), which consists of two pairs of high-density blocks ('jaws') that move in crossplane (X) and inplane (Y) directions, when viewing from a beam's eye view (BEV), and 3) a computer-controlled multileaf collimator (MLC) (10) below the jaws, which typically consists of 40 to 60 pairs of thin opposing individual leaves that move in a crossplane direction. In the beam path there is also a thin vacuum exit window, a beam flattening filter (6) to flatten the photon beam that is more intense around the beam central axis

(CAX), a dual transmission ionisation chamber (IC) (8) for beam monitoring, a field light mirror, a light field reticle and a plastic sheet. With the electron beam the X-ray target is retracted and the flattening filter is replaced by a scattering foil system (7). The jaws are in a preset static position, the MLC is retracted and the beam is directed towards the patient using an electron applicator attached to the bottom of the treatment head and shaped with an electron cutout positioned to the bottom of the applicator. [1]

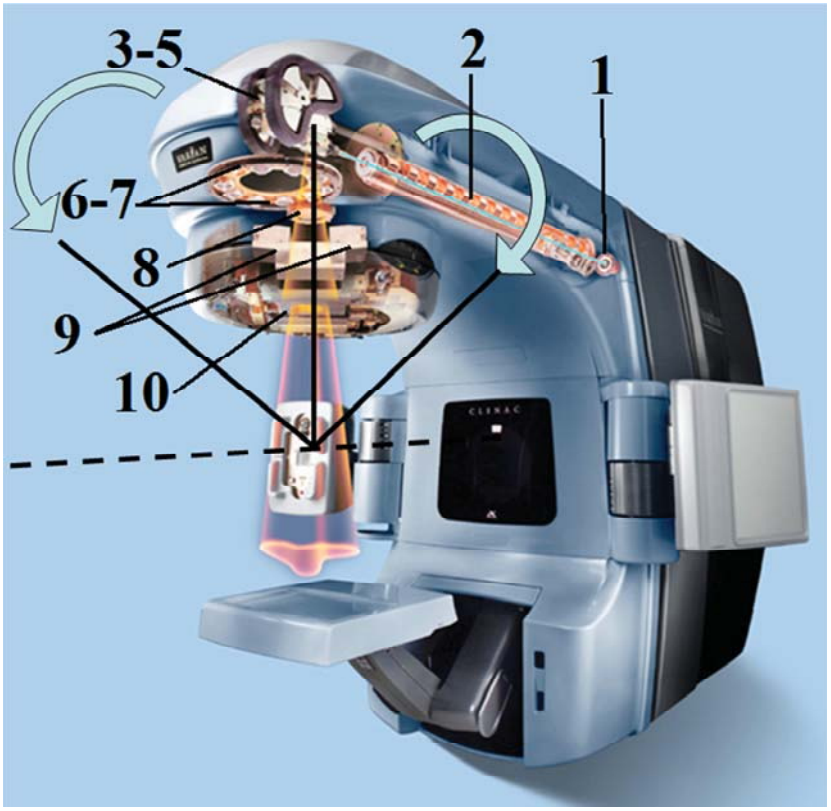

Figure 1. A visualisation of a clinical linac (Varian Clinac iX, Varian Medical Systems Inc., Palo Alto, CA, USA). The numbered items are described in the text. (Image courtesy of Varian Medical Systems)

Dosimetric measurements comprise a significant part of essential procedures in linac commissioning and during the operation. The linac has to be calibrated in terms of beam output and other beam properties prior to clinical use, and these parameters are to be monitored following a QA programme. The stability and accuracy of these basic parameters have a direct connection to the overall total uncertainty of the treatment process, as seen in Table 1. In addition to advancements in dosimetric methods, which have improved and are expected to improve the involved uncertainty levels affecting the treatment procedures, also modern treatment techniques have been developed, which introduce new

dosimetric challenges. While point and one-dimensional (1D) profile measurements have sufficed in the past, the demand for two-dimensional (2D) planar and three-dimensional (3D) volumetric measurements has increased along with intensity-modulated radiotherapy (IMRT) and volumetric modulated arc therapy (VMAT). These treatment techniques, in combination with sharp dose gradients and small field apertures, have added complexity to dosimetry. Apart from these issues, if more accurate patient treatment delivery is sought, QA procedures related to various treatment techniques and TPS dose calculation software benefit from dose measurements in heterogeneous phantoms that mimic patient anatomy and composition. However, the more realistic and complex phantom, e.g. anthropomorphic phantom, is desired, the more challenging it is to produce accurate, high-resolution, multidimensional measured dose distributions. The above-mentioned issues are discussed and further information on various tools and techniques for IMRT can be found in the report from the AAPM TG-120 ([9]).

In dose calculation, the absorbed dose in the calculation volume is determined by modelling the dose deposition by the transport of photons and electrons, with their interactions, in matter. In the past the dose calculations were based on various corrections to patient heterogeneity, distance variations and surface irregularities applied to measured dose distributions in water phantom. The introduction of computed tomography (CT) to radiotherapy enabled the contouring of treatment volumes and OARs and the dose calculation based on electron density calculation grid acquired from the patient CT dataset. In modern model-based dose calculation methods, the treatment beam is modelled as a multiple source model and the measurement data is used to fine-tune the model to represent the output of the linac. The dose deposition in the patient is calculated by applying superposition and convolution principles in combination with heterogeneity correction methods. [10] The most recent generation of commercial dose calculation algorithms is based on ‘fast’ implementations of statistical Monte Carlo (MC) methods or grid-based linear Boltzmann transport equation (LBTE) solver. [2,11] What is common for all the commercial dose calculation algorithms is that they need to be extensively benchmarked prior to clinical use and both phantom and patient verification against other independent dose determination methods, such as measurements, have to be performed following the QA programme. As the reported accuracy of the algorithms has improved, it has introduced challenges for dosimetric methods, as described above. The only means to compare the full dose distribution calculated by a commercial algorithm in a patient CT dataset is to compare it to the results of another dose calculation method.

The use of MC methods in radiotherapy originates from the 1970s. Their various applications have included the design of treatment head components, the determination of reference data for dosimetry, and the production of reference dose distributions for TPS QA. [12] Nowadays 'full' MC simulations are considered the gold standard for calculating dose distributions for radiotherapy purposes ([12]), especially in complex-shaped heterogeneous geometries ([2]). However, prior to utilising the full MC simulations for reference purposes, the MC models have to be commissioned and benchmarked with caution. Appropriately configured, they can be used for various purposes in radiotherapy QA, as long as sufficient computational resources are available, since it is an inherent characteristic of MC methods that statistical uncertainty of the resulting dose distributions decreases when the number of statistically sampled and simulated events is increased, which in turn increases the calculation time. [12] The MC methods have been extensively used in the literature and more information on their history, theory and applications can be found in extensive review articles, e.g. [12-16].

2. AIMS OF THE STUDY

The general objective of this work was to develop a full MC-based dose calculation tool, mainly to be used as a reference method for TPS dose calculation algorithm commissioning and QA procedures, but also to establish a reference for dosimetry purposes. The aim was to configure and benchmark the MC-based model for both photon and electron beams, calibrate it for absolute dose calculation, and implement the option to simulate dose distributions in CT-based phantoms. Finally, the value of the MC model was assessed by applying it to specific problems in radiotherapy dosimetry and dose calculations.

The specific aims of the study were as follows.

1. To construct MC models, which would represent the photon and electron beams of a selected treatment unit and show as small deviations from the well-defined measurements as possible;
2. To construct an MLC model within the photon beam MC models that would show as small deviations from the measurements as possible, which is essential for accurate IMRT and VMAT dose calculations;
3. To use the MC model for the accuracy assessment in the following areas of application:
   - a new TPS photon beam dose calculation algorithm in comparison to two other TPS algorithms in the stereotactic body radiotherapy (SBRT) of the lung, which uses small field apertures;
   - a new TPS photon beam dose calculation algorithm in the presence of high-density implanted material in comparison to measurements in a phantom and to other TPS algorithm in a patient case example, in which a hybrid VMAT technique is applied;
   - two TPS electron beam dose calculation algorithms in chest wall radio-therapy, with reference to the dose to lung and mediastinum;
4. To use the MC model to provide the first evaluation of the accuracy of a new TPS photon beam dose calculation algorithm in VMAT dose calculation in comparison with full MC simulations.

3. BACKGROUND

The MC methods, which are applied to numerical integrations by means of random sampling and statistics, are in general well-suited for modelling particle transport in physics. The transport of photons and electrons in a medium with their random trajectories is simulated using probability distributions representing the likelihood of individual interactions. Each particle induces a cascade of interactions, and the physical quantities of interest are recorded on the course. The track of one particle is called a particle history and the result is an average of a large number of particle histories. In other words, since these methods are of a stochastic nature, it can be summarised that when using the MC techniques, random numbers are sampled from a user-defined input domain and they are used to perform a large number of separate output simulations. The results are combined and analysed and a simplified result is to fall within evaluated statistical uncertainty limits. In radiation transport calculations, the accuracy of cross-section data for individual interactions, which represents the likelihood of the interactions, has a fundamental relevance in the overall accuracy of the MC simulation results. [2,13,17]

3.1. BEAMnrc Monte Carlo simulation system

The MC simulations in this study are performed with a BEAMnrc code system ([18]). The history of the system and underlying codes dates back to the 1970s, but the versions from 2007, 2009, 2010 and most recently, from 2013 were applied. The system is owned and maintained by the National Research Council (NRC) of Canada. The BEAMnrc system is built around EGSnrc (electron gamma shower) general purpose code, simulating the photon and electron interactions and transport in medium ([19]). BEAMnrc is a general purpose EGSnrc user code for simulating radiation sources and the option to model radiation transport through a linear accelerator treatment head was applied in this study ([20]). DOSXYZnrc is a general purpose EGSnrc user code to score an absorbed dose in a rectilinear voxelised phantom geometry ([21]). Another user code, *ctcreate*, allows the user to build a DOSXYZnrc phantom from a CT dataset, in which the dose is then calculated ([21]). PEGS4 is a data preparation code part of the EGSnrc that can be utilised to determine cross-section data for user-defined materials ([19]).

3.1.1. Radiation transport physics modelling (EGSnrc)

3.1.1.1 Photon interactions

Photon transport in a BEAMnrc system is governed by modelling four different types of interactions: 1) coherent (Rayleigh) scattering, 2) photoelectric absorption, 3) incoherent (Compton) scattering, and 4) pair production. A photon interaction process, where photons are scattered by bound atomic electrons, without exciting or ionising the atom, is called coherent scattering. In this process, no energy is transferred to charged particles – the incident photon is scattered to account for the small recoil energy. Coherent scattering is characteristic of low energy photons traversing in high atomic number (high-Z) material (in this study, 'high-Z' refers to materials of higher (effective) atomic number and density than that found in human tissues). [17] In EGSnrc, the default total coherent scattering cross-sections are based on the work by Storm and Israel ([19,22]) and atomic form factors on the work by Hubbel and Øverbø ([19,23]), but other options for cross-section data are also available. It is recommended that the Rayleigh scattering option is turned on for calculations, in which particle energies are of the order 1 MeV and less. [19]

In photoelectric absorption the whole energy of the incident photon is absorbed by a tightly-bound orbital electron of the atom. This electron, a photoelectron, is ejected with a kinetic energy equal to the energy of the original photon, from which the binding energy of the electron is subtracted. If the resulting energy is large enough, the photoelectron is emitted from the atom and the atom is ionised, but when the energy is below this level, the photoelectron rises to a higher orbit and the atom is excited. If the photoelectron is emitted, the vacancy is filled by an electron from a higher shell and the energy difference between the orbital energy levels is emitted as a fluorescent (characteristic) X-ray photon or as an Auger or Coster-Kronig electron. [17] In EGSnrc, the default total photo-absorption cross-sections are based on the work by Storm and Israel ([19,22]) and the direction sampling on the Sauter distribution ([19,24]), but other options for cross-section data are also available. The cross-section for the photoelectric effect is considerably larger than for the coherent scattering in the low energy range (~1 MeV) ([17]).

In the case of incoherent (Compton) scattering, the incident photon interacts with a loosely bound orbital electron. As a result, the photon is scattered and its energy is smaller than the energy of the incident photon. The energy difference is transferred as kinetic energy to the orbital electron, which is ejected from the atom. The formalism to determine the cross-section for the interaction is based on the work by Klein and Nishina, and the work by Hubbell at the National Institute for Science and Technology (NIST) in the United States

complemented the theory to account for the electron binding energy effects that are especially noticeable at low photon energies in high-Z materials. [17] In EGSnrc, the incoherent scattering calculations were originally based on Klein-Nishina theory, but in most recent versions of the code system, the option to utilise the binding effects and Doppler broadening following the impulse approximation principle has also been included. [19] Incoherent scattering is the predominant photon interaction type at photon beam energies typically used in radiotherapy.

At photon energies greater than 1.022 MeV, pair production is possible. In this interaction type, the photon is absorbed with all its energy in the atom nuclear field and an electron-positron pair is formed. When the photon interacts with an orbital electron with energies exceeding 2.044 MeV, a triplet production may occur, when in addition to electron-positron pair production, an electron is also ejected. [17] In EGSnrc, the pair production cross-section data is based on extreme relativistic first Born approximation, described in work by Motz, Olsen and Koch ([19,25]). This cross-section data is improved by introducing an empirical correction factor based on the work by Storm and Israel ([19,22]). In the most recent version of the code system, the cross-section data is further enhanced to account for corrections based on the partial-wave analysis calculations by Øverbø, Mork and Olsen ([19,26]). The triplet production in EGSnrc is explicitly simulated following the first Born approximation theory reported by Votruba ([19,27]) and Mork ([19,28]).

3.1.1.2 Electron interactions

The number of electron interactions along a certain traversed path length in medium is much greater than for the same path length with photons, because the electrons have electric charge and non-zero rest mass. There are two types of basic interactions through which the electrons lose energy, namely radiative energy losses and inelastic collisions with atomic electrons. Radiative energy losses occur via bremsstrahlung formation, which is a result of electrons and positrons undergoing a Coulomb interaction with an atomic nucleus, and positron annihilation, which is a result of positrons annihilating with orbital electrons. As a result of positron annihilation, most commonly two annihilation photons with energy of 0.511 MeV are created, moving in opposing directions. When electrons undergo inelastic collision with orbital electrons, the energy transfer may result in atomic ionisation or excitation. In addition to the above-mentioned interaction types, the elastic collision of an electron, which occurs with an atomic nucleus, is an interaction process that contributes to the angular deflections of electrons, but not to energy transfer.

Since the simulation of every individual electron interaction is impractical and changes in the electron state due to single interaction are usually small, Berger introduced a condensed history (CH) technique. It models a number of electron interactions, leading to both energy and directional changes, in a single 'step' ([19,29]). The choice of step-size is bipolar: 1) the step-size has to be so large that sufficiently large number of interactions occur in order that the multiple scattering theories are applicable, but 2) the step-size has to be small enough so that the cumulative contributions to deflections in electron tracks and energy losses are such that the simulation provides accurate results in terms of voxel-based energy deposition, boundary crossings and electron-track generation. In EGSnrc, the CH technique belongs to Class II scheme, which means that as a result of 'catastrophic' collisions, where bremsstrahlung photons and atomic electrons set in motion possess energies greater than set energy thresholds, the resulting photons and electrons are simulated as individual particle tracks. The particles with energies less than threshold levels are simulated by applying continuous slowing-down approximation (CSDA). [19]

The EGSnrc bremsstrahlung production cross-section data for energy levels applied in radiotherapy are based on first Born approximation Bethe-Heitler data with an empirical correction factor. Other options are to use the NIST bremsstrahlung cross-section data or further enhanced NIST data from the NRC. [19] With electron-electron and positron-electron inelastic collisions, the Moller ([19,30]) and the Bhabha ([19,31]) cross-section data is used, respectively. When including the atomic electron binding, these interactions may produce inner shell vacancy, which in EGSnrc is called electron impact ionisation and when included in simulations, one of the empirically obtained cross-section data can be selected. Two-photon positron-electron annihilation processes are also simulated in EGSnrc. The cross-section data for elastic collision of an electron that occurs with an atomic nucleus, which also takes into account spin effects, is based on the partial-wave analysis solution of the Dirac equation following the work by Mott ([19,32]). Finally, if the atom is in an excited state after Compton and photoelectric processes, the atomic relaxation to the ground state results in the emission of characteristic X-rays and/or Auger or Coster-Kronig electrons. In EGSnrc, this is explicitly modelled for shell vacancies with binding energies greater than 1 keV. [19]

With the EGSnrc CH technique, the path length, energy loss, change in direction and spatial displacement for each step in the random walk are determined using various approximate methods, since the exact solutions for the equations including the parameters are not known. The implemented electron-step algorithm produces accurate transport in an infinite, homogeneous medium for varying step sizes. For electron transport in heterogeneous medium,

a boundary crossing algorithm is also needed, since near a material interface the curved path of an electron may cross a material boundary and then cross back to the original material. Thus, the transport steps on the other side in different material would be different from the ones in the original medium. In EGSnrc this is overcome by changing the elastic scattering from multiple to single mode, when the distance to the boundary is smaller than the set limit.

3.1.2. Source and geometry modelling (BEAMnrc)

BEAMnrc is a general purpose EGSnrc user code for simulating radiation sources and modelling radiation transport through various structures, such as a linac treatment head. In Figure 2 the simulation process is presented as a flow chart. The simulation is based on the geometry model of the treatment head, which has a modular layered structure. First, the user must specify which separate parts are to be included and this is done with component modules (CMs). There are a number of CMs for various structures and they are completely independent, non-overlapping blocks in the geometry model. Then the accelerator model is built and compiled, for which various input parameters and cross-section data must be specified prior to simulation. In the input file the user provides detailed information on the geometry and material specification for each CM, specifies the desired output data form, defines parameters that specify the transport physics modelling and cross-section data and lastly, defines the radiation source. The source is located at the entry surface of the first CM or certain types of sources may be located between CMs. [20]

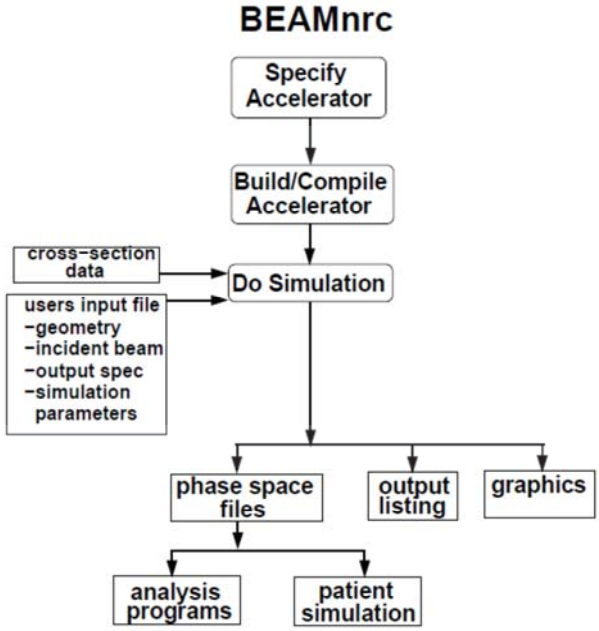

Figure 2. A flow chart of the simulation using the BEAMnrc code system. [18]

In a radiotherapy treatment simulation, the output data is usually collected on a user-specified plane, to a phase space file, in which the energy, position, direction, weight and charge of each particle is recorded. Options for various output listings and output graphics files for treatment visualisation are also available. The phase space file data can be used as input for BEAM Data Processor (BEAMDP) utility for deriving particle energy spectral, mean energy, planar fluence and angular distributions. The most general use for the phase space file is to employ it as a plane source for the phantom simulation. [20]

3.1.2.1 Radiation sources in BEAMnrc code system

In addition to the option to use a phase space file as a source in the BEAMnrc accelerator simulation (ISOURC = 21), there are 15 other source options in the BEAMnrc code system version 2013. Most commonly, in the case of treatment head simulation, the radiation source is the electron beam that is directed downwards from the bending magnet system, right above the horizontal level of the X-ray target. For this purpose there are two sources in the BEAMnrc code system version 2013: ISOURC = 0, which is a parallel circular beam, and ISOURC = 19, which an elliptical beam with Gaussian distribution profile in an X and Y direction. In this study, ISOURC = 19 was applied to characterise the initial electron beam in the simulations. The beam profile is defined either by standard deviation or full width at half maximum (FWHM) in cm in both the X and Y direction. The incident beam energy may be monoenergetic or the user may define an energy spectrum. The user can select whether the beam is set parallel to the incident beam axis or they can choose to apply a mean angular spread about the beam CAX. [20] One of the subjects of most intense research in linac beam modelling has been the selection of initial electron beam parameters that produce the best congruence between the simulation results and the measured reference dose distributions. The reason for this is that the linac manufacturers have not provided detailed information on the initial electron beam characteristics and the parameters are extremely difficult to determine through measurements. Therefore, the most general option is to build a detailed geometry model of the treatment head, select appropriate physics simulation parameters, and perform an elaborate and laborious iterative tuning process for each initial electron beam parameter.

3.1.2.2 Geometry modelling in BEAMnrc code system

The geometry model consists of CMs that are independent blocks that take up a horizontal slab portion of the model, such as in the linac treatment head. In the BEAMnrc code system version 2013 there are 25 different CMs, which are designed to cover various purposes in the modelling of other types of radio-therapy treatment machines, such as tomotherapy units. In this section only

those CMs that are used in this study are described and their schematics are shown in Figure 3 (a)-(b). [20]

SLABS is the most simplistic CM, which is used to model one or more slabs of material. The materials and thicknesses of slabs in square outer boundaries may vary and the structures are perpendicular to the axis that represents beam CAX. CONS3R is a CM with a cylindrical structure that has an interior and outer region, which can be different media. CONS3R is ideal for modelling conical structures. The region boundary is defined as a series of successive points, as seen in Figure 3 (a). FLATFILT is the most general purpose of the CMs that are rotationally symmetric about the beam CAX. It can be used to simulate multiple stacked cones. The number of cones on each level is arbitrary and the material for each cone in each layer can be different. The most common use for FLATFILT is the photon beam flattening filter modelling. CHAMBER is a cylindrical CM specialised in parallel plate monitor IC modelling. [20]

For beam collimation there are several specific CMs. SYNCJAWS, which is used in this study, is an improved version of DYNJAWS (which in turn is a version of JAWS shown in Figure 3 (b)), which allows the dynamic motion of structures either in 'step-and-shoot' or 'dynamic' mode. What is common to all three CMs is that they can be used to model an arbitrary number of paired blocks in two perpendicular horizontal orientations. Most commonly these CMs are used to model two pairs of secondary collimators in a linac treatment head in an X and Y direction. The option for 'dynamic' motion allows the simulation of enhanced dynamic wedge (EDW) fields and the improvement in SYNCJAWS is to enable the synchronised movement with several other CMs, beam simulation and dose calculation with DOSXYZnrc. This is analogous to DYNVMLC and SYNCVMLC, which can be used to model the Varian Millennium (Varian Medical Systems Inc., Palo Alto, CA, USA) MLC. The complex structure consists of three different types of leaves and their cross-sections. The leave ends can be straight or round and the leave side surfaces can be focused to a point above, in the treatment head. As with CMs modelling the jaws, the leaves may either define a static field or the simulation may be in 'step-and-shoot' or in 'dynamic' mode. SYNCVMLC allows a synchronised simulation similar to SYNCJAWS. [20,33] PYRAMIDS is a CM for modelling rectangular collimators or blocks, which is implemented with pyramid-shaped structures with an arbitrary number of layers. Each layer has three regions, all of which may be assigned a different medium. In addition, there are certain CMs, such as MIRROR and APPLICAT, which are designed for modelling certain specific structures, but in this study these structures are modelled with the more general purpose CMs mentioned above. [20]

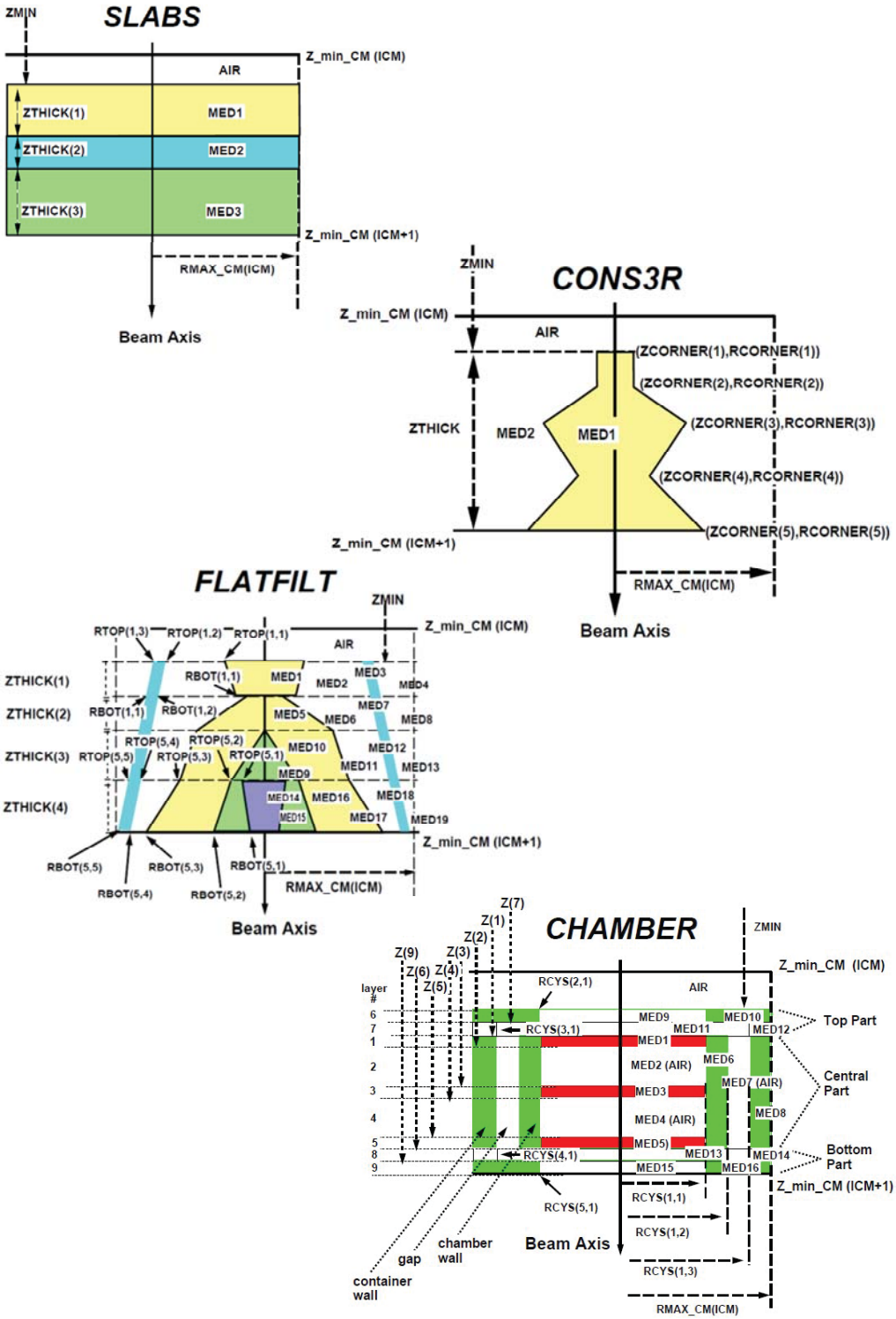

Figure 3. (a) Schematics of the CMs used in this study. [20]

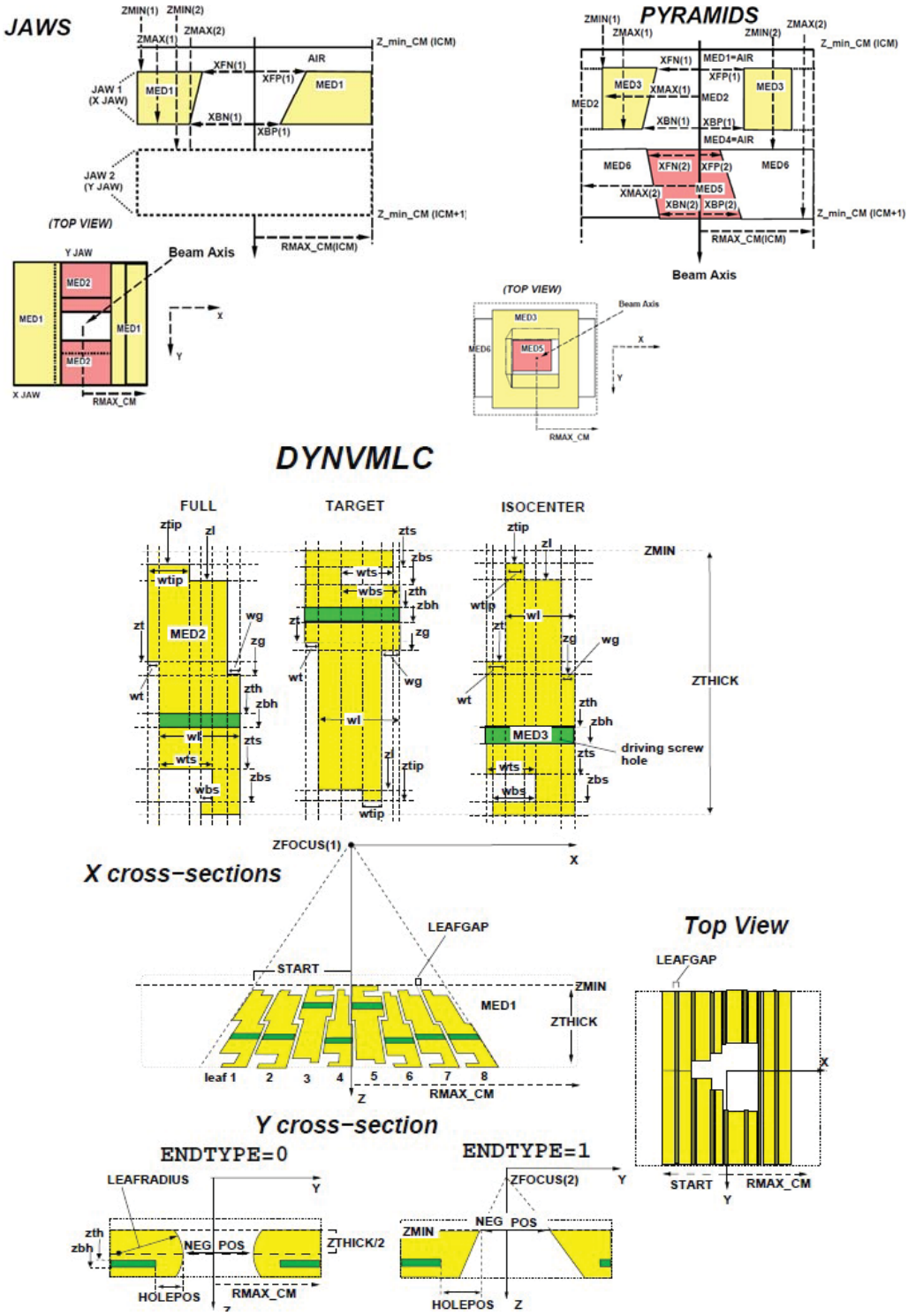

Figure 3. (b) Schematics of the CMs used in this study. [20]

3.1.3. Dose calculation (DOSXYZnrc)

The actual dose calculation in the BEAMnrc code system is performed with DOSXYZnrc, which is a general purpose EGSnrc user code. It is used to simulate the electron and photon transport and score an absorbed dose in a rectilinear voxelised phantom geometry. DOSXYZnrc is accompanied with *ctcreate*, which is a user code that can be used to build a DOSXYZnrc phantom from a CT dataset, in which the dose is then calculated. The user may also define a virtual phantom of arbitrary size and the sizes of volume elements (voxels) in the phantom may vary in all three dimensions. The voxels can be of any density and/or material. The materials for the phantoms are defined in the PEGS4 material library, which is a file that contains the cross-section data for each material. *ctcreate* reads slices in the CT dataset and converts the Hounsfield Unit (HU) values to material densities and assigns a material for each voxel, according to a user-defined conversion curve. [21]

In DOSXYZnrc there are 12 different sources to be used in simulations. Many of them are similar to radiation sources included in the BEAMnrc code system, but most often the option to utilise a phase space file from a BEAMnrc simulation or a full BEAMnrc treatment head simulation is used, as is this case in this study. For these purposes there is isource = 2, which is the phase space source with which the user may arbitrarily choose the direction of the source plane and distance with regard to the phantom. This is visualised in Figure 4. [21]

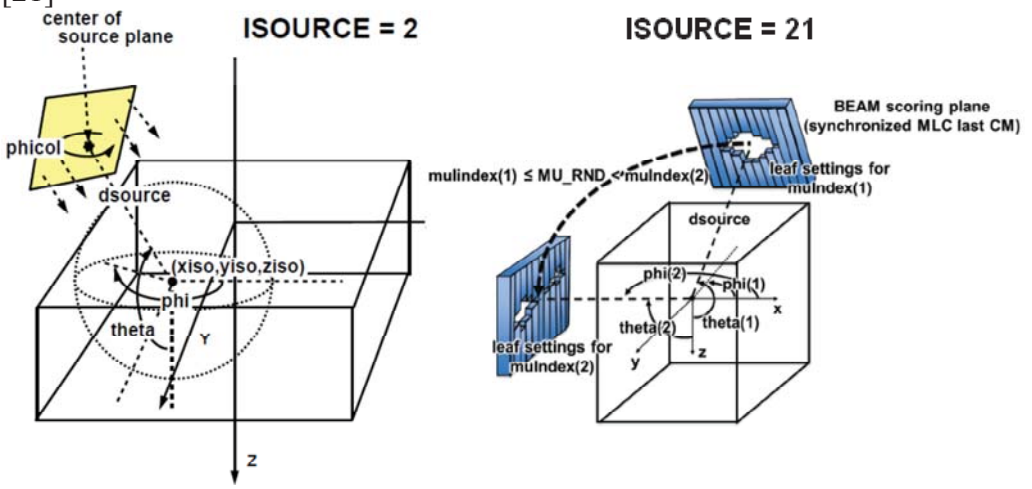

Figure 4. Visualisations of the DOSXYZnrc sources used in this study. [21]

isource = 20 is a source, where the same phase source is used from multiple directions and between the phase space source plane and the phantom there is an option to insert a part of treatment head components which may have

different settings depending, on the position of the source plane in regard to the phantom, for example. This allows the simulation of continuous motion of the source, to which the synchronised movement of beam-modifying components, such as jaws and MLC, simulated with SYNCJAWS and SYNVMLC CMs, is linked. The simulation of these components is performed as a shared library, which is dynamically loaded by DOSXYZnrc at run time. isource = 21 is otherwise similar to isource = 20, but the phase space source is replaced with a full BEAMnrc treatment head simulation (Figure 4). [21,33]

3.1.4. Variance reduction techniques in BEAMnrc system

The MC calculation efficiency, epsilon (ε), is defined as:

$$\varepsilon = \frac{N}{Ns^2T} = \frac{1}{s^2T} ,$$

where N represents the number of simulated particle histories, s^2 represents an estimate of the true variance (σ^2) of the quantity of interest, such as absolute dose, and T represents the total central processing unit (CPU) calculation time needed to reach the variance. It can be shown that the efficiency is more or less independent of N. If one aims to enhance the efficiency, either 1) T needs to be decreased for a given N, keeping the s^2 unchanged, or 2) s^2 needs to be decreased for a given T. A technique that improves the efficiency without introducing significant bias to the result, by changing the s^2 for given N, is called a variance reduction technique. This is not to be confused with such efficiency enhancement methods where improved efficiency is achieved by making deliberate approximations into radiation transport calculations. [2,34]

There are several variance reduction techniques implemented in the BEAMnrc system. The most straightforward, which is rarely even considered as a variance reduction technique, is to increase the electron energy cutoff values that define the energies at which the electron particle history is terminated and the energy is locally absorbed. A similar but more sophisticated method is the range rejection technique. There are several options for performing the range rejection, but the basic idea is to terminate the charged particle history and deposit all the energy locally, if the energy of the particle is too small and thus the range is too short to cross the region boundary or to reach the region of interest. This introduces an approximation to the simulation, since by depositing the charged particle energy via range rejection, the contribution to elsewhere than current region by bremsstrahlung photons that would have been created without range rejection is neglected. One aim in the design of the variance reduction technique called photon forcing was to improve the production of contaminant electrons in air in photon beam simulations. The parent photons are forced to interact in user-specified CMs and in order to sustain an unbiased

result, the weights of the unscattered and scattered photons were distributed accordingly. [2,18,20]

Bremsstrahlung photon splitting techniques are often used in treatment head simulations to enhance the simulation statistics of photons generated in electron interactions. Instead of generating only one bremsstrahlung secondary photon in such interaction, the photon is split into a large number of secondary photons, adjusting the weights and survival of the photons accordingly to maintain unbiased simulation results. In a BEAMnrc system there are three options for bremsstrahlung splitting: uniform bremsstrahlung splitting (UBS), selective bremsstrahlung splitting (SBS) and directional bremsstrahlung splitting (DBS). The largest efficiency improvement has been shown by DBS, which has similarities with SBS in applying the technique only to the photons that are directed towards the field of interest downstream in the treatment head, in companion with the Russian Roulette feature. [2,18,20,35]

The most recent addition to variance reduction techniques in the BEAMnrc system is the bremsstrahlung cross-section enhancement (BCSE). BCSE is designed to improve efficiency in simulations where bremsstrahlung targets are utilised for X-ray beam production. This is done by artificially increasing the number of statistically-independent photons generated in interactions resulting in bremsstrahlung emission. The merit of BCSE is best seen in low energy applications and the largest efficiency gain is achieved when it is used with UBS or DBS. [20,36]

3.2. Reference measurement data acquisition for MC model commissioning

The commissioning of a linac MC model intended for various TPS benchmarking and QA purposes is an iterative multiphase process. As described in Section 3.1.2., prior to simulation the geometry model and initial electron beam parameters, among other input data, have to be determined. The detailed geometric and material information on each component of the linac treatment head usually needs to be requested from the linac manufacturer or determined via mechanical or attenuation measurements. Another option is to use phase space files available from public databases or the manufacturer. However, depending on what part of the treatment head is modelled in these ready-to-use files, using them is always a more limited option in terms of matching and tuning the MC model to a certain linac, in comparison to modelling the whole treatment head, including the initial electron beam.

The first parameter set for the initial electron beam should follow the estimated values from the manufacturer and/or the values used in other studies. To find the optimal initial electron beam energy spectrum, an acceptable congruence, 'a match', between the calculated and measured depth dose distribution should be found. The criterion for a match is up to the user – e.g. according to [12] an agreement is found if the local differences at depths greater than the depth of dose maximum (d_{max}) are smaller than 2%. The depth dose measurements should follow well-known protocols, such as the International Atomic Energy Agency (IAEA) TRS-398 ([37]) or the report from the AAPM TG-51 ([38]), in order to obtain reference level comparison data. For photon beams a medium-sized field, e.g. 10 x 10 cm^2, with a source-to-surface/skin distance (SSD) of 100 cm and a cylindrical, thimble IC with active volumes of order 0.1 cm^3, with effective point of measurement (EPOM) correction applied, represents a typical measurement set-up.

After tuning the initial electron beam energy spectrum, the next step in the iterative MC model tuning process is to choose whether the initial electron beam is a pencil beam of a certain width (usually between 0-2 mm) or a beam with Gaussian intensity distribution (usually 1-2 mm FWHM). By varying the width of the beam, the calculated dose distributions are to be compared to measured relative dose profiles of a large field size beam at slightly greater depths than d_{max}. [12,39] The measurements should follow the above-mentioned protocols and a good choice for the detector is a medium or small volume cylindrical IC, with minimal directional dependence. In addition, if dose distributions outside the field, e.g. in the shadow of collimators, are of interest, the detector should not be oversensitive to scattered radiation. In the tuning process, a match is found when the local differences in flat, high dose regions of the dose profile are below the set criterion, e.g. 1-2%, and the distance-to-agreement (DTA) at a 50% dose level (when the dose profile is normalised to 100% at beam CAX) would be as small as possible. When the latter criterion is fulfilled, it suggests that the field size defined by the jaws with the MC model is in agreement with the actual field defined by the jaws with the linac. To fine-tune the MC model, a divergence of 0-1° to the initial electron beam could also be applied. Since the parameters defining the initial electron beam, its width and divergence have small combined influence on the depth dose distribution, the original match with the measured depth dose has to be verified ([40]). In case of worse agreement, all the steps need to be repeated until both depth dose distributions and dose profiles agree with the measured dose distributions at the desired agreement level. [12]

An agreement for one field size in depth dose distributions and for another field size in dose profiles at one depth does not ascertain that the MC model would

produce congruent dose distributions for the whole field size range at all depths. [39,41] Regardless of the field size, for the dose in the dose build-up region it is difficult to produce reference measurement data, due to large dose gradients and charged particle disequilibrium, and thus special attention has to be paid to the measurement equipment selection. The most common detectors for measurements on the surface and build-up dose region include semiconductor detectors, radiochromic films and parallel plate ICs with empirical correction methods, for which the small dimension of the active volume in the direction of the beam is common. [42-44] The challenges in the modelling of the dose build-up region are pronounced, especially with the largest field sizes. The issues are related to the performance of the MC model in simulating the extra-focal radiation, i.e. the scattered photons and contamination electrons from the treatment head components and air, when the collimators are wide open ([45-46]). On the other hand, according to some studies, the small field sizes are recommended for tuning the initial electron beam energy spectrum, since the effect of the extra-focal component of the beam is less pronounced, and thus the primary electron energy spectrum affects the depth dose distributions the most ([12,47-48]).

Small field dosimetry has become an area of intense research during the past decade, since the advances in radiotherapy treatment techniques have favoured the utilisation of small fields and field apertures. There are a number of related theoretical and technical issues that pose serious challenges, if reference-level measurement data for small field dose distributions is desired. [49-50] The detector selection for the measurements should be performed with great care. For the performance, high spatial resolution and water equivalence are primary attributes ([51-53]). The former is also important if one wants to minimise the averaging effect, which is related to the size of the detector active volume, in field penumbrae (in the region of 80%-20% relative dose) in dose profiles for all field sizes ([54]). No ideal detector has yet been found especially for small field dosimetry, but, e.g. semiconductor and diamond detectors, radiochromic films and liquid-filled ICs, among others have shown good characteristics, but all of them have suffered from some drawbacks [55-56]. It has even been hypothesised that instead of attempting to design an ideal detector or determining correction factors ([57]) via, MC calculations ([58-59]), for example, the dosimetric quantities could be directly calculated, which would be equivalent to performing measurements in ideal conditions ([50]). Many aspects of and challenges related to small field dosimetry have been comprehensively discussed in the Institute of Physics and Engineering in Medicine's (IPEM) Report Number 103 ([60]).

For electron beams the initial electron beam tuning process is similar to photon beams. For reference depth dose measurements with electron beams Roos or NACP-type well-guarded parallel plate ICs are recommended detector choices with an SSD of 100 cm and a 20 x 20 cm^2 field defined by the electron applicator, according to well-known dosimetry protocols, such as IAEA TRS-398 ([37]) and AAPM TG-51 ([38]). With dose profile measurements, medium or small volume cylindrical ICs are recommended. If a high resolution is desired, for example in dose profile penumbrae or in depth dose distributions at depths smaller than d_{max}, unshielded semiconductor and diamond detectors and radiochromic films are preferable choices ([61-63]). In output factor measurements it is similar for both photon and electron beam dosimetry that the detector sensitivity should be large enough for stable readings and the radiation fluence across the detector active volume should be uniform. Both issues bring about challenges, especially with small fields, where output factors are usually measured with semiconductor or diamond detectors. [37,60] If multiple detectors are utilised in output factor measurements, it is recommended to perform measurements with overlapping field sizes and apply the 'daisy-chaining' technique to combine the results ([64]). In this work, the measurement depths for output factors were 5 and 10 cm for 6 MV and 18 MV photon beams, respectively, and d_{max} for electron beams.

What is common for both photon and electron beam dosimetry when acquiring reference dose distributions for the commissioning of an MC model is that the assets of each dosimetry technique and device should always be taken into account. There is no ideal detector for the whole field size range and for all purposes. Therefore, in an ideal case, the reference dose distributions should be combined results from measurements with multiple detectors and measurement techniques.

3.3. Treatment beam simulations and dose distribution calculations applying MC methods

3.3.1. Photon beams

With time, the MC models have begun to produce dose distributions with comparable accuracy to measurements in square fields and they have been introduced as alternative reference methods to various applications in dose calculations and dosimetry. As the MC codes and computing resources have evolved, the MC codes have become the gold standard method for simulating dose distributions in heterogeneous phantom and patient geometries ([2,12]). However, all the studies applying MC methods agreed that the MC model

requires rigorous and comprehensive commissioning, including benchmarking in well-known conditions, before it can be utilised as a reference for other purposes.

Studies which describe the MC model commissioning and tuning process and the resulting performance in water phantom compared to measurements are numerous. The early works focused on the quantification of various beam properties, such as scatter components ([65-66]), energy and angular distributions ([67-68]), dosimetric quantities ([69]), and the contribution from different treatment head components ([70]). Many groups studied the effect of different simulation parameters to calculated dose distributions and attempted to achieve as good congruence with the reference percentage depth dose (PDD) curve, dose profile and output factor measurements as possible. They also discussed the possible reasons for deviations. It was common that with field sizes from 2 x 2 cm^2 to 40 x 40 cm^2 in PDDs at depths beyond d_{max}, dose profiles in high dose regions and output factors agreements better than ±1-2% of dose at d_{max} (D_{max}), ±2-3% of D_{max} and ±1-2%, respectively, were attained. [40-41,46,71-79] However, in the build-up region in PDDs, especially with large fields and high nominal beam energies, large discrepancies were reported with linacs in clinical use. To explain the discrepancies, potential sources and solutions, such as: 1) lack of neutron simulation ([80]), 2) insufficient electron contamination modelling ([45,48]), 3) utilisation of improved dosimetry techniques for collecting comparison data ([81-82]), 4) improved transport physics modelling ([81,83]), and 5) more detailed knowledge on treatment head geometry ([41,84]) were investigated. This was different from research linacs, with which the details needed in simulations are well known and thus the differences from empirically corrected measurements were less than ±1% ([85]).

The MLC is one of the most complex structures of the treatment head in regard to geometry modelling and commissioning benchmarking, due to small, complex details in the geometry and consequent challenges in the acquisition of reference measurement data for comparison. There are reports on the modelling and benchmarking of Elekta MLC (Elekta Oncology Systems, Crawley, UK) ([86-87]), BrainLAB m3 microMLC (BrainLAB, Feldkirchen, Germany) ([88-90]), Varian MarkII, Millennium ([91-97]) and HD120 ([98-99]) MLC (Varian Medical Systems Inc., Palo Alto, CA, USA). Benchmarking has included MLC-shaped static and dynamic MLC fields in both ‘step-and-shoot’ and ‘dynamic’, ‘sliding window’ mode. The most detailed MC MLC models have resulted in good agreement with static and dynamic field profile, transmission and 2D dose distribution measurements, which in turn have resulted in the conclusion that MC models are applicable to IMRT and VMAT dose calculation.

3.3.2. Electron beams

The earliest studies using the first version of the BEAM code system mostly concentrated on modelling the clinical electron beams. As with photon beams, many investigations focused on the quantification of various dosimetric beam properties, such as stopping-power ratios ([100-101]) and energy-related parameters ([102]). In studies where the MC model simulation parameters were tuned to obtain the best agreement with PDD, dose profile and output factor measurements, it was not uncommon that the local differences of smaller than ±1-3% of D_{max} in PDDs, ±1-2% of D_{max} in dose profiles in high dose regions, 1-2 mm in DTA in profile penumbrae and ±1-2% in output factors were obtained for beams with nominal energies of between 4 MeV and 50 MeV ([18,103-109]).

3.3.3. Heterogeneous phantoms and patient plan calculation

Once the accuracy of the simulated radiotherapy beam coming out of the treatment head is satisfactory when compared to measurements, there are several issues that have to be taken into account prior to heterogeneous phantom or patient plan simulations. If the simulations are to be performed in virtual phantoms, the construction of the rectilinear phantom geometry is straightforward. In order to compare the simulations to measurements, the user may for example define a whole or half slab or other arbitrary shape of non-water-equivalent material and otherwise assign the phantom as water or water-equivalent plastic phantom material. As an example, films between the slabs in the phantom or other detectors in water can be used to collect the reference measurement data for comparison. [2]

Whether the phantom is virtual or CT-based, has the correct material assignment and in addition with CT-based phantoms, has a verified HU value to material density conversion curve, are crucial elements for the achievement of accurate MC-calculated dose distributions. [110-113] The conversion must be extended to high HU values if the calculation phantoms include high-Z materials. [114] If the MC model is intended for TPS dose calculation benchmarking, the curve for MC simulations should be identical to that used in the TPS. Prior to utilising the MC model for further purposes, the commissioning should include tests with heterogeneous phantoms, for which reference measurements are available. The heterogeneities should include low and high-density tissue-equivalent and high-Z material inserts of varying sizes. The materials should represent lung ([115-118]) and bone tissues ([119]), also applicable for electron beam treatments ([120-121]), and high-Z metals or metal alloys ([122]), so that the accuracy of the MC model would be tested under

conditions of charged particle disequilibrium and at various material interfaces. The benchmarking should also contain clinically more relevant anthropometric phantoms, which geometrically represent anatomical regions, such as thorax or pelvic phantoms, and anthropomorphic phantoms ([123-125]) which, in addition to geometrical dimensions, are also made of tissue-equivalent materials. [2]

An MC model that is appropriately commissioned can be used in TPS dose calculation algorithm benchmarking with virtual phantoms or patient CT datasets. The model can be applied to cases where commercial dose calculation algorithms are known to produce inaccurate dose distributions or to cases where no experience on the performance of the commercial algorithms is available. In general, materials with densities and atomic compositions significantly differing from water have been reported to cause large uncertainties in dose calculation. The effects are especially pronounced in anatomical sites where there are tissues with widely varying densities in complex 3D shapes. At the other extreme end of the density range are airways, especially of interest in head and neck radiotherapy, where large photon/electron energy fluence perturbations are introduced into the air and in the vicinity of air/tissue interfaces. Low-density materials, such as lung tissue, have probably elicited the greatest level of interest among the radiotherapy community, since the insufficient and/or imperfect inclusion of electron transport modelling has caused substantial uncertainties – as large as around 10% to 20% ([2-3]) – in clinical dose calculations, the greatest being with high energy photon beams and with small fields, especially applied in the SBRT of the lung ([126]). At the other end of the density range there are bone and high-Z materials used in implants, such as titanium-based, iron-based and cobalt-based alloys, and alloys used in dental implants. Since bone has a greater effective atomic number than water-like tissues, the particle transport phenomena and thus the contribution to dose distribution are different, and therefore the requirements for inhomogeneity correction in dose calculation differ from those for other tissues. The introduced uncertainties with non-biological high-Z materials have caused other types of challenges than tissues of lower density. The dose perturbation effect due to high-Z materials is usually considered to be so severe that it has become common to avoid such beam directions where the beam would first traverse the high-Z material, prior to impinging on the volume to be treated. This has been the case with hip implants in particular, when radiotherapy has been applied to the pelvic region. [2,8,122]

The particle transport phenomena and the absorbed dose deposition of electron beams differ significantly from photon beams and thus the foundations of the radiotherapy dose calculation are very distinct. The reason is that with electron

beams the number of interaction events per unit path length is much greater and therefore also the trajectory shapes are more complex. However, regardless of this, it has been common with the photon beams that materials with densities and atomic compositions significantly differing from water have also caused large uncertainties in electron beam dose calculation. Since the electron beams are usually applied to malignancies that are superficial on the skin or at shallow depths, the main interests have been related to heterogeneities such as airways, bone and lung tissue near the skin surface. Due to the physical properties of the electron beam, the high-Z materials have usually been avoided between the treatment beam and the volume to be treated, unless such materials are intentionally used for shielding. Issues related to larger uncertainties in dose calculation with electron beams have also included the consideration of small, irregular fields, oblique incident fields, extended SSD fields and both electron-electron and photon-electron treatment field junctions. [2,127]

Examples of applications utilising MC models in TPS benchmarking are found with 3D conformal radiotherapy (3D-CRT) ([128]), IMRT ([129]), head and neck IMRT and VMAT ([130-132]), prostate IMRT ([131]), total body irradiation (TBI) ([133]), SBRT of the lung ([134]) and electron radiotherapy ([135]) plans. There are studies where MC-based patient plan simulation systems are developed for all types of plan verification, including 3D-CRT ([136]), IMRT ([136-137]), electron radiotherapy ([136]), VMAT ([138-139]) and flattening filter free VMAT ([140]) techniques. The most developed MC-based patient plan calculation systems for TPS benchmarking and plan verification feature graphical user interfaces (GUIs) to ease the workflow with photon ([141-144]) and electron ([145]) beam radiotherapy. In addition, separate radiotherapy research software platforms are employed to allow the dose distribution visualisation, analysis and other applications ([146-148]).

4. THE MC MODELS FOR PHOTON AND ELECTRON BEAMS – CONSTRUCTION AND BENCHMARKING

The BEAMnrc code system was installed and run on the calculation grid of the Tampere Center for Scientific Computing (TCSC) at Tampere University of Technology (TUT) (Tampere, Finland) between 2009 and 2014. In the grid, there were 200-400 cores, including computing nodes with dual-core and six-core AMD (Advanced Micro Devices, Inc., Sunnyvale, CA, USA) Opteron processors and quad-core Intel (Intel Corporation, Santa Clara, CA, USA) Xeon processors.

The MC models were based on the Varian Clinac iX (Varian Medical Systems Inc., Palo Alto, CA, USA) medical linac commissioned in 2007 at the Unit of Radiotherapy, Department of Oncology, Tampere University Hospital (Tays) (Tampere, Finland). The manufacturer provided the author with a confidential proprietary information package (Monte Carlo Data Package: High Energy Accelerator) in 2009, and an updated version of the package followed in 2011. The package contains detailed information on the treatment head component geometries and materials. The information incorporated in the package was used in the MC models for the most part. However, geometrical details of readily accessible treatment head components that were not included in the package were measured. Those that were included were re-measured to ensure the correctness of the information. The elimination of some obvious erratic or conflicting information in the package was clarified by contacting the manufacturer.

4.1. The geometry models for photon and electron beams

In this study the MC models for photon beams of nominal energies 6/18 MV and for electron beams of nominal energies 6/9/12/16 MeV were commissioned. For 6 MV photon beam and 16 MeV electron beam the MC model commissioning is partly presented in [I] and for 6/18 MV photon and 9/16 MeV electron beam models in [149]. The geometry model is aligned so

that the Z-axis in the model is the beam CAX. The origin of the Z-axis (Z = 0 cm) is set to the upper, 'front' surface level of the X-ray target. The X- and Y-axes are set to coincide with the linac coordinate system, that is, the X-axis represents the crossplane direction and Y-axis denotes the inplane direction. Table 2 lists the treatment head components included in the geometry models and the corresponding CMs that were used to model the structures.

Table 2. The components included in the photon and electron beam geometry models and the corresponding CMs used.

Component	Photon beam model	Electron beam model
X-ray target*/vacuum**	SLABS*	SLABS**
Primary collimator	CONS3R	CONS3R
Vacuum exit window	SLABS	SLABS
Flattening filter*/scattering foil**	FLATFILT*	FLATFILT**
Dual monitor IC	CHAMBER	CHAMBER
Mirror and mirror frame with shielding	FLATFILT	FLATFILT
Secondary collimator (jaws)	SYNCJAWS	SYNCJAWS
MLC	SYNCVMLC	SYNCVMLC
Light field reticle plastic sheet	SLABS	SLABS
Interface mount	PYRAMIDS	PYRAMIDS
Electron applicator with square cutout	-	PYRAMIDS

X-ray target

The first component in the geometry model was the transmission type X-ray target. It is usually made of a high-Z material, such as tungsten or copper ([10,12,150]) (manufacturer proprietary information). The layered structure of the component was modelled with SLABS CM. Knowledge of correct layer thicknesses and materials is essential in order to model realistic beams. Since the width of the initial electron beam coming from the bending magnet system is small compared to the realistic size of the X-ray target, the size of the modelled structure is not important, that is, it can be considered a semi-infinite slab. With an electron beam the X-ray target is retracted and the whole CM is assigned as a vacuum.

Primary collimator

The fixed primary collimator, which is in vacuum, is modelled with CONS3R CM. The collimator, which is made of high-Z material, such as tungsten or lead (manufacturer proprietary information), has a conical opening directed downstream, in the direction of the beam. It defines the maximum circular beam, which is further collimated with the jaws and the MLC. As shown in

[84], the radii of the beam entrance and exit openings of the primary collimator strongly influence the beam properties, and therefore it is important to define the correct beam opening angle, which is about 28º. The lateral thickness of the structure has to be large enough for the shielding to be similar to a real linac.

Vacuum exit window

The last component in a vacuum, modelled with SLABS CM, is the thin window at the bottom of the primary collimator. The requirement for the window is to maintain a vacuum with minimal impact on the radiation beam.

Flattening filter

The fixed component that modulates the primary photon beam the most is the flattening filter, which is modelled with FLATFILT CM. In the linac treatment head it is located in the carousel, where all the flattening filters and electron beam scattering foils are found. The main function of this conical structure is to flatten the forward-peaked photon beam intensity so that the beam produces flat dose distribution at a depth of 10 cm in water phantom at SSD 100 cm ([12]). The geometry of this component is extremely detailed, with highly non-linearly shaped surface, and it is usually made of some high- or medium-Z material, e.g. lead, tungsten, steel or aluminium, or a combination of these ([10]) (manufacturer proprietary information). The coordinates and layer thicknesses for the flattening filter geometry models were interpolated using the proprietary information from the manufacturer. The position and shape of the filter are very important, since any misalignment or incorrect shape will alter beam symmetry and flatness. Figure 5 (a)-(b) shows the geometry models for the 6 MV and 18 MV flattening filter, respectively.

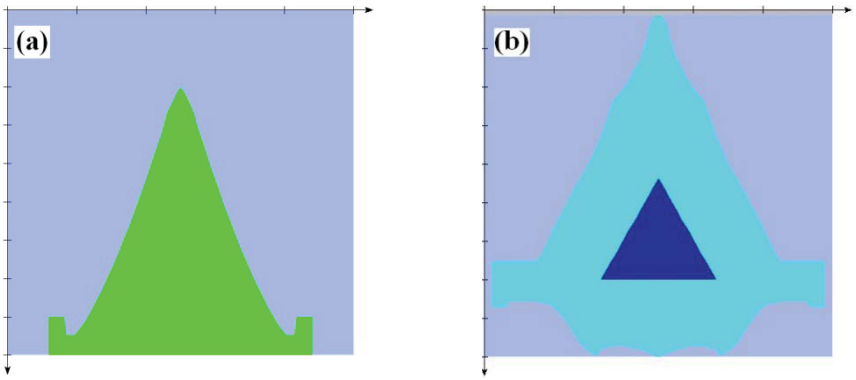

Figure 5. (a) A 6 MV flattening filter and **(b)** a 18 MV flattening filter geometry models, respectively. Note the conical insert made of a second material inside the filter in (b).

Scattering foil

The electron beam scattering foil, modelled with FLATFILT CM, is used to spread the narrow beam generating as small an amount of contaminant bremsstrahlung radiation as possible. Typically it is a two-layer structure, consisting of thin primary foil, which is made of high-Z material, such as lead ([150]) (manufacturer proprietary information), and which acts as a scatterer, followed by a secondary foil of medium-Z material (manufacturer proprietary information), which is slightly conical in shape, similar to X-ray flattening filter, thus attempting to flatten the beam. The resulting electron beam characteristics are highly sensitive to the thicknesses and materials of both scattering foils and the mutual distance ([104]). They form a set of parameters in combination with initial electron beam parameters that need to be optimised in the MC model commissioning phase. Figure 6 shows a dual scattering foil of a high energy electron beam.

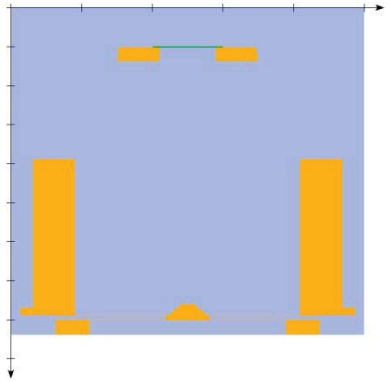

Figure 6. A dual scattering foil of a high energy electron beam.

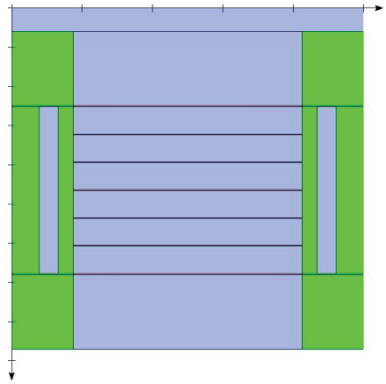

Figure 7. A dual monitor IC.

Dual monitor IC

The monitor IC, which monitors various beam parameters, consists of two stacked identical transmission parallel plate ICs in a 90º orientation relative to each other. It has a complex structure, i.e. there are number of plastic sheets with electrodes, in addition to protective cover sheets ensuring the sealing, which all are separated by very small distances. In the outer wall there are two annuli made of medium-Z material (manufacturer proprietary information). In this study CHAMBER CM was used to model the structure shown in Figure 7.

Mirror and mirror frame with shielding

In the BEAMnrc system there is a dedicated MIRROR CM for modelling the field light mirror tilted to an angle relative to the beam CAX. However, this CM does not allow the modelling of surrounding structures for the tilted mirror structure. In [84] the discrepancies in the build-up dose between the MC model and measurements with a high energy photon beam were studied. One of the conclusions was that the underestimation of the build-up dose was due to deficiencies in electron contamination modelling. A partial solution to this was to include the complex-shaped lead shield around the mirror in the MC model, which was implemented with a simplified conical structure with the mirror with its frame as a horizontal annulus. The approach was also implemented in this study (Figure 8) and therefore instead of MIRROR CM, FLATFILT CM was used to model the structure. The beam opening angle, defined by the plastic mirror sheet and its frame made of medium-Z material (manufacturer proprietary information), was projected on a horizontal level, as were the thicknesses of the corresponding structures. The opening angle of the surrounding conical structure made of high-Z material (manufacturer proprietary information) was matched to that of the primary collimator.

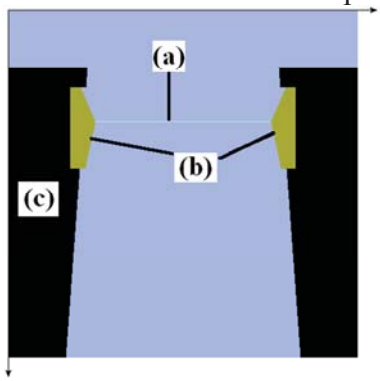

Figure 8. The mirror **(a)**, mirror frame **(b)** and the surrounding shielding **(c)**.

Secondary collimator (jaws)

The jaws were modelled with SYNCJAWS CM. They comprise two pairs of high-Z material, such as lead or tungsten ([10]) (manufacturer proprietary information), blocks, downstream from the mirror and mirror frame with the surrounding shielding structure. First there are the Y jaws in an inplane direction, and downstream there are the X jaws in a crossplane direction. The jaws are the first component from the top in the treatment head that are considered to be patient-specific beam-modifying components, which means that any rectangular field size ranging between 0 x 0 cm^2 and 40 x 40 cm^2 can be collimated with them. The Y jaws move about an arc, with the origin being

in the X-ray target, the jaw edge always being parallel to the radial line drawn through the X-ray target. The X jaws move along a horizontal line, pivoting so that the jaw edge is parallel to the Y jaws. The geometrical equations to calculate the jaw positions in the jaw level from the positions at the isocentre (SSD = 100 cm) level defined by the TPS were implemented into a separate script. The feature that allows the synchronised movement of the jaws with other components, the source and the phantom is described in Section 3.1.2.2.

MLC

The MC MLC model of Varian Millennium 120 MLC consists of 60 pairs of separate leaves made of high-Z material (manufacturer proprietary information), modelled with SYNCVMLC CM. The MLC is the most complex structure to model of the beam-modifying components. The detailed model takes into account separately with different leaf types the tongues and grooves and driving screw holes. In addition, for round leaf ends, the leaf curvature radius has to be set, as does the focus point for the focused leaves (i.e. if the imaginary lines drawn through leaf edges intersect at one point), and the interleaf air gap for all leaves. The MLC positions for the simulations are usually extracted from the TPS, which defines them at the isocentre level. Again, as with jaws, this information was converted to the MLC level using the isocentre ratio, which is the SSD divided by the distance from the source level to the MLC level. However, due to issues related to the differences in the apertures defined by the field light and radiation beam, defined by the rounded leaf ends, i.e. the isocentre ratio changes as a function of the aperture size, the geometrical equations based on the work by Boyer et al. ([151]) were further empirically verified, taking into account the individual calibration of the MLC. The results of the required individual benchmarking of the MC MLC model (Figure 9 (a)-(b)) are shown in Section 5.1.

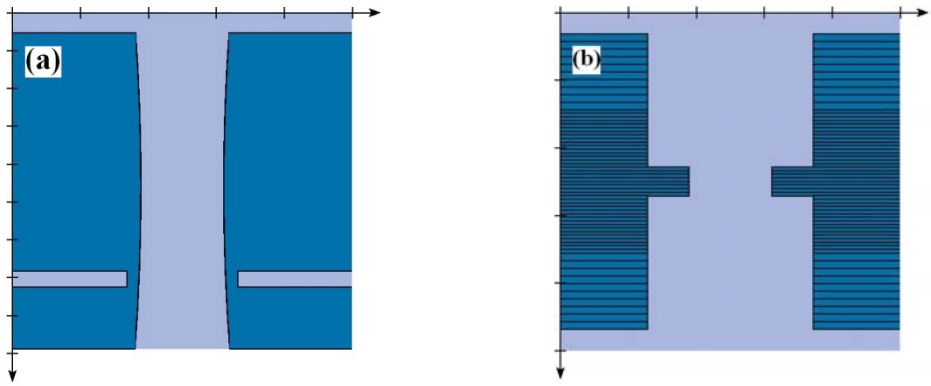

Figure 9. The MC MLC model **(a)** from the side and **(b)** from the BEV.

Light field reticle plastic sheet

The last component from the top in the beam path for the photon beam is the light field reticle and the plastic sheet. The thin sheet made of plastic (manufacturer proprietary information) was modelled with SLABS CM.

Interface mount

To complement the photon beam treatment head MC model, the interface mount directly below the light field reticle plastic sheet was modelled with PYRAMIDS CM. The dimension of the aperture and structures were manually measured and a medium-Z material was assigned.

Electron applicator with square cutout

To complement the electron beam treatment head MC model, in addition to the interface mount, the electron applicator with an electron cutout was modelled. The dedicated APPLICAT CM was not utilised in this study, since the bevelled edges of the scrapers and cutout cannot be modelled with the CM ([20]). Therefore, the more general purpose PYRAMIDS CM was applied (Figure 10). The first and second scrapers were assigned a medium-Z material and the third scraper was replaced by the cutout material, which is a modified version of Cerrobend-type low melting point alloy ([152-153]) (manufacturer proprietary information).

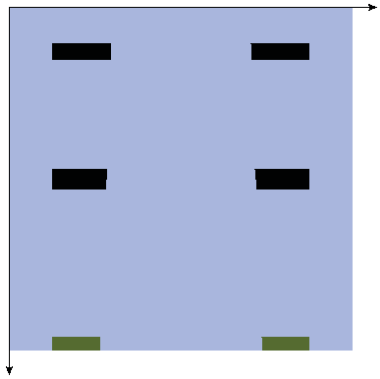

Figure 10. The electron applicator with square cutout.

Figure 11 (a)-(b) shows the complete treatment head models. The jaws have been oriented in same direction for visualisation purposes. The MC geometry models for both photon and electron beams and all beam energies are identical for the following components: primary collimator, vacuum exit window, dual monitor IC, mirror with its frame and surrounding shielding, jaws, MLC, light field reticle plastic sheet and interface mount.

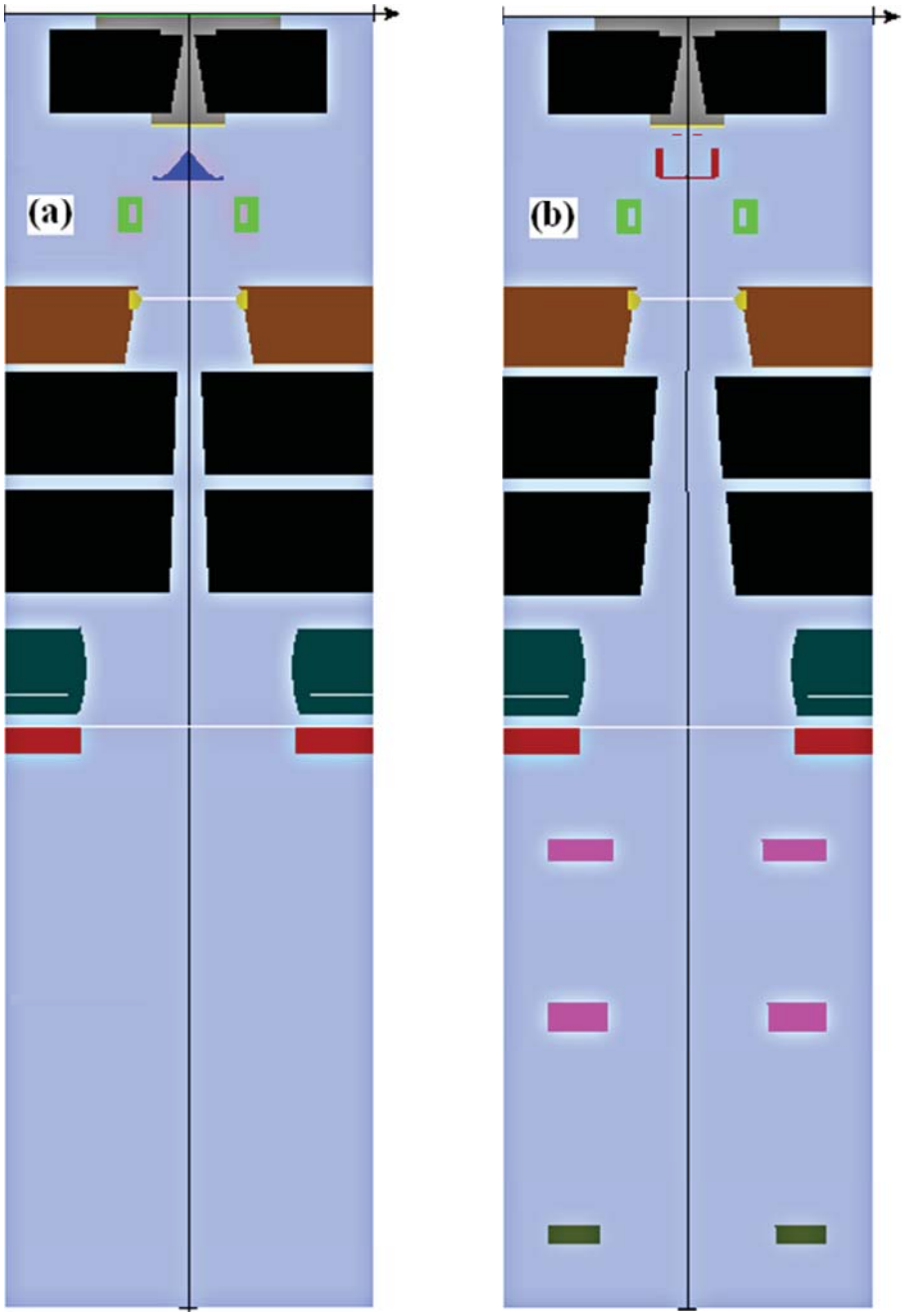

Figure 11. Varian Clinac iX MC geometry models for **(a)** the photon and **(b)** the electron beam (for explanation, see text).

4.2. Benchmarking the MC model against measurements – PDDs and profiles in water phantom

One of the goals of this work was to build MC geometry models that would represent the modelled linac as realistically as possible. Once the models were assembled, the next step was to determine the initial electron beam and other simulation parameters. With regard to EGSnrc-based physics modelling (Section 3.1.1.), the goal was also to simulate the radiation transport as realistically as possible, without many compromises, to reduce calculation times, for example. The parameters shown in Table 3 were selected with BEAMnrc code system version 2013 in all simulations.

Table 3. EGSnrc physics modelling parameters used in this study.

EGSnrc MC transport parameter	Value
Global ECUT	0.521/0.561/0.700 MeV
Global PCUT	0.01 MeV
ESTEPE	0.25
XIMAX	0.5
Boundary crossing algorithm	EXACT
Skin depth for BCA	3
Electron-step algorithm	PRESTA-II
Spin effects	On
Brems angular sampling	KM
Brems cross-sections	NRC
Triplet production	On
Bound Compton scattering	On
Compton cross-sections	default
Radiative Compton corrections	Off
Pair angular sampling	KM
Pair cross-sections	NRC
Photoelectron angular sampling	On
Rayleigh scattering	On
Atomic relaxations	On
Electron impact ionisation	On
Photon cross-sections	xcom

Some of the chosen values represent the default values of the system ([20]), but for many parameters, for which the default value is 'off', the option 'on' has been selected. For Global ECUT there were three values, for which an explanation is that in all the other simulations than in the DOSXYZnrc (0.700 MeV) and BEAMnrc phase space B (0.561 MeV) (see Section 4.3.) simulations performed in [III], the value was 0.521 MeV. Many of the parameter choices

are claimed to be significant only at low energy ranges, but since there is no exact upper limit for this energy range and there is always a low energy component present in the simulations, the options were turned on to better reflect the realistic radiation transport ([20,154]).

After selecting the EGSnrc parameters, the iterative initial electron beam parameter tuning was performed. The scheme described in Section 3.2. was applied. It was commenced by tuning the initial electron beam spectrum, the mean energy to be precise, for the 10 x 10 cm^2 field with photon beams and the A20 applicator for the electron beams (which defines a 20 x 20 cm^2 field at SSD = 100 cm). Once a match for PDD was found, an energy spectrum with a 3% FWHM spread was applied to represent the mechanical energy slit present in the bending magnet system that absorbs electrons falling outside this energy range. The beam profiles were matched for the same field sizes by varying the initial electron beam width FWHM value and the divergence. Concurrently, the matches for the PDDs were monitored, and the energy spectrum was modified as well, if needed. With photon beams, the beam profiles were also bench-marked for varying depths and field sizes. The calculation grid sizes were adapted to account for the varying dose gradients, being small (from 0.05 cm to 0.1 cm) in high dose gradient regions and greater in other regions. The reported statistical uncertainties were less than 0.2% in PDD curves, less than 0.5% in high dose regions in dose profiles, and from 1% to 2% in dose profile out-of-field regions. The measured and calculated PDD curves were normalised to the depth of 10 cm with photon beams and to d_{max} with electron beams. The dose profiles were normalised to 100% at a measured or calculated value, which was an average of three to five values around the beam CAX.

All the reference PDD measurements were performed using a motorised scanning system in a PTW MP3 (PTW Freiburg GmbH, Germany) water phantom. A PTW TM31002 Semiflex 0.125 cm^3 IC (PTW Semiflex IC) (PTW Freiburg GmbH, Germany) served as reference detector with a 6 MV photon beam for 10 x 10 cm^2 and 30 x 30 cm^2 fields and for a 3 x 3 cm^2 field an IBA unshielded stereotactic semiconductor field detector (model DEB050) (IBA SFD) (IBA Dosimetry AB, Sweden) was used. In addition, to study the performance of the MC model in the build-up dose modelling, the build-up dose for the 10 x 10 cm^2 field for 6 MV photon beam was point-measured in Gammex Standard Grade Solid Water® 457 (Gammex/RMI, Middleton, WI, USA) with Gafchromic® EBT radiochromic film (Ashland Specialty Ingredients, Wilmington, DE, USA). Therefore, the reference PDD curve was a combination of interpolated film measurement data and IC measurement values. With the 18 MV photon beam, the PTW Semiflex IC was used as reference detector for all PDD measurements. With electron beams the reference PDD

curves were measured with an IBA unshielded electron semiconductor field detector (model DEB000) (IBA EFD) (IBA Dosimetry AB, Sweden).

In the dose profile measurements, the IBA SFD was used as a reference detector for 3 x 3 cm^2 fields with photon beams, while the PTW Semiflex IC was utilised for other field sizes. With photon beams, the measurement depth was 10 cm. With electron beams the dose profile data was measured at d_{max} with the PTW Semiflex IC for 9/16 MeV beam energies, and with IBA EFD for 6/12 MeV beam energies, in order to study the applicability of both detectors for electron beam dose profile measurements for QA purposes.

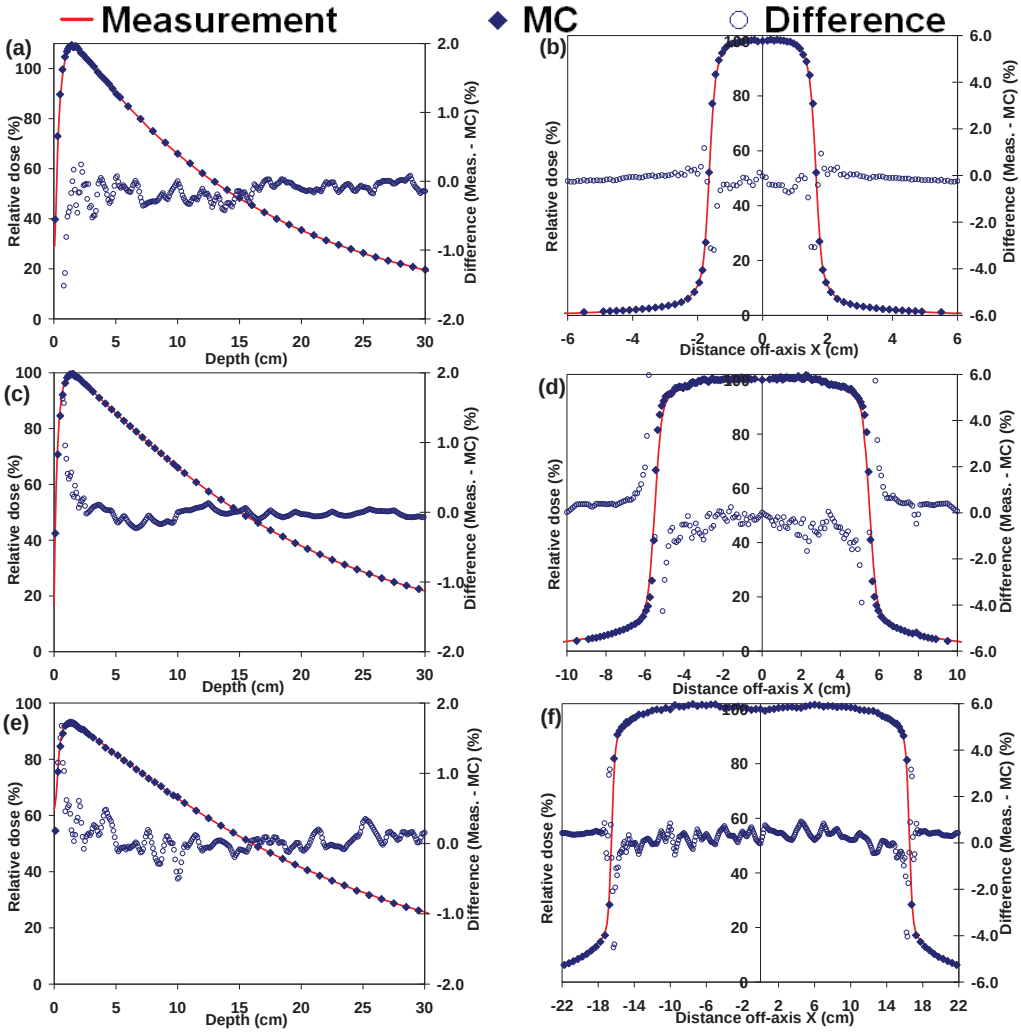

Figure 12. Benchmarking results for the 6 MV photon beam MC model: **(a)-(b)** PDD and dose profile for 3 x 3 cm^2 field, **(c)-(d)** PDD and dose profile for 10 x 10 cm^2 field and **(e)-(f)** PDD and dose profile for 30 x 30 cm^2 field.

For the 6 MV photon beam MC model, the results for the benchmarking are presented in Figure 12. In PDDs the discrepancies were less than 0.5% of D_{max} at depths greater than 1.0 cm (d_{max} = 1.4 cm), usually being from 0.1% to 0.2% of D_{max}, especially for the 10 x 10 cm^2 field. From the depth of 1.0 cm towards the surface the differences increases, which is due to the MC model producing greater PDD values than the IBA SFD and smaller PDD values than the EBT film and the PTW Semiflex IC. In the dose profiles, when neglecting the penumbral regions, the discrepancies were generally less than 0.5% of D_{max}, apart from several points in the dose profile for 10 x 10 cm^2 field. In penumbrae, the DTA values were 0.2 mm for the smallest field and less than 1.0 mm for larger fields.

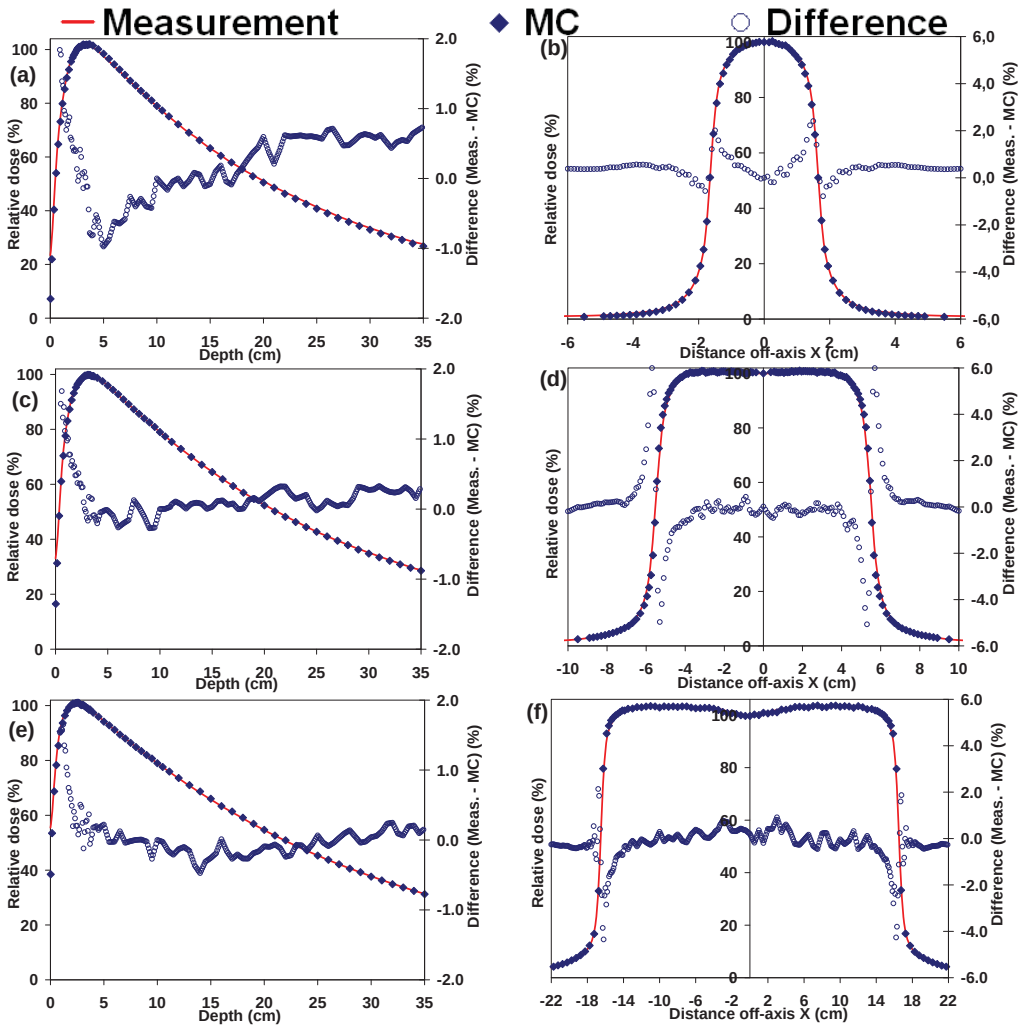

Figure 13. Benchmarking results for the 18 MV photon beam MC model: **(a)-(b)** PDD and dose profile for 3 x 3 cm^2 field, **(c)-(d)** PDD and dose profile for 10 x 10 cm^2 field and **(e)-(f)** PDD and dose profile for 30 x 30 cm^2 field.

With the 18 MV photon beam, the benchmarking results for the MC model are presented in Figure 13. In PDDs the discrepancies were less than 1.0% of D_{max} at depths greater than 1.0 cm (d_{max} = 3.0 cm), usually being from 0.2% to 0.4% of D_{max}, especially for the 10 x 10 cm^2 and 30 x 30 cm^2 fields. From the depth of 1.0 cm towards the surface the differences increase, which is due to the MC model producing smaller PDD values than the PTW Semiflex IC. For the dose profiles the discrepancies were less than 0.5% of D_{max}. In penumbrae the DTA values are 0.3 mm for the smallest field and less than 1.0 mm for larger fields.

An electron beam PDD curve has three parts: 1) the build-up region, where the dose increases to the D_{max}, 2) the 'build-down' region with large dose gradient, where the dose diminishes, and 3) the flat contamination X-ray 'tail' of the curve. Figure 14 shows the comparison data for the electron beam MC model. For electron beam energies other than 6 MeV, the discrepancies in the build-up region are less than 0.7% of D_{max}. For the 6 MeV beam in the build-up region, the MC model produces between 0% and 2.0% of D_{max} higher PDD values than the IBA EFD. In the dose 'build-down' region, the discrepancies are less than 1.0% of D_{max}, being even smaller for 12 MeV and 16 MeV beams. In the X-ray 'tails' for all the beam energies, the discrepancies are small when compared to measurements. In dose profiles the deviations are smaller than 0.3% of D_{max} and in penumbrae the DTA values are less than 0.5 mm for all energies.

The initial electron beam parameters for all the photon and electron beam MC models are shown in Table 4. ISOURC = 19 was applied to all the MC models. For the 6 MV photon beam, the final energy spectrum had a negatively skewed Gaussian shape, having a lower energy 'tail', peaking at the energy of 5.9 MeV. It did not differ much from the Gaussian energy spectrum, with 5.9 MeV mean energy and 3% FWHM energy spread, but it produced slightly more congruent results compared to some benchmarking measurements. For the 6 MV photon and 16 MeV electron beam models the commissioning is partly presented in [I] and for 6/18 MV photon and 9/16 MeV electron beam models in [149].

Table 4. The initial electron beam parameters for the MC models.

Parameter	6 MV	18 MV	6 MeV	9 MeV	12 MeV	16 MeV
Width, FWHM (mm)	0.7	1.3	2.0	1.5	0.6	0.7
Mean angular spread (°)	0.5	0.0	0.2	0.2	0.2	0.0
Energy spectrum shape	LinLog	Gaussian	Gaussian	Gaussian	Gaussian	Gaussian
Mean energy, (MeV)	-	17.80	7.02	9.95	13.50	17.66
Energy spread, FWHM (%)	-	3.00	3.00	3.00	3.00	3.00

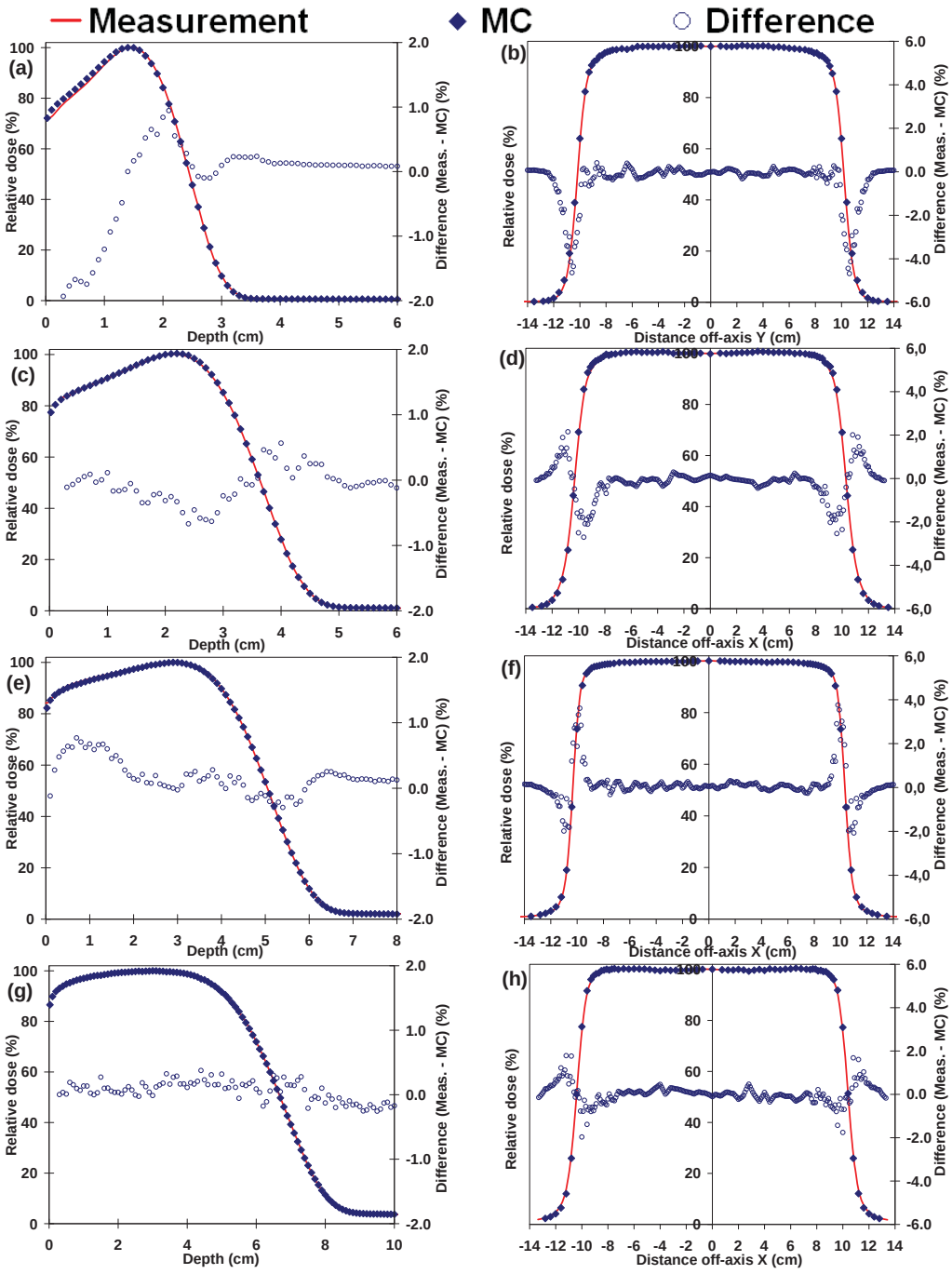

Figure 14. Benchmarking results for the electron beam MC model: PDDs and dose profiles for 6 MeV (**(a)-(b)**), 9 MeV (**(c)-(d)**), 12 MeV (**(e)-(f)**) and 16 MeV (**(g)-(h)**).

4.3. Absolute dose calibration

A monitor unit (MU) represents the radiation output of a linac. It is a measure that is related to the calibration of the monitor IC and usually the definition is that 100 MU is equivalent to a measured absolute dose of 1 Gray (Gy) in some reference conditions, i.e. at reference SSD, with the reference field size and at reference depth. This information is an integral part of the input data required for TPS commissioning and the amount of radiation delivered by each field, which is calculated by the TPS system, is transferred to the linac in MUs. [10]

In the BEAMnrc code system the calculated absorbed dose (in Gy) is normalised by the number of particles from the original source, i.e. in the case of linac simulations in this work, the number of electrons that are incident originally on the X-ray target with photon beams and on the vacuum slab replacing the X-ray target with electron beams. In order to perform full-scale TPS benchmarking with the MC model, an absolute dose calibration of the MC model is essential. In its simplest form, the user could simulate the dose distribution to represent an absolute dose calibration measurement set-up, determine the conversion factor with the MC-calculated dose in a voxel representing the active volume of the detector, and use the factor to normalise the dose distributions. However, with many types of linacs, as with the one used in this work, the linac output is affected by the backscattered radiation from the secondary and tertiary collimators, mainly from Y jaws, to the monitor IC. Therefore, the required number of MUs accumulates sooner and the linac beam is switched off earlier. This factor is included in the measured output factors, which describe the field or aperture size dependence of the linac output. [2-3,12] When output factors are determined with MC models, agreement levels of 1-3% over a broad field size range have been reported ([58,79,155-156]).

A formalism, with which the absolute dose calibration of the MC models in this study is performed, is presented in [157]. The rigorous method is based on the linac simulation in two steps. In the first simulation the phase space is collected below all the fixed components in the treatment head (phspA), i.e. below the mirror with the frame, surrounded by the shielding. In this simulation the dose is scored in the active, charge-collecting air-filled volume of the monitor IC, deposited by the forward-directed particles. In the second simulation the phspA is used as a source and the geometry model includes the monitor IC and the mirror with accompanying structures upstream from the source plane and all the beam-modifying components, such as the jaws, the MLC and the electron applicator, downstream from the source plane. The resulting phase space

(phspB) located below all the treatment head components can thereafter be utilised as a source in phantom dose calculations. In the phspB simulation the dose is again scored in the monitor IC, as in phspA simulation, but now it corresponds to the backscattered dose to the monitor IC, which is dependent on the positions of the collimators. When performing these simulations in the reference absolute dose measurements set-up, the relationship between the dose calibration and MUs can be established for the MC model. This data can subsequently be used with other field configuration simulations applying the dose-MU equation according to [157].

In [157] the reported deviations between the measured and calculated square field output factors were less than 1.5%. In this work, the output factors were determined with the MC model for selected field sizes and compared to measurements. The results are shown in Tables 5 and 6.

Table 5. The calculated and measured (IBA SFD (3 x 3 cm^2) and PTW Semiflex IC (10 x 10 cm^2 and 30 x 30 cm^2)) output factors for 6 MV and 18 MV photon beams with percentage differences. The output factors are normalised to the value for 10 x 10 cm^2 field.

	3 x 3 cm^2			**30 x 30 cm^2**		
	Meas.	**MC**	**Difference**	**Meas.**	**MC**	**Difference**
6 MV	0.868	0.873	0.61%	1.100	1.104	0.35%
18 MV	0.842	0.846	0.45%	1.088	1.094	0.51%

Table 6. The calculated and measured (PTW Roos TM34001 parallel plate IC) output factors for 6 MeV, 9 MeV, 12 MeV and 16 MeV electron beams with percentage differences. The output factors are normalised to the value for the field defined by the A20 applicator.

	A10 applicator		
	Meas.	**MC**	**Difference**
6 MeV	1.013	1.016	0.30%
9 MeV	0.985	0.988	0.26%
12 MeV	0.980	0.985	0.53%
16 MeV	0.976	0.981	0.49%

For all the MC models the discrepancies in the output factors are around or less than 0.5%, when compared to the measurements. For both photon and electron beams, the MC models produce larger output factors than the measurements.

5. APPLICATION OF THE MONTE CARLO MODELS TO SPECIFIC CASES IN RADIOTHERAPY

5.1. Dosimetry

The MC models have been extensively used to provide more information on various issues in dosimetry. Since the resolution of the calculated dose distribution is very adaptable, calculation grids with small dimensions enable the use of the MC models in small field/aperture dosimetry benchmarking. In the commissioning benchmarking phase of the MC MLC model for this work, a wide selection of detectors was used. First the evaluation was done with static MLC-shaped fields to assess the accuracy of the various parameters defining the MC MLC geometry model. To evaluate the accuracy of the geometric shape and position of the leaves and leaf transmission in the MC model, separate MLC-shaped fields in both crossplane and inplane directions were prepared and measured. Since the apertures with single or few MLC leaves are small, high resolution was a primary requirement for measurements. The most important properties of the used detectors, in addition to the other detectors used during the commissioning of the MC models, are presented in Table 7.

Table 7. Summary of detectors used and their most important properties.

	PTW Farmer	PTW Semiflex	PTW Roos	PTW LIC	IBA EFD	IBA SFD	Gafchromic® EBT2
Sensitive material	air	air	air	iso-octane	silicon	silicon	radiochromic film
Active volume (mm^3)	600	125	350	1.7	0.29	0.017	-
Active volume size (mm)	6.1	5.5	15	2.5	2.0	0.6	0.8*
Density (g/cm^3)	0.001	0.001	0.001	0.692	2.329	2.329	1.2

* The film dosimetry system readout spatial resolution

The PTW Semiflex IC was partly used as the basic detector, but better resolution was pursued with IBA SFD, Gafchromic® EBT2 radiochromic film (Ashland Specialty Ingredients, Wilmington, DE, USA) and PTW microLion

liquid-filled IC (LIC) (PTW Freiburg GmbH, Germany). Since there are disadvantageous issues identified with all the detectors, the MC model was compared to the most reliable detector in each field and field region, and if an agreement was found, at the same time the MC model was used as a reference for other detectors. The test field in Figure 15 (a) was to ensure the leaf positions in crossplane and inplane directions ('L-shaped' field), and the final static test field in Figure 15 (b) represented a complex-shaped field with varying apertures ('grid-shaped' field).

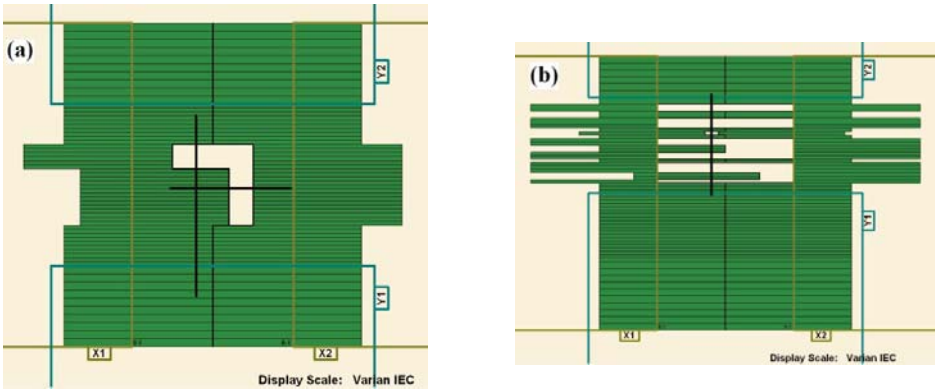

Figure 15. BEV visualisations of test fields for the MC MLC model benchmarking: **(a)** L-shaped and **(b)** grid-shaped field.

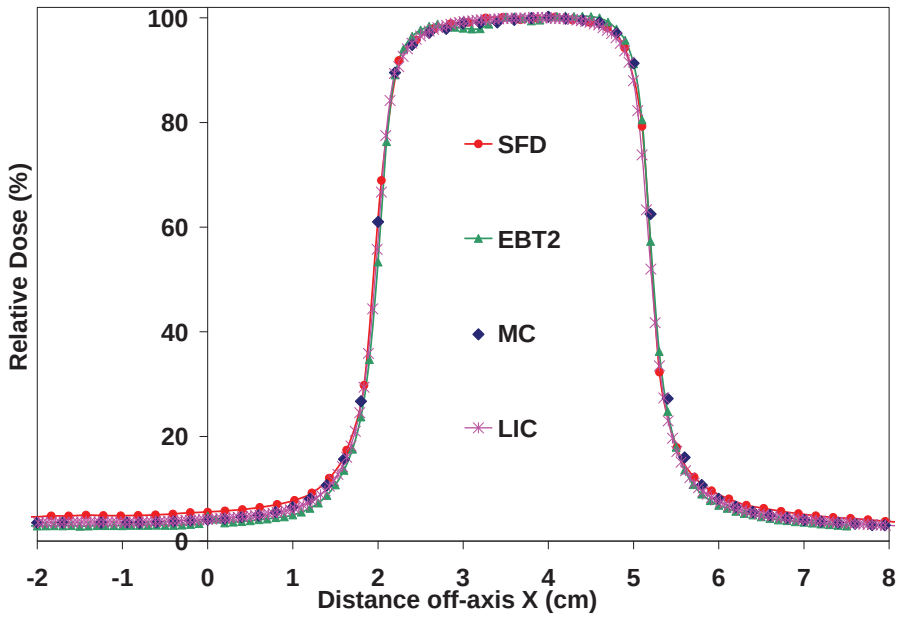

Figure 16. The relative crossplane dose profiles for the MC model and measurements for the L-shaped field.

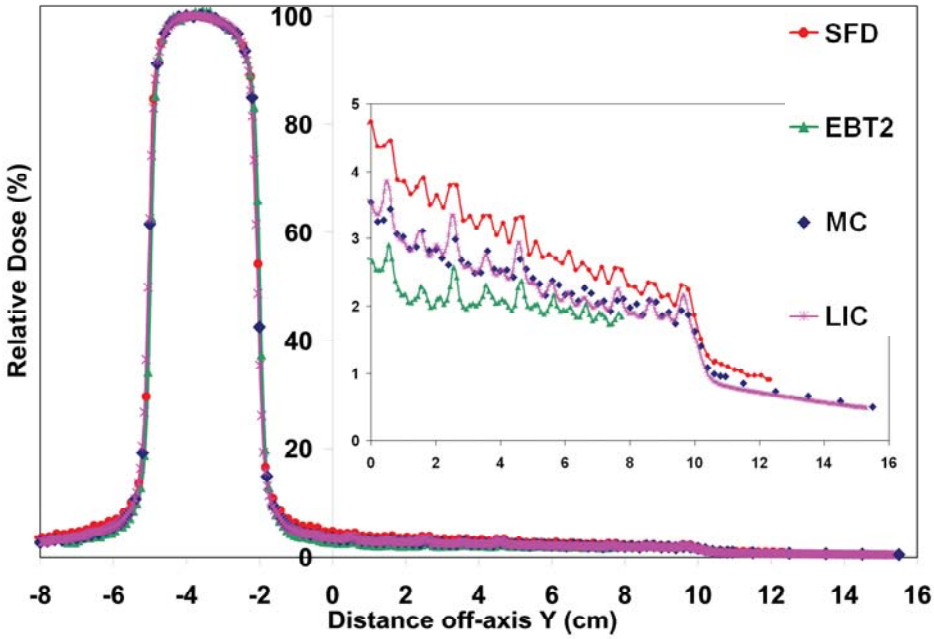

Figure 17. The relative inplane dose profiles for the MC model and measurements for the L-shaped field. The insert is a magnification of the out-of-field region.

In Figures 16 and 17 it can be seen that the MC MLC model is able to reproduce the leaf positions defined by the test fields. The field aperture penumbrae are congruent with all the measurement techniques. However, in the out-of-field regions in both test fields, clear discrepancies are observable between the measurement techniques. In the insert in Figure 17 there is a magnification of this region – from 0 cm to +10 cm collimated by the MLC and from +10 cm to +16 cm collimated by both the jaws and the MLC. The former region benchmarks the MC model with regard to the interleaf leakage and leaf transmission. The insert also shows that the dose profile pattern due to interleaf leakage is effectively reproduced by the MC MLC model, when compared to all measurements. For the leaf transmission, the MC MLC model coincides with the LIC. The LIC was tested against PTW Semiflex IC with a jaw-collimated square field out-of-field region and an agreement of 0.2% of D_{max} was found. This suggests that the leaf transmission is correctly modelled with the MC MLC model, while the IBA SFD and Gafchromic EBT2 are found to over- and underestimate the dose levels, respectively. In the latter region the jaw collimation is added and the LIC and the MC model are also congruent in this region, while the IBA SFD overestimates the dose level. These results are partly found in preliminary form in [158].

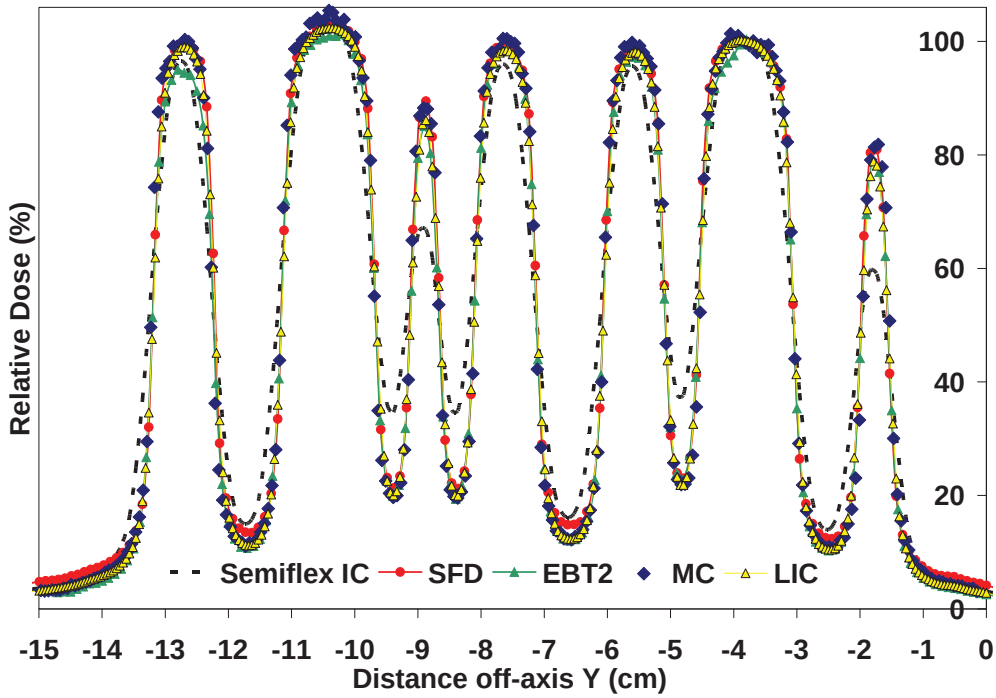

Figure 18. The relative inplane dose profiles for the MC model and measurements for the grid-shaped field.

Figure 18 presents the profiles for the complex-shaped test field. The limited resolution of the PTW Semiflex IC due to the volume averaging effect is clearly seen, especially in the apertures and closures of one leaf pair. In the leaf closures and out-of-field regions, the IBA SFD shows similar overestimation as the L-shaped field, but in the apertures it produces the best congruence with the MC model because of the smallest size of the active volume in the detector. The Gafchromic EBT2 film is congruent with the LIC in regions close to the beam CAX, but it shows dose underestimation, especially in leaf apertures further away from the beam CAX. The LIC shows the best overall congruence with the MC model throughout the dose profile.

While the rigorously commissioned MC model can be used as a reference in small field/aperture dosimetry for various detectors, it is also a choice of reference method for dynamic MLC fields. For this purpose a highly modulated IMRT field was prepared (Figure 19 (a)). The field dose distribution was first measured using an IC array detector (IBA I'm*RT* MatriXX, IBA Dosimetry AB, Sweden), consisting of 1020 ICs placed in a 32 x 32 grid, with 0.7619 cm spatial resolution. The field was simulated with the MC model in virtual water phantom with a similar spatial resolution. The dose distributions were

interpolated to a finer grid (0.1 cm x 0.1 cm) and normalised to the same average dose value in a small flat dose region. Then, a 2D gamma comparison with a 3% dose difference and a 3 mm DTA (3%/3 mm) acceptance criteria was applied ([159-160]). Of all the analysed grid points, 98.6% fulfilled the criteria.

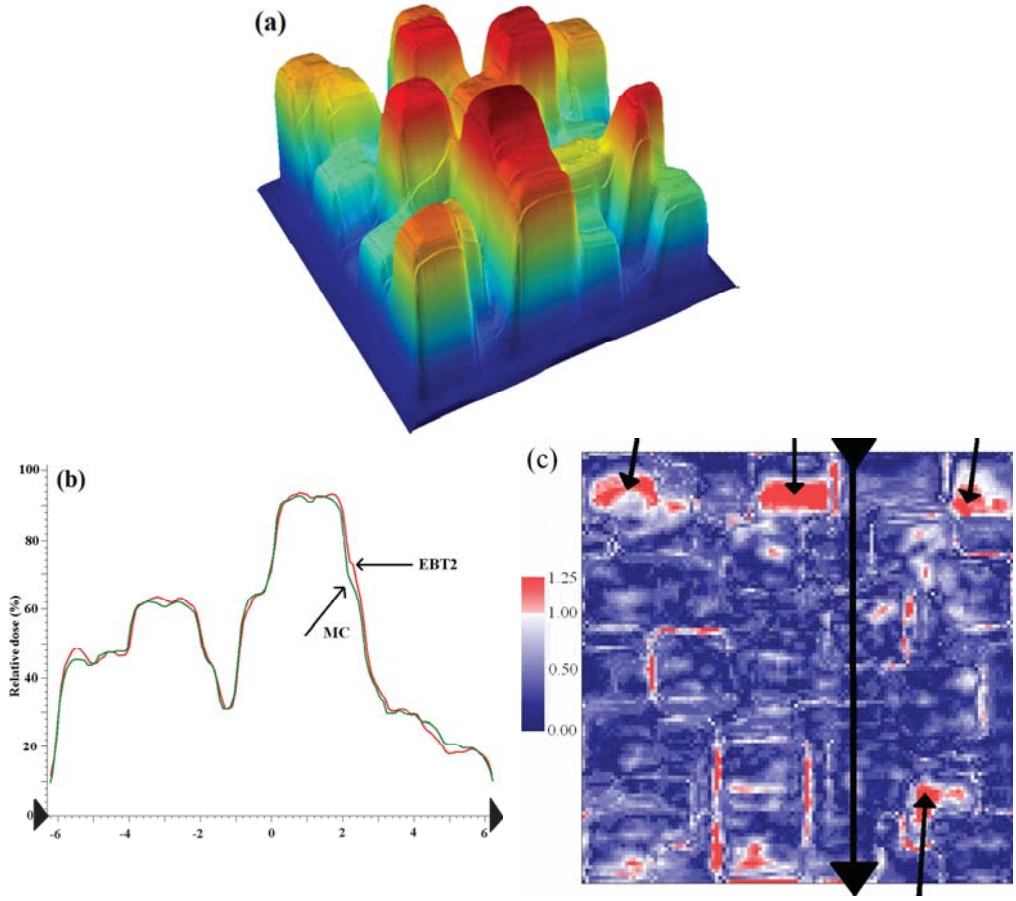

Figure 19. (a) A 3D visualisation of the IMRT field used in benchmarking. **(b)** shows the relative dose profiles in an inplane direction for the MC model, and the film dosimetry system is shown by the black line with arrows in **(c)**, which is a 2D gamma map where the red areas are the points that do not fulfil the acceptance criteria.

However, since the IC array detector suffers from relatively coarse spatial resolution, when fields with small apertures are to be measured, the MC model was applied to the benchmarking of a Gafchromic EBT2 film dosimetry system, which was based on an in-house-built densitometer ([161]). The IMRT field shown in Figure 19 (a) was measured with the system and simulated with the MC model. In MC simulation the calculation grid size was 0.08 cm x 0.08 cm, which was equivalent to the film dosimetry system readout grid size. Both dose

distributions were smoothed using the 3 x 3 matrix median filter, converted to grids of 0.1 cm x 0.1 cm by linear interpolation and normalised to give 100% at the point of maximum dose. The 2D gamma analysis was performed with an acceptance criteria of 3%/3 mm, for which the resulting gamma map is shown in Figure 19 (c). Of all the analysed grid points, 94.3% fulfilled the criteria. In the upper portion of the map there is a horizontal region (shown with arrows), where a large portion of values not fulfilling the criteria is located, which is most probably due to a minor malfunction in a single leaf motion. When leaving that region out of the analysis, 96.6% of the points fulfil the criteria. The dose profiles in Figure 19 (b) show the agreement between the MC model and the film dosimetry system.

5.2. Photon beam dose calculation

The challenges related to the accuracy of dose calculation in the presence of low-density materials are emphasised in the SBRT of the lung. In the SBRT of the lung, small field apertures are delivered from multiple directions and in most cases the fields propagate notable distances in the lung tissue prior to impinging on the volume to be treated. For this purpose, three clinical photon beam dose calculation algorithms of different generations, implemented in a commercial radiotherapy TPS, Varian Eclipse™ version 10.0 (Varian Medical Systems Inc., Palo Alto, CA, USA), were benchmarked. [II] The Pencil Beam Convolution (PBC) algorithm is an analytical correction-based 'type a' algorithm, in which the dose is calculated by convoluting the field intensity fluence with narrow pencil beam kernels. Subsequently, corrections for patient surface obliquity and heterogeneities are performed. [162-164] The PBC algorithm represented the first generation of the evaluated algorithms and it was used in dose calculations for the SBRT of the lung from 1999 to 2011 at Tays. The Analytical Anisotropic Algorithm (AAA) is a semi-analytical model-based 'type b' algorithm, although its core is built on exploiting pencil beams. The pencil beams are derived from MC simulations, fitted to user-supplied beam measurements, after which three separate sub-sources – primary photons, extra-focal photons and electron contamination – are modelled. Heterogeneity correction in the AAA is partly similar to the one in the PBC algorithm, but to some extent, it also takes the scattered radiation from the surroundings of the calculation point into account, i.e. in the lateral scaling of the medium it applies six independent exponential functions to account for the lateral transport of energy with varying densities. [165-167] The AAA represented the second generation of the evaluated algorithms and it has been used in dose calculations for the SBRT of the lung since 2011 at Tays. The Acuros XB (AXB) algorithm is a non-analytical model-based 'type c' algorithm (see definition in [III]),

which deterministically solves the coupled system of LBTEs. It uses the same sub-source models as implemented in the AAA, but in the patient dose calculation the following steps are performed: 1) transport of source model fluence into the patient, 2) calculation of scattered photon fluence in the patient, 3) calculation of scattered electron fluence in the patient, and 4) dose calculation. In the AXB algorithm the heterogeneity correction explicitly models the physical interactions of radiation with matter and thus the report mode for the final dose distribution is referred to as dose-to-medium in medium ($D_{m,m}$). Although the AXB algorithm inherently calculates $D_{m,m}$, the dose distributions can be converted to dose-to-water in medium ($D_{w,m}$), which is performed by replacing the medium-based fluence-to-dose response function used in absorbed dose calculation with a water-based response function. In the PBC algorithm and in the AAA, the dose report mode is also $D_{w,m}$, but in those algorithms the dose results are based on electron density-based corrections applied to dose kernels calculated in water. [11,168-169] The AXB algorithm represented the third, most recent generation of the evaluated algorithms and it is currently in its commissioning phase at Tays. [II]

Dose distributions from full MC simulations were regarded as a reference for the accuracy assessment. The first phase of the study included four patients diagnosed with varying-sized central lung tumours. For the patients, treatment plans that applied the 3D-CRT technique using 6 MV photon beams were made using the AXB algorithm. The planning criteria were in accordance with the Nordic SBRT study group, adapted from the original work published in [170]. The plans were recalculated (with same number of MUs and identical field settings) using the MC model. To assess the accuracy of the AXB algorithm, the original AXB-calculated dose distributions were compared to the MC-calculated dose distributions with 3D gamma comparison with 3%/3 mm and 2%/2 mm acceptance criteria and with the dose volume histogram (DVH) parameter comparison. [II]

An example of an SBRT plan isodose distribution recalculated with the MC model is shown in Figure 20 (a). In general, the agreement between the AXB algorithm and the MC model was good for larger planning target volumes (PTVs). The 3D gamma agreement index (GAI) was over 99% and 94% for both plans with acceptance criteria 3%/3 mm and 2%/2 mm, respectively. For plans with smaller PTVs, the discrepancies were greater, especially for the plan with PTV of 15.1 cc in size (Figure 20 (b)). However, the GAI result with 3%/3 mm criteria was over 95% for both plans. With DVH parameters for the OARs the deviations were 1.5% or less for all plans. The largest differences occurred with the DVH parameters for the PTV. [II]

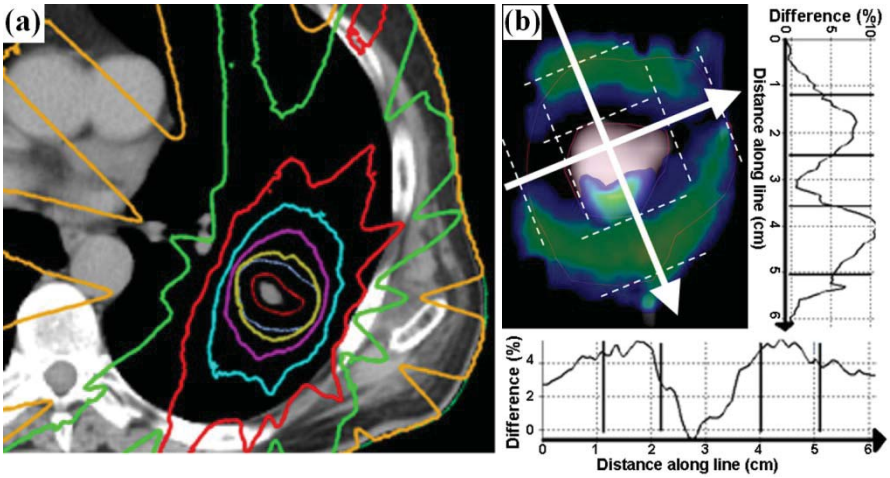

Figure 20. (a) The isodoses calculated by the MC model for the plan with medium-sized PTV. There are six dose levels starting from 5 Gy in 10 Gy increments from the outermost isodose curve. **(b)** A sagittal plane showing coloured areas where the gamma calculation typically failed (threshold criteria 3%/3 mm). The graphs along the lines show the percentage dose difference between the MC-recalculated AXB plan and the original AXB plan. Lines in the profiles represent the PTV and the GTV (gross tumour volume) boundaries. [II]

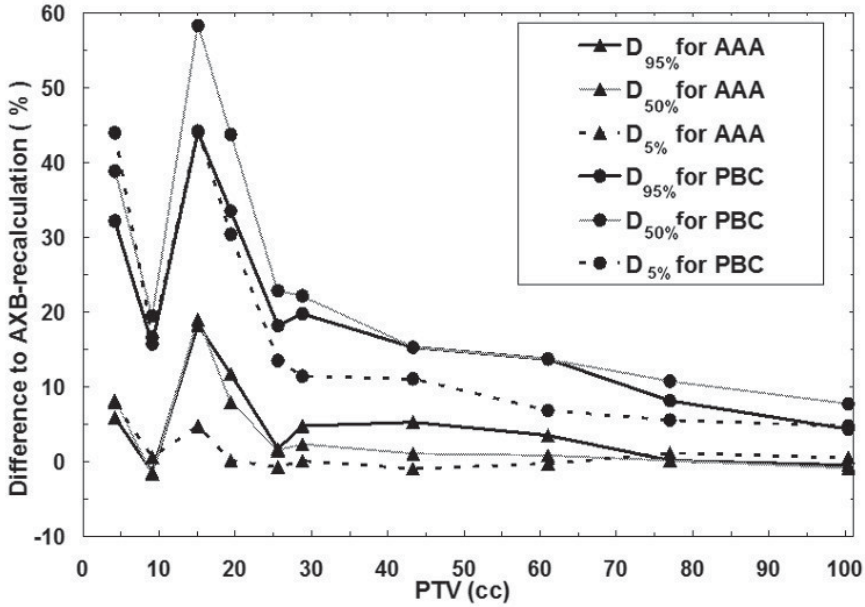

Figure 21. Comparison of the results for the algorithms as a function of the PTV size. Lines with triangles represent the differences for $D_{95\%}$, $D_{50\%}$ and $D_{5\%}$ between the AAA and the AXB-recalculated AAA-plan and lines with circles represent the differences for $D_{95\%}$, $D_{50\%}$ and $D_{5\%}$ between the PBC algorithm and the AXB-recalculated PBC-plan. Solid lines are for $D_{95\%}$, grey lines for $D_{50\%}$ and dashed lines for $D_{5\%}$. [II]

In the second phase of the study, treatment plans for ten patients with varying-sized PTVs were prepared using the TPS algorithms. Applying the 3D-CRT technique separate plans with both the PBC algorithm and the AAA were made to meet the planning criteria. Both plan sets were recalculated with the AXB algorithm and comparisons with original plans were performed. The TPS algorithm comparison results showed large dose discrepancies in the PTV mean dose ($D_{50\%}$), nearly 60%, for the PBC algorithm and differences of nearly 20% for the AAA, occurring also in the small PTV size range, which is also shown in Figure 21. With DVH parameters for the OARs the deviations were 1.6% or less and 3.8% or less for the AAA and the PBC algorithm for all plans, respectively. [II]

At the other end of the density range, according to the first results in other studies, the AXB algorithm has been reported to reduce the uncertainties related to the dose calculation in the presence of high-Z materials closer to a clinically acceptable level. Therefore, in [III] the clinical benefit of the AXB algorithm was demonstrated in a phantom and with a clinical example for the treatment of a prostate cancer patient with a hip implant. In the first phase the AXB algorithm was benchmarked against point and film dosimetry in an anthropometric phantom ([171]) (Figure 22) with a unilateral hip implant and also against the MC model, which was concurrently validated against the measurements. The effect of the CT artefacts was quantified by performing the calculations with the original CT dataset and corrected CT dataset, where constant HU values were assigned, where applicable. [III]

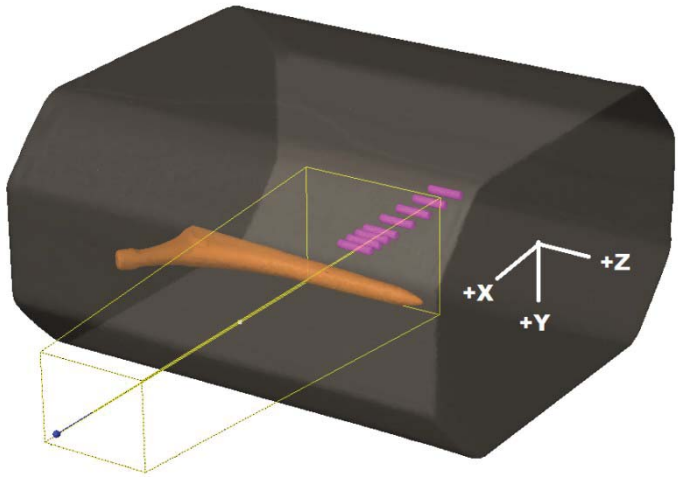

Figure 22. The phantom and a beam from the side, through the stem of the hip implant. Contoured cavities for the IC are also present. [III]

Scanditronix Wellhöfer FC65-G Farmer-type 0.6 cm^3 IC (Farmer IC) (IBA Dosimetry AB, Sweden) and IBA SFD were used as measurement detectors.

Figure 23 shows the results for the corrected CT dataset. For the Farmer IC, on average, the AXB algorithm underestimated the measured dose, with deviations in both CT datasets ranging from -1.1% to -2.2%, being smaller for the corrected CT dataset on average. With the MC model the overall discrepancies compared to measurements were smaller, the differences ranging from -0.9% to +0.7% in both CT datasets. [III]

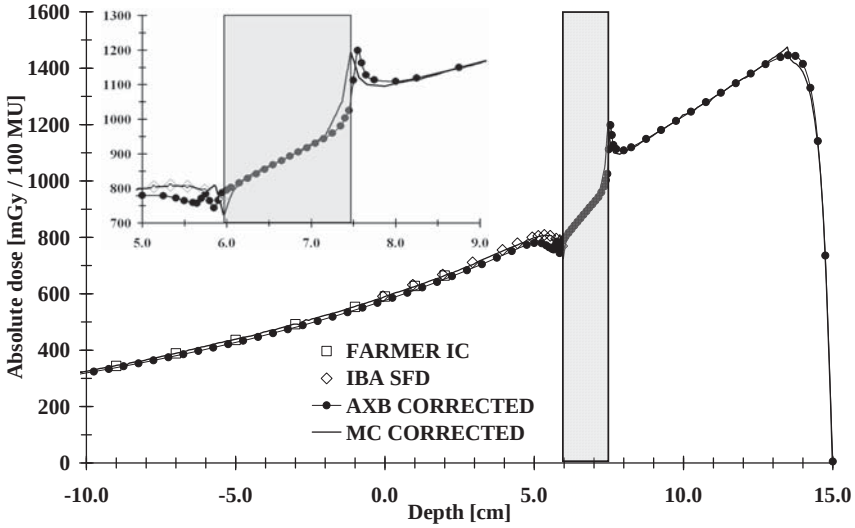

Figure 23. Measured (Farmer IC and IBA SFD) and calculated (the AXB algorithm and the MC model) depth dose values applying a 6 MV beam through the hip implant in the corrected CT dataset. The highlighted region represents the implant. The inset shows the magnification of the dose values in proximity to the implant and water interfaces. [III]

With the IBA SFD, the AXB algorithm underestimated the measured and the MC-calculated doses in the shadow of the implant. The deviations with both CT datasets ranged from -5.5% to +2.2% and the mean differences were -2.4% and -2.5% for the original and corrected CT datasets, respectively. When compared to measurements, the overall discrepancies with the MC model were smaller, the differences ranging from -3.1% to +0.1%. However, the AXB algorithm was congruent with the MC model upstream and inside the implant. In the proximal interface of the implant, the peak in the dose distribution was due to the increased backscatter from the high-Z material to the lower density material and it was modelled similarly by both the AXB algorithm and the MC model. [III]

The clinical benefit of the AXB algorithm was assessed in the second phase of the study. A clinical treatment plan was prepared for a prostate cancer patient with a unilateral hip implant using the VMAT technique with avoidance sectors

and static beams passing through the implant (referred to as the hybrid technique). The plan was recalculated with the MC model and the dose distribution was compared to the original AXB-calculated dose distribution to assess the accuracy of the AXB algorithm in a clinical setting with beams traversing the implant. A recalculation with the AAA was also performed to quantify the benefit of the improved dose calculation accuracy of the AXB algorithm over the AAA. [III]

The discrepancies between the AXB algorithm and the MC model were small. The 3D GAI result with an acceptance criteria 2%/2 mm between the AXB algorithm and the MC model was over 99%. In the DVH parameter comparison, in general, the AXB algorithm showed a small underestimation when compared to the MC model. The small discrepancies are visible in the isodose distributions shown in Figure 24. The DVH parameter results for the AAA showed small deviations from the results of the MC model, similar to the results of the AXB algorithm. However, in the vicinity of and inside the implant, the AAA produced greater deviations than the AXB algorithm when compared to the MC model. [III]

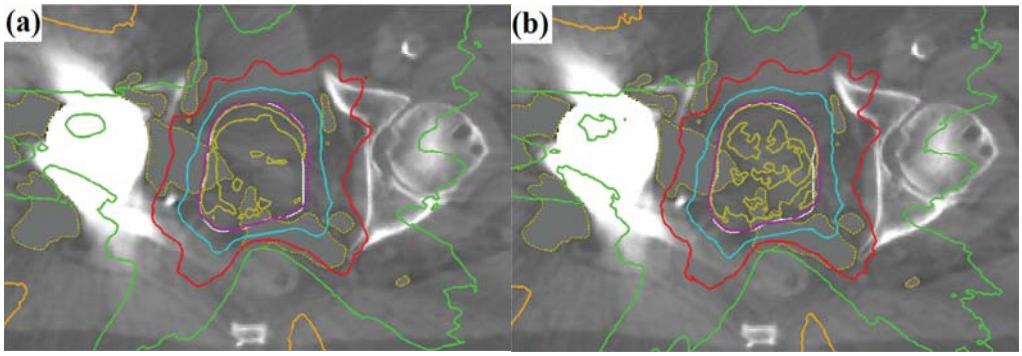

Figure 24. The isodose curves for clinical patient plan demonstration calculated both by the AXB algorithm **(a)** and the MC model **(b)**. Isodose levels from the outermost curve are 10%, 30%, 50%, 70%, 95% and 100% of the prescribed dose (PTV white). [III]

5.3. Electron beam dose calculation

Various intensity-modulated photon beam treatment techniques have replaced electron beams in many cases. Despite this, when treating the chest wall (post-mastectomy or intact chest) the application of electron beams is still considered a suitable option in terms of the resulting dose distribution. Great care should be taken when the electron beam is directed so that the beam CAX is parallel or close to parallel to the lung/mediastinum interface. This is because many of the commercial dose calculation algorithms are known to assume slab-like

geometry when calculating the dose in each voxel. Therefore, near the interface large dose uncertainties are expected. For this purpose, the calculation accuracy was tested for the Generalized Gaussian Pencil Beam (GGPB) algorithm (based on the pencil beam principle) and the electron MC (eMC) algorithm (based on the macro MC (MMC) principle), both implemented in the Varian Eclipse™ TPS. Preliminary and partial results are presented in [172]. The analytical GGPB algorithm is based on the Fermi-Eyges electron multiple scattering theory ([173-174]). The eMC algorithm, a Varian specific implementation of MMC in Eclipse™ TPS, utilises a large library of pre-calculated kernels using accurate MC simulations for spherical volumes of varying sizes, materials and energies. The kernels are then used in the MC simulation within the global CT-based patient geometry and the dose calculation is performed with an adaptive step-size algorithm ([175-176]). [IV]

First the MC models for 9 and 16 MeV electron beams were commissioned, as described in Sections 4.1-4.2. A comparison was made of the MC models against the measurements in water. Then the GGPB and eMC algorithms were benchmarked against the MC model in two virtual phantoms: 1) a water phantom, where a lung-equivalent slab covering the whole area of the phantom was immersed, and 2) a water phantom, where a lung-equivalent slab covering half of the phantom area was immersed (Figure 25). Finally, the beams with both energies were applied to an anthropomorphic phantom (RANDO) and in-phantom thermoluminescence dosimetry (TLD) was performed at selected points. The measurement results were compared to a CT-based dose distribution calculation by the MC model. The accuracy of the GGPB and the eMC algorithms was assessed by comparing it to the MC model simulation and the measurements. [IV]

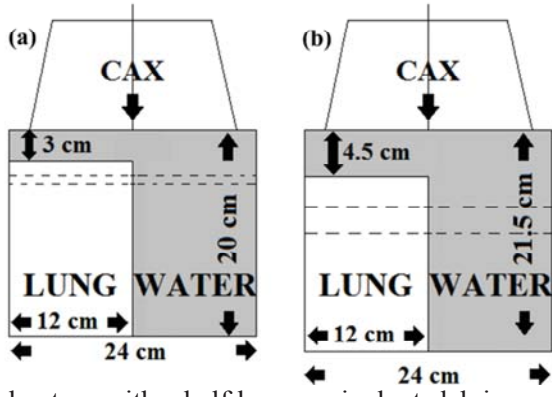

Figure 25. The phantom with a half lung-equivalent slab immersed in a water-equivalent phantom at a depth of 3 cm (9 MeV beam) **(a)** or 4.5 cm (16 MeV beam) **(b)**. The locations of planes selected for calculating profiles chosen for comparison are also shown. [IV]

For the both beam energies (Figures 26 and 27), the dose profiles calculated with the eMC algorithm show similar shapes to those calculated by the MC model. However, in the lung-equivalent material the dose values calculated by the eMC algorithm are 3-5% of D_{max} higher than the reference results of the MC model. In addition, in the dose profile at a shallower depth with the 9 MeV beam energy, the eMC algorithm results also overestimate the dose over the water-equivalent part by up to about 4% of D_{max}. In regions where the dose gradient is small, i.e. further away from the material boundary, the results of the GGPB calculation in the presence of heterogeneity correction lead to dose distributions closer to the MC model results, compared to results obtained from eMC calculations. Anyhow, in the vicinity of the material boundary, in the lung-equivalent region, the GGPB-calculated dose is 6-12% and 3-14% of D_{max} lower than in the MC-calculated dose profile for the 9 and 16 MeV beam energies, respectively, and over the water-equivalent region it is higher by about 12% and over 15% of D_{max} for the 9 and 16 MeV beam energies, respectively.

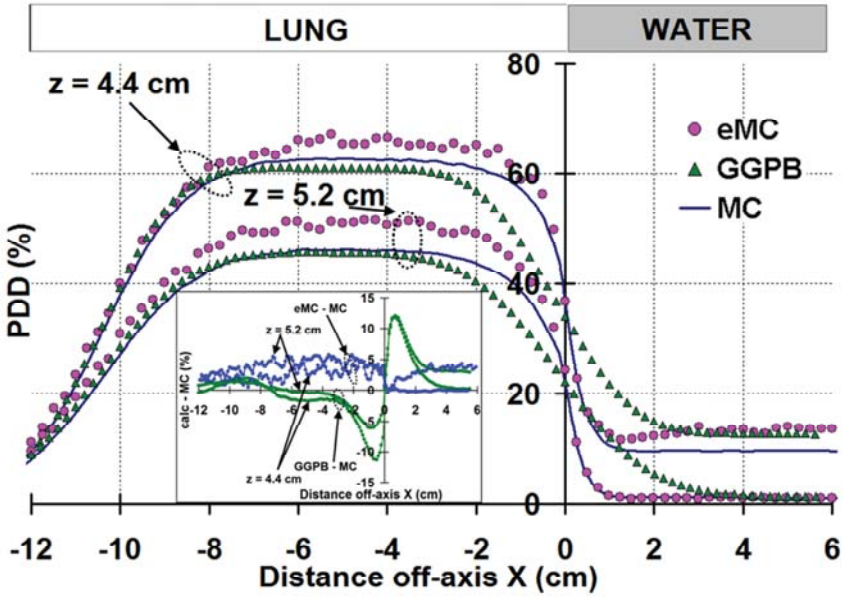

Figure 26. Dose profiles for the 9 MeV beam through the CAX in the phantom in Figure 25 at depths of 4.4 and 5.2 cm, calculated by the MC (blue, solid line), eMC (purple, circles) and GGPB (green, triangles) algorithms. [IV]

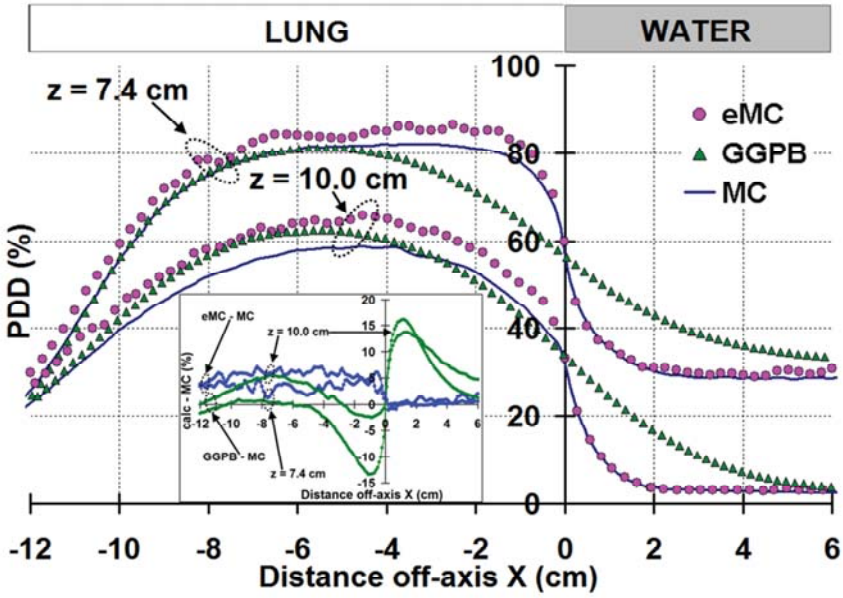

Figure 27. Dose profiles for the 16 MeV beam through the CAX in the phantom in Figure 25 at depths of 7.4 and 10.0 cm, calculated by MC (blue, solid line), eMC (purple, circles) and GGPB (green, triangles) algorithms. [IV]

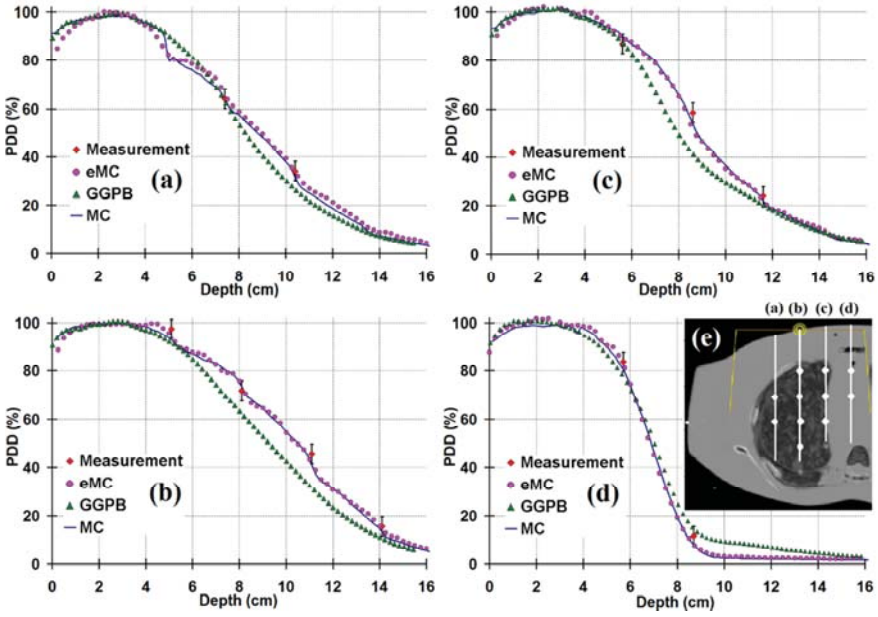

Figure 28 (a)-(e). PDD curves along white lines in (e) in RANDO anthropomorphic phantom. The PDD curves shown are for the MC model (blue, solid line), eMC (purple, circles) and GGPB (green, triangles) algorithms. The TLD point dose values (red, diamonds) with their error bars are the white dots shown in (e). [IV]

In the RANDO anthropomorphic phantom, the agreement for the eMC algorithm is better than for the GGPB algorithm when compared with the reference dose distribution calculated by the MC model and measured with TLD (Figure 28 (a)-(e)). In general, the eMC algorithm slightly overestimates the dose, by no more than 5% of D_{max} (the maximum overestimation at depth of 4.5 cm in Figure 28 (b)). The GGPB algorithm underestimates the dose in many regions, especially in the lung (by up to 15% of D_{max}), but performs better in the tissue-equivalent parts of the PDDs. In the DVH analysis for the lung in the RANDO phantom, with the prescription dose of 50 Gy being 100%, the V_{20Gy} values (volume fraction with absorbed dose higher than 20 Gy) were 23.3% and 28.2% for the GGPB and eMC algorithms, respectively.

6. DISCUSSION

6.1. The MC model for open and MLC-shaped beams and dosimetry applications

A prerequisite for the application of MC simulations as a reference method for various purposes is to develop a treatment head geometry and beam model, with which the disagreement against the reference linac measurement data would be as small as possible. In this work the manufacturer's data on the construction details of the reference linac were interpreted with great care (taking into account the reported tolerances), readily accessible components were measured and inconsistent information was sorted out by contacting the manufacturer. For those parameters on which no information was available and no measurements were possible, the initial values were gathered from other studies and the final values resulted from an iterative fine-tuning process.

Special attention was paid to the acquisition of accurate reference measurement data. First the measurements and the MC model fine-tuning was performed for the reference field sizes used in QA activities at Tays and then for small and large fields. The deviations from the measurements with PDDs were within 0.5% and 1.0% of D_{max} at depths greater than 1.0 cm for the 6 MV and 18 MV photon beams, respectively, being mostly between 0.0% and 0.5%. The largest discrepancies in PDDs were for the small field with the 18 MV photon beam. In general, the deviations in PDDs were small compared to other studies. Often, an acceptable congruence has been considered to be found if the discrepancies are less than 1-2% ([12,41,72-73,76-77]). The largest deviations in the dose build-up region, near the phantom surface, suggest that the MC model most likely produces a better estimate of the surface dose, since there are more uncertainties related to the measured build-up doses. This is supported by other studies where better congruence has been reported, when special attention has been paid to the reference measurement equipment selection and set-up ([42-43,81]). With the Gafchromic EBT film measurements, the combined uncertainty originated from the determination of the actual measurement depth of the film active volume, the non-water equivalence of the Gammex solid water, and the issues related to film calibration. With the PTW Semiflex IC, the active volume averaging effect of the detector caused uncertainties in the steep dose gradient region present in

the dose build-up region, similar to the dose profile penumbrae. The congruence in the dose build-up region was better for the 6 MV photon beam small field, for which the PDD was measured with the IBA SFD, because of the negligible volume of the detector active volume. With electron beams the deviations in PDDs were smaller with increasing nominal beam energy, generally being less than 1.0% of D_{max}, which is similar to or less than that found in other studies ([105-107]). This suggests that the smaller the nominal energy, the more sensitive the MC model is to simulation parameter selection. On the other hand, with lower nominal beam energies the issues related to the accuracy of the measurement detector positioning, the EPOM selection and the effect of the detector active volume size are more pronounced.

In the dose profiles the congruence was good, mostly within 0.5% of D_{max} in high dose regions and out-of-field regions. The DTA values in penumbrae were less than 0.5 mm for small fields with photon beams and with all electron beam dose profiles, and less than 1.0 mm for large photon beam field sizes, due to the volume averaging effect of the PTW Semiflex IC. Again, these deviations are smaller than those accepted or achieved in other studies, in which the reported discrepancies were often 1-3% in high dose regions and 1-2 mm DTA in penumbrae ([41,72,77,105-107]). With output factors, including the contribution of the backscatter to the monitor chamber through the absolute dose calibration described in Section 4.3., the deviations were mostly about or less than 0.5%. These discrepancies are small when compared to the results obtained in other studies ([41,72,79,105,108]). All in all, the performance of the MC model in this study in a water phantom, where the reference measurement data of relatively good accuracy is achievable, has been shown to be as good or better than that reported in other studies. The merit of the MC models is that both the photon beam and the electron beam geometry models are based on identical common components of the treatment head ([I]), which in combination with the benchmarking results indicate that the MC models represent the realistic linac used as reference.

The MC model built for open beams, i.e. for beams collimated only with the jaws, is insufficient for TPS QA purposes in modern radiotherapy. Therefore, the MLC model in the MC model was separately commissioned and bench-marked. The complexity of the MLC and the related geometry model introduced the need to include several various field configurations for testing. At the same time, the requirements for the reference measurement data acquisition became more demanding, since the test fields contained very small apertures and sharp dose gradients, both in 1D and 2D and in static and dynamic mode. The performance of the MC model was assessed by comparing the calculated dose profiles to those measured dose profiles that were

considered to represent the most accurate measurement data in each test field and separate test field region. The pros and cons of each detector were taken into account, such as the very high spatial resolution but the oversensitivity to scattered radiation of the IBA SFD. The MC model showed congruent results with the measurements, similar to other studies ([88-89,94,158]) and on the other hand, thus served as a reference for measurements. The performance of the MC model with dynamic MLC fields was assessed, simulating a complex 'sliding window' dynamic MLC field and comparing the calculation results to measured dose distributions by an IC array detector and film dosimetry system ([161]). The comparison to the IC array detector showed congruent results, but due to the coarse spatial resolution of the measurement, the comparison with the film dosimetry system was essential. The deviations from the film dosimetry system were small, and simultaneously the MC model provided reference data for benchmarking the film dosimetry system. As shown in other studies ([92,96-99]), rigorous commissioning of the MC MLC model is a necessity for obtaining dose distributions with the MC model that can be further used for more advanced purposes. However, an issue that needs to be taken into account is that in measurements which include large dose gradients or areas of charged particle disequilibrium, the measurement uncertainty is increased and even if the MC model were to produce congruent results, the measurement uncertainty contributes to the resulting total uncertainty of the MC-calculated dose distribution. In charged particle disequilibrium conditions, even a perfect agreement between MC simulation and a single dosimetric method does not imply that the result is definitely the best. The performance needs to be assessed against general properties of the dosimetric methods (i.e. detector size/resolution, water equivalence and sensitivity to spectral changes) in specific measurement conditions.

The commissioning of the MC-based treatment head geometry and beam model contains a large number of parameters. Despite this, the manufacturers provide detailed geometric and material information for many of the components, there is still a notable number of complete components and parameters that have to be determined by the user by measuring or otherwise iteratively tuning. In addition, the above-mentioned data provided by the manufacturer often contains tolerances that increase the number of iterations needed in the commissioning process. All these uncertainties result in the fact that the final configuration of the MC model is always a unique solution for a single reference linac and the output that has been used for reference measurement data acquisition. This also means that there is no single correct configuration, i.e. when slightly changing some parameter values, the effects may cancel each other out and the combined result is a dose distribution that is similar to the original results within the statistical uncertainty. This also introduces a pitfall, because the variation of

some parameters may not affect the calculated dose distributions in a similar way to the variation of some other parameter. This can be overcome by performing comprehensive and rigorous benchmarking for the MC model, naturally focusing on acquiring reference measurement data of the highest possible accuracy at first. The related uncertainties in the MC model could also be reduced if the manufacturers were to provide even more detailed information on the initial electron beam and treatment head components, especially those contributing to the extra-focal component of the radiation beam emerging from the treatment head. This would perhaps further improve the build-up dose modelling, as suggested in [41]. Moreover, the CMs in the BEAMnrc code system are not fully sufficient for modelling all the necessary components and especially their movement in the treatment head. Examples of such are the tilted mirror with its frame and surrounding shielding structure and the jaws, of which one pair of blocks moves in an arc and the other one pivots around a certain point.

6.2. The application of the MC model to specific clinical cases in radiotherapy

When TPS QA or patient plan verification is pursued, a major advantage of MC models is that they inherently produce 3D dose distributions of the desired resolution in a virtual or CT-based 3D calculation phantom of choice. This is contrary to measurement-based methods, where the dose distributions are often projected to 2D. Even if the measurement device were to produce 3D measurement data, the dose distribution for comparison purposes is generally recalculated in measurement phantoms that are different from the original ones, and the perturbations introduced by the measurement detectors are also to be taken into account.

To explore and exploit the benefits of the MC methods in TPS QA purposes, the MC model commissioned in this study was used to assess the accuracy of a commercial TPS in several clinical cases ([II][III][IV]). The performance of the TPS dose calculation algorithms in tissues with lower density than the density of the water has always been of interest, especially after the introduction of SBRT to the treatment of malignancies of the lung. The main aim in [II] was to assess the accuracy of a new ‘type c’ photon beam dose calculation algorithm in comparison to two other, ‘type a’ and ‘type b’, TPS algorithms in the SBRT of the lung. However, first the ‘type c’ algorithm was benchmarked against the MC model. The results in [II] suggest that, as already shown in other studies, the PBC algorithm (‘type a’) should not be applied in dose calculation for the SBRT of the lung, since it overestimates the dose in the PTV, especially for

plans with small PTVs. The deviations between the AXB algorithm ('type c') and the AAA ('type b') were small for the plans with large PTVs, but discrepancies were found with the plans with small PTVs. Interestingly, for certain plans the results suggested that the AAA produced dose distributions closer to the ones calculated with the MC model than the AXB algorithm. In other studies ([169,177-178]), the AXB algorithm has been shown to provide equally or even more accurate dose distributions than the AAA in virtual slab phantoms and in both anthropomorphic and patient phantom geometries, which was not fully supported by the results of [II] for patient phantom geometries. The AXB algorithm version utilised in [II] requires more comprehensive benchmarking prior to clinical commissioning, especially for the SBRT of the lung, and the comparisons in [II] need to be reassessed in order to quantify the effect of the reported improvements of the algorithm included in the next version ([179]). Therefore, in [II] it was suggested that independent plan verification, such as full MC dose calculation and/or measurements, should be applied, when the AAA or the AXB algorithm are utilised in the SBRT of the lung having PTVs smaller than 20-25 cc. However, the calculated data in [II] can be used, in addition to similar contributions from other studies by the radiotherapy community, in adjusting the SBRT protocols based on 'type a' and/or 'type b' algorithms for the most recent generation, 'type c' algorithms, such as the AXB algorithm.

The challenges in the TPS dose calculation in the presence of high-Z materials, for example, in the form of a hip implant, have influenced the whole of treatment planning in general. This is because usually such treatment beam directions have been avoided where the beams first traverse the implant prior to impinging on the volume to be treated. This has resulted in less optimal dose distributions with respect to the PTV and OARs when compared to patients with no hip implants. However, the previously reported improved dose calculation accuracy of the AXB algorithm in the presence of high-Z materials has been suggested for overcoming this issue and therefore in [III] it was benchmarked against the MC model, also providing a comparison to the AAA. The clinical benefit of the algorithm was demonstrated with a prostate cancer patient with a unilateral hip implant, for whom a treatment plan using hybrid VMAT technique was drawn up. According to the findings in [III], the AXB algorithm was shown to agree well with the MC model and the measurements, as already seen in [11] and [180]. With the clinical example plan, the discrepancies between the MC model and the AXB algorithm were small, with the MC model producing slightly higher doses than the AXB algorithm. This was quantitatively confirmed by the GAI value and through comparison with corresponding DVH parameter results. This means that in addition to phantom calculations, the AXB algorithm is a reliable choice for clinical dose calculation

with patient plans including hip implants, where the beams traverse high-Z material. The AAA showed relatively good congruence with the MC model and the AXB algorithm in the PTV and OARs, but due to the discrepancies in the vicinity of and inside the implant, the use of the AAA is discouraged in clinical situations similar to those presented in [III]. In addition, [III] was also the first study where the accuracy of the AXB algorithm applying the VMAT technique was assessed by comparing to full MC simulations.

With the electron beams the clinical dose calculation has also suffered from large uncertainties in the presence of materials, the density of which has considerably differed from the density of water. In [IV] a special case, when an electron beam is directed towards the chest wall so that the beam CAX is parallel or close to parallel to the lung/mediastinum interface, was studied. The accuracy of two TPS dose calculation algorithms was benchmarked in various slab and anthropomorphic phantom geometries against measurements and the MC model. The results of [IV] suggested that the MC-based eMC algorithm provides improved dose distributions when compared to the pencil beam-based GGPB algorithm, which significantly underestimates the lung dose and overestimates the dose to the mediastinum in the studied case. In general, the results in [IV] are consistent with the findings in other studies ([123,181-182]). However, there were discrepancies between the eMC algorithm and the MC model in the virtual phantom calculations. It suggests that the performance of the eMC algorithm should be further assessed, especially with the more recent versions of the algorithm, and that an independent plan verification should be applied, for example, with full MC simulations and/or measurements, when the eMC algorithm is used with studied patient geometry.

The built and benchmarked MC model for photon and electron beams in this study has been shown to provide reference-level dose distributions in both virtual and CT-based phantoms for dosimetry and TPS benchmarking purposes. The reported deviations in a water phantom between the MC model and the measurements were small in both photon and electron beams in general, when compared to other studies, where usually only photon or electron beams and a smaller set of beam energies are covered. In addition, the consistency between the MLC-shaped test field measurements and the MC model simulation results was good, taking into account the issues related to the measurement accuracy. All the simulations were performed with a large number of particle histories, which minimised the effect of statistical uncertainties on the results. In addition, the use of variance reduction techniques was kept to the minimum, so that they would introduce minimal bias to the results. These in turn minimised the effect of the systematic uncertainties, i.e. the latent variance ([183]), introduced through the utilisation of intermediate phase space files, to the calculated dose

distributions. The effect was further decreased by using the shared library feature in the BEAMnrc system, where applicable. All in all, the achieved accuracy of the MC model to simulate beams from the treatment head was considered to be adequate for further purposes, where dose distributions need to be simulated in various phantom geometries.

In addition to default materials included in the PEGS4 cross-section data library, additional data was produced to take into account all the known material compositions and densities present in the treatment head and phantom simulations. This allowed a more meaningful comparison between the MC model, the measurements and the TPS calculations. In CT-based calculations, the correspondence between the HU values and densities is taken into account through a conversion curve and the material assignment is performed utilising the curve. In this study the conversion curve was determined with great care and identical curves were used in the MC model calculations and in the TPS. This is an important issue in enabling the assessment of actual dose calculation accuracy between the calculation methods. Furthermore, since the MC model inherently calculates the $D_{m,m}$ whereas most of the clinical TPS dose calculation algorithms calculate the $D_{w,m}$, the systematic differences introduced due to dose reporting mode have to be taken into consideration in comparisons. The differences are small, 1-2%, for tissues with densities close to water, but for the bone, for example, the discrepancy may reach 15% ([2]). The issue can be overcome by converting the dose distributions between the dose reporting modes as post-processing step without introducing noteworthy approximations to the results ([184]).

Since the statistical fluctuations are inherent characteristics of MC-based dose distributions, the point dose-based approach in dose comparison may result in erroneous conclusions. Instead, integrated dose quantities, such as DVH comparison, are recommended. However, if point dose values are used, a low level of statistical uncertainty should be pursued. [2] One option is also to perform denoising for dose distributions utilising a method that would represent an optimal trade-off between smoothing the fluctuations due to statistical noise and real variation in dose levels. [185-186] Another argument for applying denoising is to reduce the number of histories that need to be simulated in order to attain the desired level of statistical uncertainty, which in turn decreases the calculation time ([186]). Long calculation times, which have traditionally been the major drawback related to MC methods, were not given special attention in this study, that is, the number of particle histories and other simulation parameters were chosen so that the calculation accuracy was optimised.

The MC model in this study has been proved to function as a dose calculation tool for QA purposes. Virtual phantoms of any material and rectilinear shape can be built to represent idealised calculation geometries, whereas CT-based calculation phantoms can be used to mimic the clinical treatment planning process with the related issues. The MC model can be applied as reference for various dosimetric devices measuring the delivered dose distributions, or the MC model may fully replace the measurements in TPS QA and treatment plan verification. In addition, another interesting application for the MC model is the linac QA, where the beam delivery and movements are simulated based on log files ([139]). In the future, it is expected that clinical dose calculations will be based on full MC simulations. However, one challenge with this is the application of the MC techniques in solving inverse problems applied in plan optimisation. One possible solution is to combine the deterministic calculation techniques that are powerful in inverse problem calculations with the accuracy of the MC techniques that can be used in the intermediate and final dose distribution calculations. As the dose distributions based on full MC simulations are considered to represent the 'reality', they can also be used for retrospective dose calculations, for patients for which the treatment outcome, local tumour control and normal tissue complications are known. This information may further be used for adjusting the treatment protocols and thus pursuing more favourable clinical outcomes.

7. CONCLUSIONS

The invincible dose calculation accuracy of full MC simulations cannot be exploited prior to thorough commissioning of the MC model that includes detailed configuration and benchmarking. Despite this, some of the most popular codes, such as the BEAMnrc system, are user-friendly with their GUIs, but the user has to have knowledge of the parameters with which the underlying physics transport, geometry model and other simulation options are governed. The rigorous benchmarking process requires a wide collection of accurate reference measurement data, including all the beam energies, various field sizes, phantom geometries and measurement detectors/methods, against which the MC model is iteratively fine-tuned. However, previously published results on the BEAMnrc system, which has been effectively tested among the radiotherapy community, give good information on the assets and pitfalls related to the simulations.

The good accuracy level of the model that was achieved was confirmed through comparisons against measurements in water in different circumstances, both with square fields and more complex MLC-shaped static and dynamic fields. The results of output factor comparison attested to the validity of the absolute dose calibration of the MC model that is essential, especially in TPS benchmarking.

The MC model was applied to accuracy testing of the TPS in certain clinical cases. The results of this study have shown that even the most advanced TPS algorithms are not always able to reach clinically acceptable accuracy levels, when large heterogeneity differences are present. This, especially in combination with new treatment techniques, establishes the demand for further verification techniques, such as full MC simulations. With photon beams, in the SBRT of the lung – apart from small differences in general – the most recent generation TPS dose calculation algorithm was shown to disagree with results of the MC model in certain cases, whereas the algorithm from the previous generation provided more congruent results with the MC model. The differences suggest that independent plan verification is needed in the SBRT of the lung with plans having small PTVs. With high-Z materials the most recent generation TPS dose calculation algorithm provided clinically acceptable

results against the MC model both in phantom, when verified against measurements, and with a patient plan, when the beam traverses the implant, whereas the use of a TPS dose calculation algorithm from the previous generation is discouraged. However, with other high-Z materials than that used in our study, the most recent generation TPS dose calculation algorithm has to be benchmarked separately, also taking the artefacts in the CT datasets into account. With electron beam TPS dose calculation algorithms, the MC model was used to assess the accuracy of two TPS algorithms at a tissue heterogeneity interface parallel to the beam CAX. The most recent generation algorithm provided more congruent results with the MC model than the other algorithm, which was also verified by the anthropomorphic phantom measurements. Despite this, such differences were discovered in flat dose regions that further improvements are anticipated in future versions of the most recent generation algorithm. In conclusion, there is a definite need for the MC model to provide reference dose distributions for the commissioning of new dosimetric methods, and for patient plans in which the current clinical TPS algorithms are known to generate large dosimetric uncertainties. In addition, the MC model is exploited to benchmark new dose calculation algorithms to be commissioned.

The utilisation of the MC model described in this study, in addition to the TPS configuration data validation performed, represents the type of use that most directly benefits the clinical radiotherapy community and has the most straightforward effect on the total uncertainty involved in radiotherapy. However, the real strength of the MC methods lies in the fact that they can be adapted to meet any applications where dose distributions of reference-level accuracy are needed. Also, it is only a matter of time when all the radiotherapy treatment planning dose calculations are performed applying full MC simulations.

REFERENCES

[1] Van Dyk, J. The Modern Technology Of Radiation Oncology: A Compendium for Medical Physicists and Radiation Oncologists. Madison 1999, Medical Physics Publishing. 1072 p.

[2] Chetty, I.J., Curran, B., Cygler, J.E., DeMarco, J.J., Ezzell, G., Faddegon, B.A., Kawrakow, I., Keall, P.J., Liu, H., Ma, C.-M., Rogers, D.W.O., Seuntjens, J., Sheikh-Bagheri, D., Siebers, J.V. Report of the AAPM Task Group 105: Issues associated with clinical implementation of Monte Carlo-based photon and electron external beam treatment planning. Med Phys, 34(2007)12, pp. 4818-53.

[3] Reynaert, N., van der Marck, S.C., Schaart, D.R., Van der Zee, W., Van Vliet-Vroegindeweij, C., Tomsej, M., Jansen, J., Heijmen, B., Coghe, M., De Wagter, C. Monte Carlo treatment planning for photon and electron beams. Radiat Phys Chem, 76(2007)4, pp. 643-86.

[4] Dutreix, A. When and how can we improve precision in radiotherapy? Radiother Oncol, 2(1984)4, pp. 275-92.

[5] Orton, C.G., Mondalek, P.M., Spicka, J.T., Herron, D.S., Andres, L.I. Lung corrections in photon beam treatment planning: are we ready? Int J Radiat Oncol Biol Phys, 10(1984)12, pp. 2191-9.

[6] Stewart, J.G., Jackson, A.W. The steepness of the dose response curve both for tumor cure and normal tissue injury. Laryngoscope, 85(1975)7, pp. 1107-11.

[7] Goitein, M., Busse, J. Immobilization error: some theoretical considerations. Radiology, 117(1975)2, pp. 407-12.

[8] Papanikolaou, N., Battista, J., Boyer, A., Kappas, C., Klein, E., Mackie, T., Sharpe, M., Van Dyk, J. Report of the AAPM Task Group 63: AAPM Report No. 85 - Tissue inhomogeneity corrections for megavoltage photon beams. Madison, WI, 2004, Medical Physics. 135 p.

[9] Low, D.A., Moran, J.M., Dempsey, J.F., Dong, L., Oldham, M. Dosimetry tools and techniques for IMRT. Med Phys, 38(2001)3, pp. 1313-38.

[10] Khan, F.M. The Physics of Radiation Therapy. 4th edition. Philadelphia 2009, Lippincott Williams & Wilkins. 592 p.

[11] Failla, G.A., Wareing, T., Archambault, Y., Thompson, S. Acuros® XB advanced dose calculation for the Eclipse™ treatment planning system. Varian Medical Systems Inc., Palo Alto, CA, USA, 2010. 32 p.

[12] Verhaegen, F., Seuntjens, J. Monte Carlo modelling of external radiotherapy photon beams. Phys Med Biol, 48(2003)21, pp. 3401-58.

[13] Raeside, D.E. Monte Carlo Principles and Applications. Phys Med Biol, 21(1976)2, pp. 181-97.

[14] Andreo, P. Monte Carlo techniques in medical radiation physics. Phys Med Biol, 36(1991)7, pp. 861-920.

[15] Ma, C.-M., Jiang, S.B. Monte Carlo modelling of electron beams from medical accelerators. Phys Med Biol, 44(1999)12, pp. R157-89.

[16] Rogers, D.W.O. Fifty years of Monte Carlo simulations for medical physics. Phys Med Biol, 51(2006)13, pp. R287-R301.

[17] Podgorsak, E.B. Radiation Physics for Medical Physicists. 2nd edition. Heidelberg/Berlin 2010. Springer-Verlag. 700 p.
[18] Rogers, D.W.O., Faddegon, B.A., Ding, G.X., Ma, C-M., We, J., Mackie, T.R. BEAM: A Monte Carlo code to simulate radiotherapy treatment units. Med Phys, 22(1995)5, pp. 503-24.
[19] Kawrakow, I., Mainegra-Hing, E., Rogers, D.W.O., Tessier, F., Walters, B.R.B. The EGSnrc Code System: Monte Carlo Simulation of Electron and Photon Transport. NRCC Report PIRS-0701. 2013. 312 p.
[20] Rogers, D.W.O., Walters, B., Kawrakow, I. BEAMnrc User's Manual. NRCC Report PIRS-0509(A)revL. 2013. 288 p.
[21] Walters, B., Kawrakow, I., Rogers, D.W.O. DOSXYZnrc User's Manual. NRCC Report PIRS-0794revB. 2013. 125 p.
[22] Storm, E., Israel, H.I. Photon Cross Sections from 1 keV to 100 MeV for Elements Z=1 to Z=100. Nucl Data Tables, A7(1970)6, pp. 565-681.
[23] Hubbell, J.H., Øverbø, I. Relativistic Atomic Form Factors and Photon Coherent Scattering Cross Sections. J Phys Chem Ref Data, 8(1979)1, pp. 69-105.
[24] Sauter, F. Über den atomaren Photoeffekt in der K-Schale nach der relativistischen Wellenmechanik Diracs. Ann Phys, 403(1931)4, pp. 454-88.
[25] Motz, J.W., Olsen, H.A., Koch, H.W. Pair production by photons. Rev Mod Phys, 41(1969), pp. 581-639.
[26] Øverbø, I., Mork, K.J., Olsen, A. Pair production by photons: Exact calculations for unscreened atomic field. Phys Rev A, 8(1973)2, pp. 668-84.
[27] Votruba, V. Pair production by gamma-rays in the field of an electron. Bull Intern Acad Tcheque Sci, 49(1948), pp. 19-49.
[28] Mork, K.J. Pair production by photons on electrons. Phys Rev, 160(1967)5, pp. 1065-71.
[29] Berger, M.J. Monte Carlo Calculation of the penetration and diffusion of fast charged particles. Meth Comput Phys, 1(1963), pp. 135-215.
[30] Møller, C. Zur Theorie des Durchgangs schneller Elektronen durch Materie. Ann Phys, 406(1932)5, pp. 531-85.
[31] Bhabha, H.J., Proc Royal Society London, A154(1935), p. 195.
[32] Mott, N.F., Proc. Royal Society London A124(1929), p. 425.
[33] Lobo, J., Popescu, I.A. Two new DOSXYZnrc sources for 4D Monte Carlo simulations of continuously variable beam configurations, with applications to RapidArc, VMAT, TomoTherapy and CyberKnife. Phys Med Biol, 50(2010), pp. 4431-43.
[34] Kawrakow, I. On the efficiency of photon beam treatment head simulations. Med Phys, 32(2005)7, pp. 2320-2326.
[35] Kawrakow, I., Rogers, D.W.O., Walters, B.R.B. Large efficiency improvements in BEAMnrc using directional bremsstrahlung splitting. Med Phys, 31(2004)10, pp. 2883-898.
[36] Ali, E.S., Rogers, D.W.O. Efficiency improvements of x-ray simulations in EGSnrc user-codes using bremsstrahlung cross-section enhancement (BCSE). Med Phys, 34(2007)6, pp. 2143-54.
[37] Andreo, P., Burns, D.T., Hohlfeld, K., Huq, M.S., Kanai, T., Laitano, F., Smyth, V.G., Vynckier, S. IAEA International Atomic Energy Agency. Absorbed Dose

Determination in External Beam Radiotherapy: An International Code of Practice for Dosimetry Based on Standards of Absorbed Dose to Water. Technical Reports Series no. 398. Vienna 2004. 181 p.
[38] Almond, P.R., Biggs, P.J., Coursey, B.M., Hanson, W.F., Huq, M.S., Nath, R., Rogers, D.W.O. AAPM's TG-51 protocol for clinical reference dosimetry of high-energy photon and electron beams. Med Phys, 26(1999)9, pp. 1847-70.
[39] Aljarrah, K., Sharp, G.C., Neicu, T., Jiang, S.B. Determination of the initial beam parameters in Monte Carlo linac simulation. Med Phys, 33(2006)4, pp. 850-858.
[40] Sheikh-Bagheri, D., Rogers, D.W.O. Sensitivity of megavoltage photon beam Monte Carlo simulations to electron beam and other parameters. Med Phys, 29(2002)3, pp. 379-90.
[41] Chibani, O., Moftah, B., Ma, C.-M. On Monte Carlo modeling of megavoltage photon beams: a revisited study on the sensitivity of beam parameters. Med Phys, 38(2011)1, pp. 188-201.
[42] Parsai, E.I., Shvydka, D., Pearson, D., Gopalakrishnan, M., Feldmeier, J.J. Surface and build-up region dose analysis for clinical radiotherapy photon beams. Appl Radiat Isotopes, 66(2008)10, pp. 1438-42.
[43] Apipunyasopon, L., Srisatit, S., Phaisangittisakul, N. An investigation of the depth dose in the build-up region, and surface dose for a 6-MV therapeutic photon beam: Monte Carlo simulation and measurements. J Radiat Res, 54(2013)2, pp. 374-82.
[44] Devic, S., Seuntjens, J., Abdel-Rahman, W., Evans, M., Olivares, M., Podgorsak, E.B., Vuong, T., Soares, C.G. Accurate skin dose measurements using radiochromic film in clinical applications. Med Phys, 33(2006)4, pp. 1116-24.
[45] Ding, G.X. Dose discrepancies between Monte Carlo calculations and measurements in the buildup region for a high-energy photon beam. Med Phys, 29(2002)11, pp. 2459-63.
[46] Ding, G.X. Energy spectra, angular spread, fluence profiles and dose distributions of 6 and 18 MV photon beams: results of Monte Carlo simulations for a Varian 2100EX accelerator. Phys Med Biol, 47(2002)7, pp. 1025-46.
[47] Liu, H.H., Mackie, T.R., McCullough, E.C. A dual source photon beam model used in convolution/superposition dose calculations for clinical megavoltage x-ray beams. Med Phys, 24(1997)12, pp. 1960-74.
[48] Hartmann Siantar, C.L., Walling, R.S., Daly, T.P., Faddegon, B., Albright, N., Bergstrom, P., Bielajew, A.F., Chuang, C., Garrett, D., House, R.K., Knapp, D., Wieczorek, D.J,, Verhey, L.J. Description and dosimetric verification of the PEREGRINE Monte Carlo dose calculation system for photon beams incident on a water phantom. Med Phys, 28(2001)7, pp. 1322-37.
[49] Das, I., Ding, G.X., Ahnesjö, A. Small fields: Nonequilibrium radiation dosimetry. Med Phys, 35(2008)1, pp. 206-15.
[50] Ding, G.X., Duggan, D.M., Coffey, C.W. A theoretical approach for non-equilibrium radiation dosimetry. Phys Med Biol, 53(2008)13, pp. 3493-9.
[51] Laub, W.U., Wong, T. The volume effect of detectors in the dosimetry of small fields used in IMRT. Med Phys, 30(2003)3, pp. 341-7.

[52] Scott, A.J., Kumar, S., Nahum, A.E., Fenwick, J.D. Characterizing the influence of detector density on dosimeter response in non-equilibrium small photon fields. Phys Med Biol, 57(2012)14, pp. 4461-76.
[53] Underwood, T.S.A., Winter, H.C., Hill, M.A., Fenwick, J.D. Mass-density compensation can improve the performance of a range of different detectors under non-equilibrium conditions. Phys Med Biol, 58(2013)23, pp. 8295-310.
[54] Pappas, E., Maris, T.G,. Papadakis, A., Zacharopoulou, F., Damilakis, J., Papanikolaou, N., Gourtsoyiannis, N. Experimental determination of the effect of detector size on profile measurements in narrow photon beams. Med Phys, 33(2006)10, pp. 3700-10.
[55] Westermark, M., Arndt, J., Nilsson, B., Brahme, A. Comparative dosimetry in narrow high-energy photon beams. Phys Med Biol, 45(2000)3, pp. 685-702.
[56] Sauer, O.A., Wilbert, J. Measurement of output factors for small photon beams. Med Phys, 34(2007)6, pp. 1983-88.
[57] Alfonso, R., Andreo, P., Capote, R., Huq, M.S., Kilby, W., Kjäll, P., Mackie, T.R., Palmans, H., Rosser, K., Seuntjens, J., Ullrich, W., Vatnitsky, S. A new formalism for reference dosimetry of small and non-standard fields. Med Phys, 35(2008)11, pp. 5179-86.
[58] Cranmer-Sargison, G., Weston, S., Evans, J.A., Sidhu, N.P., Thwaites, D.I. Implementing a newly proposed Monte Carlo based small field dosimetry formalism for a comprehensive set of diode detectors. Med Phys, 38(2011)12, pp. 6592-602.
[59] Czarnecki, D., Zink, K. Monte Carlo calculated correction factors for diodes and ion chambers in small photon fields. Phys Med Biol, 58(2013)8, pp. 2431-44.
[60] Aspradakis, M.M., Byrne, J.P., Palmans, H., Conway, J., Rosser, K., Warrington, J.A.P., et al. IPEM Report Number 103 - Small Field MV Photon Dosimetry. York 2010, IPEM. 196 p.
[61] Griessbach, I., Lapp, M., Bohsung, J., Gademann, G., Harder, D. Dosimetric characteristics of a new unshielded silicon diode and its application in clinical photon and electron beams. Med Phys, 32(2005)12, pp. 3750-4.
[62] Wang, L.L., Rogers, D.W.O. Monte Carlo study of si diode response in electron beams. Med Phys, 34(2007)5, pp. 1734-42.
[63] Di Venanzio, C., Marinelli, M., Milani, E., Prestopino, G., Verona, C., Verona-Rinati, G., Falco, M.D., Bagalà, P., Santoni, R., Pimpinella, M. Characterization of a synthetic single crystal diamond Schottky diode for radiotherapy electron beam dosimetry. Med Phys, 40(2013)2, p. 021712.
[64] Dieterich, S., Sherouse, G.W. Experimental comparison of seven commercial dosimetry diodes for measurement of stereotactic radiosurgery cone factors. Med Phys, 38(2012)7, pp. 4166-73.
[65] Chaney, E.L., Cullip, T.J., Gabriel, T.A. A Monte Carlo study of accelerator head scatter. Med Phys, 21(1994)9, pp. 1383-90.
[66] Ding, G.X. An investigation of accelerator head scatter and output factor in air. Med Phys, 31(2004)9, pp. 2527-33.
[67] Mohan, R., Chui, C., Lidofsky, L. Energy and angular distributions of photons from medical linear accelerators. Med Phys, 12(1985)5, pp. 592-7.

[68] Sheikh-Bagheri, D., Rogers, D.W.O. Monte Carlo calculation of nine megavoltage photon beam spectra using the BEAM code. Med Phys, 29(2002)3, pp. 391- 402.
[69] Kosunen, A., Rogers, D.W.O. Beam quality specification for photon beam dosimetry. Med Phys, 20(1993)4, pp. 1181-8.
[70] Lee, P.C. Monte Carlo simulations of the differential beam hardening effect of a flattening filter on a therapeutic x-ray beam. Med Phys, 24(1997)9, pp. 1485-89.
[71] Lovelock, D.M., Chui, C.S., Mohan, R. A Monte Carlo model of photon beams used in radiation therapy. Med Phys, 22(1995)9, pp. 1387-94.
[72] van der Zee, W., Welleweerd J. Calculating photon beam characteristics with Monte Carlo techniques. Med Phys, 26(1999)9, pp.1883-92.
[73] Lin, S.-Y., Chu, T.-C., Lin J.-P. Monte Carlo simulation of a clinical linear accelerator. Appl Radiat Isotopes, 55(2001)6, pp. 759-65.
[74] Keall, P.J., Siebers, J.V., Libby, B., Mohan, R. Determining the incident electron fluence for Monte Carlo-based photon treatment planning using a standard measured data set. Med Phys, 30(2003)4, pp. 574-82.
[75] Tzedakis, A., Damilakis, J.E., Mazonakis, M., Stratakis, J., Varveris, H., Gourtsoyiannis, N. Influence of initial electron beam parameters on Monte Carlo calculated absorbed dose distributions for radiotherapy photon beams. Med Phys, 31(2004)4, pp. 907-13.
[76] Pena, J., Franco, L., Gomez, F., Iglesias, A., Lobato, R., Mosquera, J., Pazos, A., Pardo, J., Pombar, M., Rodriguez, A., Sendon, J. Commissioning of a medical accelerator photon beam Monte Carlo simulation using wide-field profiles. Phys Med Biol, 49(2004)21, pp. 4929-42.
[77] Cho, S. H., Vassiliev, O.N., Lee, S., Liu, H.H., Ibbott, G.S., Mohan, R. Reference photon dosimetry data and reference phase space data for the 6 MV photon beam from Varian Clinac 2100 series linear accelerators. Med Phys, 32(2005)1, pp. 137-48.
[78] Pena, J., González-Castaño, D.M., Gómez, F., Sanchez-Doblado, F., Hartmann, G.H. Automatic determination of primary electron beam parameters in Monte Carlo simulation. Med Phys, 34(2007)3, pp. 1076-84.
[79] Ding, G.X. Using Monte Carlo simulations to commission photon beam output factors--a feasibility study. Phys Med Biol, 48(2003)23, pp. 3865-74.
[80] Ding, G.X., Duzenli, C., Kalach, N.I. Are neutrons responsible for the dose discrepancies between Monte Carlo calculations and measurements in the build-up region for a high-energy photon beam? Phys Med Biol, 47(2002)17, pp. 3251-61.
[81] Abdel-Rahman, W., Seuntjens, J.P., Verhaegen, F., Deblois, F., Podgorsak, E.B. Validation of Monte Carlo calculated surface doses for megavoltage photon beams. Med Phys, 32(2005)1, pp. 286-98.
[82] Ververs, J.D., Schaefer, M.J., Kawrakow, I., Siebers, J.V. A method to improve accuracy and precision of water surface identification for photon depth dose measurements. Med Phys, 36(2009)4, pp. 1410-20.
[83] Kim, J.H., Hill, R., Kuncic, Z. An evaluation of calculation parameters in the EGSnrc/BEAMnrc Monte Carlo codes and their effect on surface dose calculation. Phys Med Biol, 57(2012)14, pp. N267-78.

[84] Chibani, O., Ma, C.M. On the discrepancies between Monte Carlo dose calculations and measurements for the 18 MV Varian photon beam. Med Phys, 34(2007)4, pp. 1206-1216.
[85] Sheikh-Bagheri, D., Rogers, D.W.O., Ross, C.K., Seuntjens, J.P. Comparison of measured and Monte Carlo calculated dose distributions from the NRC linac. Med Phys, 27(2000)10, pp. 2256-66.
[86] De Vlamynck, K., Palmans, H., Verhaegen, V., De Wagter, C., De Neve, W., Thierens, H. Dose measurements compared with Monte Carlo simulations of narrow 6 MV multileaf collimator shaped photon beams. Med Phys, 26(1999)9, pp. 1874-82.
[87] González, W., Lallena, A.M., Alfonso, R. Monte Carlo simulation of the dynamic micro-multileaf collimator of a LINAC Elekta Precise using PENELOPE. Phys Med Biol, 56(2011)11, pp. 3417-31.
[88] Belec, J., Patrocinio, H., Verhaegen, F. Development of a Monte Carlo model for the Brainlab microMLC. Phys Med Biol, 50(2005)5, pp. 787-99.
[89] Kairn, T., Kenny, J., Crowe, S.B., Fielding, A.L., Franich, R.D., Johnston, P.N., Knight, R.T., Langton, C.M., Schlect, D., Trapp, J.V. Technical Note: Modeling a complex micro-multileaf collimator using the standard BEAMnrc distribution. Med Phys, 37(2010)4, pp. 1761-67.
[90] Kairn, T., Aland, T., Franich, R.D., Johnston, P.N., Kakakhel, M.B., Kenny, J., Knight, R.T,, Langton, C.M., Schlect, D., Taylor, M.L., Trapp, J.V. Adapting a generic BEAMnrc model of the BrainLAB m3 micro-multileaf collimator to simulate a local collimation device. Phys Med Biol, 55(2010)17, pp. N451-63.
[91] Kapur, A., Ma, C.-M., Boyer, A.L. Monte Carlo simulations for multileaf-collimator leaves: design and dosimetry. World Congress on Medical Physics and Biomedical Engineering (2000), Med Phys, 27 (2000)6, p. 1410 (abstract).
[92] Keall, P.J., Siebers, J.V., Arnfield, M., Kim, J.O., Mohan, R. Monte Carlo dose calculations for dynamic IMRT treatments. Phys Med Biol, 46(2001)4, pp. 929-41.
[93] Kim, J.O., Siebers, J.V., Keall, P.J., Arnfield, M.R., Mohan, R. A Monte Carlo study of radiation transport through multileaf collimators. Med Phys, 28(2001)12, pp. 2497-506.
[94] Siebers, J.V., Keall, P.J., Kim, J.O., Mohan, R. A method for photon beam Monte Carlo multileaf collimator particle transport. Phys Med Biol, 47(2002)17, pp. 3225-49.
[95] Liu, H.H., Verhaegen, F., Dong, L. A method of simulating dynamic multileaf collimators using Monte Carlo techniques for intensity-modulated radiation therapy. Phys Med Biol, 46(2001)9, pp. 2283-98.
[96] Heath, H., Seuntjens, J. Development and validation of a BEAMnrc component module for accurate Monte Carlo modelling of the Varian dynamic Millennium multileaf collimator. Phys Med Biol, 48(2003)24, 4045-63.
[97] Tyagi, N., Moran, J.M., Litzenebrg, D.W., Bielajew, A.F., Fraass, B.A., Chetty, I.J. Experimental verification of a Monte Carlo-based MLC simulation model for IMRT dose calculation. Med Phys, 34(2007)2, 651-63.

[98] Fix, M.K., Volken, W., Frei, D., Frauchiger, D., Born, E.J., Manser, P. Monte Carlo implementation, validation, and characterization of a 120 leaf MLC. Med Phys, 38(2011)10, 5311-20.
[99] Borges, C., Zarza-Moreno, M., Heath, E., Teixeira, N., Vaz, P. Monte Carlo modeling and simulations of the High Definition (HD120) micro MLC and validation against measurements for a 6 MV beam. Med Phys, 39(2012)1, pp. 415-23.
[100] Ding, G.X., Rogers, D.W.O., Mackie, T.R. Calculation of stopping-power ratios using realistic clinical electron beams. Med Phys, 22(1995)5, pp. 489-502.
[101] Burns, D.T., Ding, G.X., Rogers, D.W.O. R50 as a beam quality specifier for selecting stopping-power ratios and reference depths for electron dosimetry. Med Phys, 23(1996)3, pp. 383-8.
[102] Ding, G.X., Rogers, D.W.O. Mean energy, energy-range relationship and depth-scaling factor for clinical electron beams. Med Phys, 23(1996)3, pp. 361-76.
[103] Ma, C.-M., Faddegon, B.A., Rogers, D.W.O., Mackie, T.R. Accurate characterization of Monte Carlo calculated electron beams for radiotherapy. Med Phys, 24(1997)3, pp. 401-16.
[104] Bieda, M.R., Antolak, J.A., Hogstrom, K.R. The effect of scattering foil parameters on electron-beam Monte Carlo calculations. Med Phys, 28(2001)12, pp. 2527-34.
[105] Verhaegen, F., Mubata, C., Pettingell, J., Bidmead, A.M., Rosenberg, I., Mockbridge, D., Nahum, A.E. Monte Carlo calculation of output factors for circular, rectangular, and square fields of electron accelerators (6–20 MeV). Med Phys, 28(2001)6, pp. 938-49.
[106] Antolak, J.A., Bieda, M.R., Hogstrom, K.R. Using Monte Carlo methods to commission electron beams: A feasibility study. Med Phys, 29(2002)5, pp. 771-86.
[107] Faddegon, B.A., Sawkey, D., O'Shea, T., McEwen, M., Ross, C. Treatment head disassembly to improve the accuracy of large electron field simulation. Med Phys, 36(2009)10, pp. 4577-91.
[108] O'Shea, T.P., Sawkey, D.L., Foley, M.J., Faddegon, B.A. Monte Carlo commissioning of clinical electron beams using large field measurements. Phys Med Biol, 55(2010)14, pp. 4083-105.
[109] Shimozato, T., Okudaira, K., Fuse, H., Tabushi, K. Monte Carlo simulation and measurement of radiation leakage from applicators used in external electron radiotherapy. Phys Med, 29(2013)4, pp. 388-96.
[110] Schneider, W., Bortfeld, T., Schlegel, W. Correlation between CT numbers and tissue parameters needed for Monte Carlo simulations of clinical dose distributions. Phys Med Biol, 45(2000)2, pp. 459-78.
[111] Verhaegen, F., Devic, S. Sensitivity study for CT image use in Monte Carlo treatment planning. Phys Med Biol, 50(2005)5, pp. 937-46.
[112] Vanderstraeten, B., Chin, P.W., Fix, M., Leal, A., Mora, G., Reynaert, N., Seco, J., Soukup, M., Spezi, E., De Neve, W., Thierens, H. Conversion of CT numbers into tissue parameters for Monte Carlo dose calculations: a multi-centre study. Phys Med Biol, 52(2007)3, pp. 539-62.

[113] Zarza-Moreno, M., Cardoso, I., Teixeira, N., Jesus, A.P., Mora, G. The use of non-standard CT conversion ramps for Monte Carlo verification of 6 MV prostate IMRT plans. Phys Med, 29(2013)4, pp. 357-67.
[114] Coolens, C., Childs, P.J. Calibration of CT Hounsfield units for radiotherapy treatment planning of patients with metallic hip prostheses: the use of the extended CT-scale. Phys Med Biol, 48(2003)11, pp. 1591-603.
[115] Arnfield, M.R., Siantar, C.H., Siebers, J., Garmon, P., Cox, L., Mohan, R. The impact of electron transport on the accuracy of computed dose. Med Phys, 27(2000)6, pp. 1266-74.
[116] Chetty, I.J., Charland, P.M., Tyagi, N., McShan, D.L., Fraass, B.A., Bielajew, A.F. Photon beam relative dose validation of the DPM Monte Carlo code in lung-equivalent media. Med Phys, 30(2003)4, pp. 563-73.
[117] Carrasco, P., Jornet, N., Duch, M.A., Weber, L., Ginjaume, M., Eudaldo, T., Jurado, D., Ruiz, A., Ribas, M. Comparison of dose calculation algorithms in phantoms with lung equivalent heterogeneities under conditions of lateral electronic disequilibrium. Med Phys, 31(2004)10, pp. 2899-911.
[118] Paelinck, L., Reynaert, N., Thierens, H., De Neve, W., De Wagter, C. Experimental verification of lung dose with radiochromic film: comparison with Monte Carlo simulations and commercially available treatment planning systems. Phys Med Biol, 50(2005)9, pp. 2055-69
[119] Wang, L., Lovelock, M., Chui, C.S. Experimental verification of a CT-based Monte Carlo dose-calculation method in heterogeneous phantoms. Med Phys, 26(1999)12, pp. 2626-34.
[120] Doucet, R., Olivares, M., DeBlois, F., Podgorsak, E.B., Kawrakow, I., Seuntjens, J. Comparison of measured and Monte Carlo calculated dose distributions in inhomogeneous phantoms in clinical electron beams. Phys Med Biol, 48(2003)15, pp. 2339-54.
[121] Chow, J.C., Grigorov, G.N. Dosimetry of a small air cavity for clinical electron beams: A Monte Carlo study. Med Dosim, 35(2010)2, pp. 92-100.
[122] Reft, C., Alecu, R., Das, I.J., Gerbi, B.J., Keall, P., Lief, E., Mijnheer, B.J., Papanikolaou, N., Sibata, C., Van Dyk, J. Dosimetric considerations for patients with HIP prostheses undergoing pelvic irradiation. Report of the AAPM Radiation Therapy Committee Task Group 63. Med Phys, 30(2003)6, pp. 1162-82.
[123] Aubry, J.F., Bouchard, H., Bessières, I., Lacroix, F. Validation of an electron Monte Carlo dose calculation algorithm in the presence of heterogeneities using EGSnrc and radiochromic film measurements. J Appl Clin Med Phys, 12(2011)4, pp. 3392.
[124] Harrison, K.M., Ebert, M.A., Kron, T., Howlett, S.J., Cornes, D., Hamilton, C.S., Denham, J.W. Design, manufacture, and evaluation of an anthropomorphic pelvic phantom purpose-built for radiotherapy. Med Phys, 38(2011)10, pp. 5330-7.
[125] Struelens, L., Vanhavere, F., Smans, K. Experimental validation of Monte Carlo calculations with a voxelized Rando-Alderson phantom: a study on influence parameters. Phys Med Biol, 53(2008)20, pp. 5831-44.

[126] Benedict, S.H., Yenice, K.M., Followill, D., Galvin, J.M., Hinson, W., Kavanagh, B., Keall, P., Lovelock, M., Meeks, S., Papiez, L., Purdie, T., Sadagopan, R., Schell, M.C., Salter, B., Schlesinger, D.J., Shiu, A.S., Solberg, T., Song, D.Y., Stieber, V., Timmerman, R., Tomé, W.A., Verellen, D., Wang, L., Yin, F.F. Stereotactic body radiation therapy: the report of AAPM Task Group 101. Med Phys, 37(2010)8, pp. 4078-101.
[127] Gerbi, B.J., Antolak, J.A., Deibel, F.C., Followill, D.S., Herman, M.G., Higgins, P.D., Huq, M.S., Mihailidis, D.N., Yorke, E.D., Hogstrom, K.R., Khan, F.M. Recommendations for clinical electron beam dosimetry: supplement to the recommendations of Task Group 25. Med Phys, 36(2009)7, pp. 3239-79.
[128] Francescon, P., Cavedon, C., Reccanello, S., Cora, S. Photon dose calculation of a three-dimensional treatment planning system compared to the Monte Carlo code BEAM. Med Phys, 27(2000)7, pp. 1579-87.
[129] Francescon, P., Cora, S., Chiovati, P. Dose verification of an IMRT treatment planning system with the BEAM EGS4-based Monte Carlo code. Med Phys, 30(2003)2, pp. 144-57.
[130] Seco, J., Adams, E., Bidmead, M., Partridge, M., Verhaegen, F. Head-and-neck IMRT treatments assessed with a Monte Carlo dose calculation engine. Phys Med Biol, 50(2005)5, pp. 817-30.
[131] Dogan, N., Siebers, J.V., Keall, P.J. Clinical comparison of head and neck and prostate IMRT plans using absorbed dose to medium and absorbed dose to water. Phys Med Biol, 51(2006)19, pp. 4967-80.
[132] Gagne, I.M., Ansbacher, W., Zavgorodni, S., Popescu, C., Beckham, W.A. A Monte Carlo evaluation of RapidArc dose calculations for oropharynx radiotherapy. Phys Med Biol, 53(2008)24, pp. 7167-85.
[133] Chakarova, R., Müntzing, K., Krantz, M., Hedin, E., Hertzman, S. Monte Carlo optimization of total body irradiation in a phantom and patient geometry. Phys Med Biol, 58(2013)8, pp. 2461-9.
[134] Moiseenko, V., Liu, M., Bergman, A.M., Gill, B., Kristensen, S., Teke, T., Popescu, I.A. Monte Carlo calculation of dose distribution in early stage NSCLC patients planned for accelerated hypofractionated radiation therapy in the NCIC-BR25 protocol. Phys Med Biol, 55(2010)3, pp. 723-33.
[135] Shokrani, P., Baradaran-Ghahfarokhi, M., Zadeh, M.K. A novel approach in electron beam radiation therapy of lips carcinoma: a Monte Carlo study. Med Phys, 40(2013)4, p. 041720.
[136] Ma, C.-M., Li, J.S., Pawlicki, T., Jiang, S.B., Deng, J., Lee, M.C., Koumrian, T., Luxton, M., Brain, S. A Monte Carlo dose calculation tool for radiotherapy treatment planning. Phys Med Biol, 47(2002)10, pp. 1671-89.
[137] Pawlicki, T., Ma, C.-M. Monte Carlo simulation for MLC-based intensity-modulated radiotherapy. Med Dosim, 26(2001)2, pp. 157-68.
[138] Bush, K., Townson, R., Zavgorodni, S. Monte Carlo simulation of RapidArc radiotherapy delivery. Phys Med Biol, 53(2008)19, pp. N359-70.
[139] Teke, T., Bergman, A.M., Kwa, W., Gill, B., Duzenli, C., Popescu, I.A. Monte Carlo based, patient-specific RapidArc QA using Linac log files. Med Phys, 37(2010)1, pp. 116-23.

[140] Gete, E., Duzenli, C., Milette, M.P., Mestrovic, A., Hyde, D., Bergman, A.M., Teke, T. A Monte Carlo approach to validation of FFF VMAT treatment plans for the TrueBeam linac. Med Phys, 40(2013), p. 021707.
[141] Alexander, A., Deblois, F., Stroian, G., Al-Yahya, K., Heath, E., Seuntjens, J. MMCTP: a radiotherapy research environment for Monte Carlo and patient-specific treatment planning. Phys Med Biol, 52(2007)13, pp. N297-308.
[142] Yamamoto, T., Mizowaki, T., Miyabe, Y., Takegawa, H., Narita, Y., Yano, S., Nagata, Y., Teshima, T., Hiraoka, M. An integrated Monte Carlo dosimetric verification system for radiotherapy treatment planning. Phys Med Biol, 52(2007)7, pp. 1991-2008.
[143] Mukumoto, N., Tsujii, K., Saito, S., Yasunaga, M., Takegawa, H., Yamamoto, T., Numasaki, H., Teshima, T. A preliminary study of in-house Monte Carlo simulations: an integrated Monte Carlo verification system. Int J Radiat Oncol Biol Phys, 75(2009)2, pp. 571-9.
[144] Magaddino, V., Manser, P., Frei, D., Volken, W., Schmidhalter, D., Hirschi, L., Fix, MK.. Validation of the Swiss Monte Carlo Plan for a static and dynamic 6 MV photon beam. Z Med Phys, 21(2011)2, pp. 124-34.
[145] Wieslander, E., Knöös, T. A virtual-accelerator-based verification of a Monte Carlo dose calculation algorithm for electron beam treatment planning in clinical situations. Radiother Oncol, 82(2007)7, pp. 208-17.
[146] Pinter, C., Lasso, A., Wang, A., Jaffray, D., Fichtinger, G. SlicerRT: radiation therapy research toolkit for 3D Slicer. Med Phys, 39(2012)10, pp. 6332-8.
[147] Deasy, J.O., Blanco, A.I., Clark, V.H. CERR: A computational environment for radiotherapy research. Med Phys, 30(2003)5, pp. 979-85.
[148] Spezi, E., Lewis, D.G., Smith, C.W. A DICOM-RT-based toolbox for the evaluation and verification of radiotherapy plans. Phys Med Biol, 47(2002)23, pp. 4223-32.
[149] Ojala, J. Application of Monte Carlo simulations in commissioning of radiotherapy dose calculation algorithms. Thesis for Licentiate's degree. Tampere University of Technology. Tampere 2012. 78 p.
[150] Hendee, W.R., Ibbott, G.S., Hendee, E.G. Radiation Therapy Physics (3rd edition). Wilmington, 2004. Wiley-Liss. 472 p.
[151] Boyer, A.L., Li, S. Geometric analysis of light-field position of a multileaf collimator with curved ends. Med Phys, 24(1997)5, pp. 757-62.
[152] Goede, M.R., Gooden, D.S., Ellis, R.G., Brickner, T.J. Jr. A versatile electron collimation system to be used with electron cones supplied with Varian's Clinac 18. Int J Radiat Oncol Biol Phys, 2(1977)7-8, pp. 791-5.
[153] Hogstrom, K.R., Almond, P.R. Review of electron beam therapy physics. Phys Med Biol, 51(2006)13, pp. R455-89.
[154] Fragoso, M., Kawrakow, I., Faddegon, B.A., Solberg, T.D., Chetty, I.J. Fast, accurate photon beam accelerator modeling using BEAMnrc: A systematic investigation of efficiency enhancing methods and cross-section data. Med Phys, 36(2009)12, pp. 5451–66.
[155] Liu, H.H., Mackie, T.R., McCullough, E.C. Modeling photon output caused by backscattered radiation into the monitor chamber from collimator jaws using a Monte Carlo technique. Med Phys, 27(2000)4, pp. 737-44.

[156] Verhaegen, F., Symonds-Tayler, R., Liu, H.H., Nahum, A.E. Backscatter towards the monitor ion chamber in high-energy photon and electron beams: charge integration versus Monte Carlo simulation. Phys Med Biol, 45(2000)11, pp. 3159-70.
[157] Popescu, I.A., Shaw, C.P., Zavgorodni, S.F., Beckham, W.A. Absolute dose calculations for Monte Carlo simulations of radiotherapy beams. Phys Med Biol, 50(2005)14, pp. 3375-92.
[158] Ojala, J., Sipilä, S., Hyödynmaa, S., Pitkänen, M. Validation of a 6 MV Varian iX linear accelerator Monte Carlo model using a combination of IC and radiochromic film measurements. Radiother Oncol, 96(2010)S1, pp. S478–S494.
[159] Low, D.A., Harms, W.B., Mutic, S., Purdy, J.A. A technique for the quantitative evaluation of dose distributions. Med Phys, 25(1998)5, pp. 656-61.
[160] Low, D.A., Dempsey, J.F. Evaluation of the gamma dose distribution comparison method. Med Phys, 30(2003)9, pp. 2455-64.
[161] Sipilä, P., Järvinen, H., Jokelainen, I., Ojala, J., Niemelä, J. Radiochromic film dosimetry: Computer controlled densitometer. Radiother Oncol, 96(2010)S1, pp. S467–S478.
[162] Storchi, P., Woudstra, E. Calculation of the absorbed dose distribution due to irregularly shaped photon beams using pencil beam kernels derived form basic beam data. Phys Med Biol, 41(1996)4, pp. 637-56.
[163] Storchi, P.R., van Battum, L.J., Woudstra, E. Calculation of a pencil beam kernel from measured photon beam data. Phys Med Biol, 44(1999)12, pp. 2917-28.
[164] Webb, S., Fox, R.A. Verification by Monte Carlo methods of a power law tissue-air ratio algorithm for inhomogeneity corrections in photon beam dose calculations. Phys Med Biol, 25(1980)2, pp. 225-40.
[165] Ulmer, W., Harder, D. A triple Gaussian pencil beam model for photon beam treatment planning. Z Med Phys, 5(1995), pp. 25-30.
[166] Ulmer, W., Harder, D. Applications of a triple Gaussian pencil beam model for photon beam treatment planning. Z Med Phys, 6(1996), pp. 68-74.
[167] Ulmer, W., Pyyry, J., Kaissl, W. A 3D photon superposition/convolution algorithm and its foundation on results of Monte Carlo calculations. Phys Med Biol, 50(2005)8, pp. 1767-90.
[168] Vassiliev, O.N., Wareing, T.A., McGhee, J., Failla, G., Salehpour, M.R., Mourtada, F. Validation of a new grid-based Boltzmann equation solver for dose calculation in radiotherapy with photon beams. Phys Med Biol, 55(2010)3, pp. 581-98.
[169] Han, T., Mikell, J.K., Salehpour, M., Mourtada, F. Dosimetric comparison of Acuros XB deterministic radiation transport method with Monte Carlo and model-based convolution methods in heterogeneous media. Med Phys, 38(2011)5, pp. 2651-64.
[170] Lax, I., Blomgren, H., Naslund, I., Svanstrom, R. Stereotactic radiotherapy of malignancies in the abdomen. Methodological aspects. Acta Oncol, 33(1994)6, pp. 677-83.
[171] Sipilä, P., Järvinen, H., Kosunen, A., I., Ojala, J., Niemelä, J. Multipurpose, semianatomical water phantom for TPS verification. Book of Extended

Synopses. IAEA-CN-182. International Symposium on Standards, Applications and Quality Assurance in Medical Radiation Dosimetry (IDOS). 2010 Nov 9-12; Vienna, Austria. pp. 459-60.
[172] Ojala, J., Hyödynmaa, S. MC-based verification of absorbed dose distributions in the lung calculated by two electron beam algorithms. Radiother Oncol, 99(2011)S1, pp. S177.
[173] Lax, I. Development of a generalized Gaussian model for absorbed dose calculation and dose planning in therapeutic electron beams. Ph.D. Thesis. University of Stockholm 1986. 58 p.
[174] Hyödynmaa, S. Implementations of the generalised Gaussian pencil beam algorithm for three-dimensional electron beam dose planning. Ph.D. Thesis. Technical Research Centre of Finland. Publications 74. Espoo 1991. 95 p.
[175] Neuenschwander, H., Mackie, T.R., Reckwerdt, P.J. MMC--a high-performance Monte Carlo code for electron beam planning. Phys Med Biol, 40(1995)4, pp. 543-74.
[176] Janssen, J.J., Korevaar, E.W., van Battum, L.J., Storchi, P.R., Huizenga, H. A model to determine the initial phase space of a clinical electron beam from measured beam data. Phys Med Biol, 46(2001)2, pp. 269-86.
[177] Rana, S., Rogers, K., Lee, T., Reed, D., Biggs, C. Verification and Dosimetric Impact of Acuros XB Algorithm for Stereotactic Body Radiation Therapy (SBRT) and RapidArc Planning for Non-Small-Cell Lung Cancer (NSCLC) Patients. International Journal of Medical Physics, Clinical Engineering and Radiation Oncology, 2(2013)1, pp. 6-14.
[178] Han, T., Followill, D., Mikell, J., Repchak, R., Molineu, A., Howell, R., Salehpour, M., Mourtada, F. Dosimetric impact of Acuros XB deterministic radiation transport algorithm for heterogeneous dose calculation in lung cancer. Med Phys, 40(2013)5, p. 051710.
[179] Fogliata, A., Nicolini, G., Clivio, A., Vanetti, E., Cozzi, L. Dosimetric evaluation of Acuros XB Advanced Dose Calculation algorithm in heterogeneous media. Radiat Oncol, 19(2011)7, p. 82.
[180] Lloyd, S.A., Ansbacher, W. Evaluation of an analytic linear Boltzmann transport equation solver for high-density inhomogeneities, Med Phys, 40(2013)1, p. 011707.
[181] Ding, G.X., Duggan, D.M., Coffey, C.W., Shokrani, P., Cygler, J.E. First macro Monte Carlo based commercial dose calculation module for electron beam treatment planning--new issues for clinical consideration. Phys Med Biol, 51(2006)11, pp. 2781-99.
[182] Coleman, J., Park, C., Villarreal-Barajas, J.E., Petti, P., Faddegon, B. A comparison of Monte Carlo and Fermi-Eyges-Hogstrom estimates of heart and lung dose from breast electron boost treatment. Int J Radiat Oncol Biol Phys, 61(2005)2, pp. 621-8.
[183] Sempau, J., Sánchez-Reyes, A., Salvat, F., ben Tahar, H.O., Jiang, S.B., Fernández-Varea, J.M. Monte Carlo simulation of electron beams from an accelerator head using PENELOPE. Phys Med Biol, 46(2001)4, pp. 1163-86.

[184] Siebers, J.V., Keall, P.J., Nahum, A.E., Mohan, R. Converting absorbed dose to medium to absorbed dose to water for Monte Carlo based photon beam dose calculations. Phys Med Biol, 45(2000)4, pp. 983-95.
[185] El Naqa, I., Kawrakow, I., Fippel, M., Siebers, J.V., Lindsay, P.E., Wickerhauser, M.V., Vicic, M., Zakarian, K., Kauffmann, N., Deasy, J.O. A comparison of Monte Carlo dose calculation denoising techniques. Phys Med Biol, 50(2005)5, pp. 909-22.
[186] Kawrakow, I. On the de-noising of Monte Carlo calculated dose distributions. Phys Med Biol, 47(2002)17, pp. 3087-103.

ORIGINAL PUBLICATIONS

Publication I

Ojala, J., Hyödynmaa, S., Pitkänen, M.

BEAMnrc Monte Carlo modelling of linear accelerator using parallel computing grid – validation of a common, fixed geometry model for photon and electron beams.

Conference Proceedings for the XVIth International Conference on the Use of Computers in Radiation Therapy (ICCR). 2010. 4 p.

Publication II

Ojala, J., Kapanen, M., Hyödynmaa, S., Wigren, T., Pitkänen, M.

Performance of dose calculation algorithms from three generations in lung SBRT: comparison with full Monte Carlo-based dose distributions.

J Appl Clin Med Phys, 15(2014)2, pp. 4-18.

JOURNAL OF APPLIED CLINICAL MEDICAL PHYSICS, VOLUME 15, NUMBER 2, 2014

Performance of dose calculation algorithms from three generations in lung SBRT: comparison with full Monte Carlo-based dose distributions

Jarkko J. Ojala,[1,2a] Mika K. Kapanen,[1,2] Simo J. Hyödynmaa,[2] Tuija K. Wigren,[1] Maunu A. Pitkänen[1,2]
Department of Oncology,[1] Unit of Radiotherapy, Tampere University Hospital, Tampere, Finland; Department of Medical Physics,[2] Medical Imaging Center, Tampere University Hospital, Tampere, Finland
jarkko.ojala@pshp.fi

Received 7 August, 2013; accepted 25 September, 2013

The accuracy of dose calculation is a key challenge in stereotactic body radiotherapy (SBRT) of the lung. We have benchmarked three photon beam dose calculation algorithms — pencil beam convolution (PBC), anisotropic analytical algorithm (AAA), and Acuros XB (AXB) — implemented in a commercial treatment planning system (TPS), Varian Eclipse. Dose distributions from full Monte Carlo (MC) simulations were regarded as a reference. In the first stage, for four patients with central lung tumors, treatment plans using 3D conformal radiotherapy (CRT) technique applying 6 MV photon beams were made using the AXB algorithm, with planning criteria according to the Nordic SBRT study group. The plans were recalculated (with same number of monitor units (MUs) and identical field settings) using BEAMnrc and DOSXYZnrc MC codes. The MC-calculated dose distributions were compared to corresponding AXB-calculated dose distributions to assess the accuracy of the AXB algorithm, to which then other TPS algorithms were compared. In the second stage, treatment plans were made for ten patients with 3D CRT technique using both the PBC algorithm and the AAA. The plans were recalculated (with same number of MUs and identical field settings) with the AXB algorithm, then compared to original plans. Throughout the study, the comparisons were made as a function of the size of the planning target volume (PTV), using various dose-volume histogram (DVH) and other parameters to quantitatively assess the plan quality. In the first stage also, 3D gamma analyses with threshold criteria 3%/3 mm and 2%/2 mm were applied. The AXB-calculated dose distributions showed relatively high level of agreement in the light of 3D gamma analysis and DVH comparison against the full MC simulation, especially with large PTVs, but, with smaller PTVs, larger discrepancies were found. Gamma agreement index (GAI) values between 95.5% and 99.6% for all the plans with the threshold criteria 3%/3 mm were achieved, but 2%/2 mm threshold criteria showed larger discrepancies. The TPS algorithm comparison results showed large dose discrepancies in the PTV mean dose ($D_{50\%}$), nearly 60%, for the PBC algorithm, and differences of nearly 20% for the AAA, occurring also in the small PTV size range. This work suggests the application of independent plan verification, when the AAA or the AXB algorithm are utilized in lung SBRT having PTVs smaller than 20–25 cc. The calculated data from this study can be used in converting the SBRT protocols based on type 'a' and/or type 'b' algorithms for the most recent generation type 'c' algorithms, such as the AXB algorithm.

PACS numbers: 87.55.-x, 87.55.D-, 87.55.K-, 87.55.kd, 87.55.Qr

[a] Corresponding author: Jarkko Ojala, Department of Oncology, Unit of Radiotherapy, Tampere University Hospital (TAUH), P.O. Box 2000, 33521 Tampere, Finland; phone: +358 3 311 63212; fax: +358 3 311 63001; email: jarkko.ojala@pshp.fi

Key words: Monte Carlo dose calculation, Acuros, AXB, SBRT, photon beam radiotherapy

Conflict of Interest statement: The authors declare that they have no conflicts of interest. The authors alone are responsible for the content and writing of the paper.

I. INTRODUCTION

Stereotactic body radiotherapy (SBRT) has attained a status of the treatment technique of choice for malignancies in several anatomical locations. After its first implementation to extracranial treatments reported by Lax et al.[1] in 1994, SBRT has evolved to its present form. The principle of SBRT is based on delivering large doses to planning target volume (PTV) in a single fraction or in a few fractions. Compared to conventional radiotherapy fractionation schemes, this results in higher potential biological effect. In the normal tissue toxicity minimization, the PTV volume plays a key role (i.e., the larger the PTV volume, the larger probability there is for adverse normal tissue complications). Therefore, SBRT is applied only for tumors with diameters not larger than 5 cm, and the size of the PTV has to be minimized. This is achieved with small, patient-specific target margins, which result from accurate patient positioning and immobilization, and modern image-guidance. Five to seven or more conformal static treatment fields or arc techniques, such as volumetric-modulated arc therapy (VMAT), enable rapid dose falloff away from target, which spares the normal tissue around the PTV. The history, development, and application of SBRT has been thoroughly presented in several review articles,[2-3] clinical trial and protocol reports,[4-8] and other comprehensive papers[9] by numerous research groups.

One of the major challenges in lung SBRT is the accuracy of the dose calculation. Challenges originate from the issues related to small-field dosimetry, since measured data are required in dose calculation algorithm configuration. This has consequences, especially with measurement-based algorithms, whereas with model-based algorithms the inherent performance of the algorithm defines the achievable accuracy level. In dose calculation, largest inaccuracies occur in areas of steep dose gradients being largest in small fields delivered through heterogeneities having low density, such as the lung tissue. This is due to the inability of dose calculation algorithms to model lateral electron transport, especially in a state of "electronic disequilibrium". The discrepancies are specific especially to type 'a' algorithms, which are usually based on pencil beam convolution principles. More advanced type 'b' algorithms, based on superposition convolution principles, produce more accurate results, but the differences are still too large in most complex cases when compared to reference methods.[3] Recently, a next-generation dose calculation algorithm has been released, for which preliminary results in homogeneous[10-11] and heterogeneous[12-16] phantoms are superior when compared to conventional algorithms.

In radiotherapy, full Monte Carlo (MC) simulations are considered to provide dose distributions that can be used as a primary reference for various purposes.[17] There are several studies available exploiting MC methods in benchmarking commercial dose calculation algorithms and, in the case of clinical lung SBRT, plan dose comparisons with full[18-19] and fast[20-23] MC codes have been carried out. These studies have reported dosimetric discrepancies for the minimum dose in PTV to be as large as about 40% for type 'a' algorithms and about 10% for type 'b' algorithms. However, studies concerning dose calculation accuracy in lung SBRT with the most recent generation of algorithms and full MC simulation have not yet been reported. In the study by Rana et al.[16] a type 'b' algorithm was compared to the calculation results of a new generation algorithm in lung SBRT treatments, finding differences up to 10%.

The goal in this work is to compare lung SBRT plan dose distributions obtained with dose calculation algorithms of different generations implemented in Eclipse treatment planning system (TPS) by Varian Medical Systems, Inc. (VMS) (Palo Alto, CA, USA). In TPS algorithm comparison, we used one of the algorithms (the most recent dose calculation algorithm by

VMS, Acuros XB (AXB) algorithm) as the baseline for other TPS algorithms. To evaluate the accuracy of the AXB algorithm, we recalculated selected AXB-calculated plans with the full MC model and compared the dose distributions with gamma analysis, quantitative dose-volume histogram (DVH) parameters, and dose difference profiles. After assessing the accuracy of the AXB algorithm, we created ten SBRT treatment plans for the lung with pencil beam convolution (PBC) algorithm (type 'a') and anisotropic analytical algorithm (AAA) (type 'b'). We benchmarked the algorithms with respect to DVH parameters of the PTV, ipsilateral lung, and spinal cord by preparing optimal plans using both algorithms and then recalculated the plans with the AXB algorithm (which here is categorized as type 'c' algorithm), to allow the mutual comparison. In our study, the comparison has been taken to the next level from the study by Rana et al.[16] by comparing the calculation results to full MC simulation and providing results compared to type 'a' algorithm. Another merit of this work is in that, whereas in other earlier studies comparisons are based on calculations and measurements in virtual phantoms, we have performed the full MC-based comparisons in clinical patient plans, with which measurement-based verification methods inside patients are impossible to apply.

This study has two motivations. On one hand, the inclusion of the widely decommissioned type 'a' algorithm enables the reader to retrospectively link its dosimetric aspects to the analysis of treatment outcomes. Also, since the published data are mostly based on dose calculations with type 'a' algorithm, the results of our study contributes to transferring of this data through type 'b' algorithm results to most recent type 'c' algorithm. On the other hand, this study demonstrates the performance of the new type 'c' algorithm for lung SBRT dose calculation with clinical plans. Requests for this kind of study can be found in the literature.[8,11] At the authors' clinic, the value of the work is self-evident because, after the commissioning of lung SBRT for clinical use in 1999, for 75% of over 150 patients treated to date, the treatment plans have been calculated with the PBC algorithm (type 'a') and the rest with the AAA (type 'b'). Our investigation on the treatment outcomes, with dosimetric analysis, will take place in the near future, as will also the commissioning of the AXB algorithm (type 'c'), after comprehensive benchmarking.

II. MATERIALS AND METHODS

A. The TPS dose calculation algorithms

In this study, version 10.0 of the Eclipse TPS and version 10.0.28 of the algorithms were used. Commissioning of the algorithms was performed strictly following manufacturer's manuals and recommendations, using the same measurement data for all algorithms, where applicable, and default configuration settings. The smallest field size in output factor configuration was 2×2 cm^2 for all the algorithms and it was smaller than the smallest field size (defined by the jaws) needed in dose calculations. The measurements were performed with IBA SFD DEB050 stereotactic field detector (IBA Dosimetry AB, Sweden) for 2×2 to 4×4 cm^2 fields, and with PTW TM31002 Semiflex ionization chamber (IC) (PTW Freiburg GmbH, Germany) for 3×3 to 40×40 cm^2 fields using a motorized scanning system in an MP3 water phantom (PTW Freiburg GmbH). The output factor measurement results were daisy-chained, as presented by Dieterich et al.[24] The PBC algorithm is an analytical correction-based algorithm where the dose is calculated by convoluting the field intensity fluence with narrow pencil beam kernels. Subsequently, corrections for patient surface obliquity and heterogeneities are performed.[25-27] The AAA is a semi-analytical, model-based algorithm, although its core is built on exploiting pencil beams. The pencil beams are determined from Monte Carlo simulations, fitted to user-supplied beam measurements, after which three separate subsources — primary photons, extrafocal photons, and electron contamination — are modeled. Heterogeneity correction in the AAA is partly similar to the one in PBC algorithm, but to some extent, it also takes into account the scattered radiation from the surroundings of the calculation point (i.e., in the lateral

scaling of the medium it applies six independent exponential functions to account for the lateral transport of energy with varying densities).[28-30] The AXB algorithm is a nonanalytical model-based algorithm and represents the most recent generation of clinical dose calculation algorithms. It solves deterministically the coupled system of linear Boltzmann transport equations (LBTEs). It uses the same subsource models as implemented in the AAA, but in the patient dose calculation, the following steps are performed: 1) transport of source model fluence into the patient, 2) calculation of scattered photon fluence in the patient, 3) calculation of scattered electron fluence in the patient, and 4) dose calculation.[10] In heterogeneity correction, the AXB algorithm explicitly models the physical interactions of radiation with matter and, thus, the report mode for the final dose distribution is referred to as dose-to-medium in medium ($D_{m,m}$). Although the AXB algorithm inherently calculates $D_{m,m}$, the dose distributions can be converted to dose-to-water in medium ($D_{w,m}$), which is done by replacing the medium-based fluence-to-dose response function used in absorbed dose calculation with a water-based response function. In the PBC algorithm and in the AAA, the dose report mode is also $D_{w,m}$, but in those algorithms the dose results are based on electron density-based corrections applied to dose kernels calculated in water.[10-11,13] Therefore $D_{w,m}$ mode of the AXB algorithm represents more closely true absorbed dose to water.[12] For square fields in field sizes relevant to this study, the TPS algorithms produced dose distributions, compared to TPS beam data measurements, in water with dose differences less than 1.0% in percentage depth dose (PDD) curves at depths beyond depth of dose maximum (d_{max}), less than 0.7% in profiles in high-dose and out-of-field regions, and distance-to-agreement (DTA) values less than 1.8 mm in the penumbral region (results not presented in this paper).

B. The MC model

"Full" MC simulations were performed with the BEAMnrc code package (V4-2.3.1, or BEAMnrc 2010) based on the EGSnrc MC code that simulates coupled electron-photon transport. The EGSnrc-based phantom dose calculation is performed with DOSXYZnrc, also included in the BEAMnrc code package.[31] The geometry model of the linear accelerator (linac) treatment head was based on the Varian Clinac iX (2300C/D) linac equipped with Millennium 120 MLC (5 mm thick leaves at isocenter plane around beam central axis (CAX)). The MC model was based on the earlier work by the authors,[32] changing the treatment head components specific to the electron beam mode to ones specific to the photon beam mode used in this study.

The nominal photon beam energy was 6 MV. The simulation of beam generation and beam transport in the treatment head was divided into two phases to allow the absolute dose calibration of the MC model, following the technique by Popescu et al.[33] The initial electron beam of the MC model was selected to be of circular shape with a Gaussian intensity distribution of 0.6 mm FWHM. The initial electron beam energy spectrum at the X-ray target level was negatively skewed in shape, having a lower energy "tail", peaking to the energy of 5.9 MeV. Other perspectives of the iterative initial electron beam tuning process and beam parameter selection are discussed in Ojala et al.[34] For square fields in field sizes relevant to this study, the MC model produced dose distributions, compared to TPS beam data measurements, in water with dose differences less than 1.0% in PDD curves at depths beyond d_{max}, less than 0.5% in profiles in high-dose and out-of-field regions and DTA values less than 0.2 mm in the penumbral region (results not presented in this paper). In the first phase simulation directional bremsstrahlung splitting (DBS) was applied with a splitting factor of 1000. This simulation had to be performed only once, with the number of particle histories of 10×10^9. The resulting particle data were collected into a phase space file, which was used as source in the second phase simulation through beam-modifying components, for which the number of particle histories was the number of resulted particles in the phase space file recycled five times. The contribution from each treatment field was simulated separately, and the parameters representing field apertures defined by jaws and MLC were exported from the TPS and converted to the

form required by the MC code package. The following electron and photon transport cutoff parameters were used in all simulations, also in subsequent DOSXYZnrc simulations: ECUT = AE = 0.521 MeV and PCUT = AP = 0.01 MeV. The value for ECUT for MC represents the cutoff of total (rest + kinetic) energy of the electron and it was chosen to provide accurate secondary electron transport. The cutoff value for electron kinetic energy for the AXB algorithm was 0.500 MeV (1.011 MeV total energy), which is unmodifiable by the user. Other EGSnrc parameters were the same as in the earlier work by the authors.[32]

The phase space data from second phase simulation were used as input for dose calculations in the patient geometry, applying the DOSXYZnrc code. The CT-based patient phantom geometry was reconstructed from a set of three mm-thick CT slices, exported from TPS, with the CTCREATE code in DOSXYZnrc. The CT number-to-material and density conversion curve were defined using the RMI Gammex 467 Tissue Characterization Phantom (Middleton, WI, USA). The same conversion curve was used in Eclipse TPS. Four different materials (AIR521ICRU, LUNG521ICRU, ICRUTISSUE521ICRU, and ICRPBONE521ICRU) were assigned for patient phantom voxels using the conversion curve, and the PEGS4 cross-sectional data for the materials were applied in MC dose calculation. In the AXB algorithm, adipose and cartilage tissue were also included in the material assignment table, but since they were not available in PEGS4 cross-sectional library, the CT number range of ICRUTISSUE521ICRU was extended to the upper limit of LUNG521ICRU and lower limit of ICRPBONE521ICRU in the MC model. The number of particle histories used in each DOSXYZnrc simulation was the number of resulting particles from second phase simulation recycled five times. The calculation grid size for CT-based patient phantoms was 0.125 cm, which was equivalent to the calculation grid size applied with clinical dose calculation algorithms. With MC model, the dose report mode is $D_{m,m}$. The random nature of particle transport is expressed by determining statistical uncertainties for the calculated dose values for simulated particles and dose values within each voxel. The average latent variances in BEAMnrc simulations were typically about ± 0.1%, which were taken into account in the average statistical uncertainty of about 1.0% in voxels with doses values greater than 50% of the maximum dose in patient dose calculations performed with DOSXYZnrc. In general, the simulation parameter selection was performed without compromising the calculation accuracy, which led to long calculation times (several thousands of CPU hours per plan), which was the reason why the MC calculations were applied only to limited number of patients.

C. Patient selection, dose prescription, treatment planning, and comparison

The criteria for the patient selection were to include patients with varying PTV sizes and tumors not in contact with surrounding high-density structures (i.e., thoracic or mediastinal wall, diaphragm or large blood vessels). The distance of the gross tumor volume (GTV) to such structures was usually at least 1–2 cm, being at minimum 3 mm for small parts of some GTVs. Structures were delineated utilizing retrospective respiration-correlated 4D CT (Philips Brilliance Big Bore CT, Philips Healthcare System, Cleveland, OH, USA) technique, from which maximum intensity projection datasets with 3 mm slice thickness were reconstructed. The dose calculation was performed in the average intensity projection of 4D CT datasets. The dose prescription was according to the Nordic SBRT study group, adapted from the original work published by Lax et al.[1] In this dose prescription protocol, doses to central parts of the PTV are about 50% higher than that prescribed at the periphery of the PTV. The prescription isodose level should be 67% of the dose at normalization point, which normally is close to the isocenter and/or the center of mass of the PTV. The dose planning criteria are described more in detail in Lax et al.[1] The prescribed dose was from 45 to 54 Gy in 3 to 5 fractions, depending on the size of the PTV. The plans used 3D conformal radiotherapy (CRT) technique and included five to nine coplanar nonopposing treatment fields with 6 MV photon beams. MLCs were used in static mode and no wedges were applied.

For all the plans, we extracted clinically relevant, quantitative dose-volume histogram (DVH) parameters for the PTV ($D_{95\%}$, $D_{50\%}$, and $D_{5\%}$; percentage of the dose for which there is 95%/50%/5% volume coverage), for the ipsilateral lung with the GTV subtracted ($V_{30\%}$; percentage of the structure volume for which the percentage dose is 30% or less), and for the spinal cord (D_{max}; percentage maximum dose).[7] To quantify the low dose spillage in the lung around the PTV, the maximum dose at a distance of 2 cm from the PTV (D_{2cm}[%]) was determined.[7] All the parameters were adapted from RTOG 0915 protocol[7] and they were normalized to the prescribed dose. From DVH parameters, also a conformity index (CI)[35] was calculated. It describes how the PTV is encompassed by the prescription dose, but also takes into account how much high-dose levels are spilling to the surrounding normal tissue around PTV. CI is calculated as follows:

$$CI = \frac{V_{PTV67\%}}{V_{PTV}} \frac{V_{PTV67\%}}{V_T} \quad (1)$$

where $V_{PTV67\%}$ represents the volume of PTV receiving the prescription dose, V_{PTV} is the volume of PTV, and V_T is total volume receiving the prescription dose.

C.1 The AXB algorithm vs. the full MC model

In the first stage of the study, we selected four patients to cover the whole PTV size range from all the treated lung SBRT patients at the authors' clinic: a patient with a small PTV of 4.2 cc, two patients with medium-sized PTVs of 15.1 cc and 25.6 cc, and a patient with a large PTV of 100.4 cc. Using the selected patient CT datasets, the AXB algorithm was used for treatment planning (dose report mode: $D_{m,m}$), creating the plans to meet the planning criteria. The accuracy of the AXB algorithm was assessed by recalculating the plans with the MC model with the same number of monitor units (MUs) and identical field settings. The AXB-calculated plans, including the CT datasets, structure sets, and dose distributions, were exported to CERR software, where also the MC-calculated dose distributions were imported. CERR, which uses MATLAB software (The MathWorks, Natick, MA; version R2011b in this study), is a software package developed at Washington University for the review and analysis of mainly radiotherapy planning data.[36-37] In addition to DVH analysis including aforementioned DVH parameters, a 3D gamma analysis tool was applied to quantify the accuracy of the AXB algorithm. There were two levels of threshold criteria set for both parameters in the gamma analysis calculation: 2% (of maximum dose) in dose difference, 2 mm in distance-to-agreement (DTA) (2%/2 mm) and 3%/3 mm. To minimize the effect of inherent noise present in MC-based dose distributions on gamma analysis results, large numbers of particle histories were simulated in MC calculations to minimize the statistical uncertainty, and regions with less than 15% of maximum dose were neglected in the gamma analysis calculation. The results were presented with the gamma agreement index (GAI), which is the ratio of the number of calculation points passing the gamma test and the number of all calculation points.

C.2 The performance of the TPS algorithms

In the second stage of the study, a subgroup of ten patients (including four patients used in the AXB algorithm benchmark) was selected for this study. Separate plans applying both the PBC algorithm and the AAA for all patients were created to meet the planning criteria, keeping the number of fields and field directions similar but changing only the jaw and MLC apertures. Finally, the plans using the PBC algorithm and the AAA were recalculated with the same number of MUs and identical field settings with the AXB algorithm (dose report mode: $D_{w,m}$). The dose distributions were compared using the aforementioned DVH parameters, D_{2cm} and CI.

III. RESULTS

A. The AXB algorithm vs. the full MC model

The results for the 3D gamma analysis and for the DVH parameter comparison for the accuracy assessment of the AXB algorithm against the MC model are presented in Table 1. For the four plans, the GAI with the threshold criteria of 3%/3 mm was between 95.5% and 99.6%. The threshold criteria of 2%/2 mm revealed more differences. The largest discrepancy, 83.6%, was produced by the plan with the PTV of 15.1 cc. In DVH parameters, the largest discrepancies occurred in the plan with the same PTV; the difference in DVH parameters related to the PTV was at largest 11.9% in $D_{50\%}$. For all the plans, the discrepancies in the $V_{30\%}$ and spinal cord D_{max} parameters were small. The largest difference in the CIs was 0.13 for the plan with the PTV of 15.1 cc, while with the rest of the plans, the differences were negligible. The results for two plans with largest PTVs showed better overall congruence, as may also be seen in the GAI values. Differences less than 1% can be ignored, since the statistical uncertainties related to the MC-calculated dose distributions were of the same order.

Figure 1 presents isodose distribution (Fig. 1(a)) and positional distribution of the dose discrepancies (Fig. 1(b)) for the plan with the medium-sized PTV of 15.1 cc. In the dose difference graphs (Fig. 1(b)), dose values in the craniocaudal direction are nearly 11% larger with the MC model than with the AXB algorithm, located in the low-density areas in the lung around high-density tumor in the cranial and caudal corners of the PTV margin. In the transversal direction, the largest differences occur also in the PTV margin, but are half, about 5% of the difference in the other direction. In the central PTV, the dose values for the MC model are about 0% to 3% larger than for the AXB algorithm.

TABLE 1. Comparison of the results between the dose distributions from original AXB-calculated plans which were recalculated with the MC model. All DVH parameter results represent the difference values between the original AXB-calculated plan and the MC-recalculated AXB-plan. Absolute dose values for various DVH parameters from different plans are normalized to the prescribed dose values.

	Patient #1	*Patient #2*	*Patient #3*	*Patient #4*
PTV volume (cc)	4.2	15.1	25.6	100.4
GAI	*(%)*	*(%)*	*(%)*	*(%)*
3%/3 mm	98.9	95.5	99.4	99.6
2%/2 mm	92.6	83.6	94.4	95.2
Parameters		*Difference (%)*		
Lung				
D_{2cm}	3.3	-7.6	-2.7	-1.4
PTV				
$D_{95\%}$	-4.0	-11.1	-3.6	-1.8
$D_{50\%}$	-7.3	-11.9	-4.4	-1.8
$D_{5\%}$	-10.2	-9.4	-1.6	-0.2
Lung-GTV				
$V_{30\%}$	-0.6	-1.5	-0.5	-0.2
Spinal cord				
D_{max}	-0.2	0.0	1.3	1.0
CI (absolute diff.)	0.03	0.13	0.05	0.01

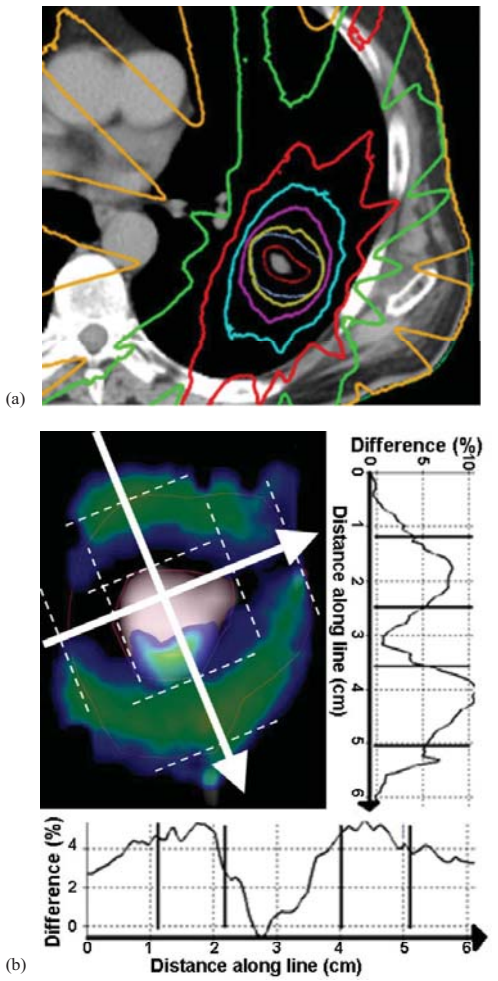

FIG. 1. The isodose distribution (a) calculated by the MC model for the plan with medium-sized PTV (15.1 cc) in transversal isocenter plane. Dose levels from the outermost isodose curve to the innermost one are 5 Gy, 15 Gy, 25 Gy, 35 Gy, 45 Gy (the prescription dose), and 55 Gy. The two innermost contours represent the PTV and the GTV, respectively. A sagittal isocenter plane (b) showing colored areas, where the gamma calculation typically failed (threshold criteria 3%/3 mm). The graphs along the lines show the percentage dose difference between the MC-recalculated AXB-plan and the original AXB-plan through the largest dose differences in orthogonal directions. Lines in the profiles represent the PTV and the GTV boundaries.

B. The performance of the TPS algorithms

The results of the TPS algorithm comparison are presented in Table 2 and in Figs. 2 to 5. Certain DVH parameters show large dosimetric uncertainties for the smallest PTV volumes. For DVH parameters related to the PTV ($D_{95\%}$, $D_{50\%}$, $D_{5\%}$) with both the PBC algorithm and the AAA the differences compared to AXB-recalculated dose distributions become larger with

TABLE 2. Comparison of the results between dose distributions from original PBC- and AAA-based plans, which were recalculated with the AXB algorithm. All DVH parameter results represent the difference values between the original AAA-calculated plan and the AXB-recalculated AAA plan or the original PBC-calculated plan and AXB-recalculated PBC plan. Absolute dose values for various DVH parameters from different plans are normalized to the prescribed dose values.

	Maximum Difference (%)		*Minimum Difference (%)*		*Mean Difference (%)*	
Parameters	*AAA*	*PBC*	*AAA*	*PBC*	*AAA*	*PBC*
Lung						
D_{2cm}	6.5	25.7	0.4	3.3	0.8	11.2
PTV						
$D_{95\%}$	18.3	44.1	0.2	4.4	5.0	20.5
$D_{50\%}$	19.1	58.3	0.2	7.8	3.9	25.3
$D_{5\%}$	8.0	44.3	0.2	4.8	1.4	18.9
Lung-GTV						
$V_{30\%}$	1.6	3.8	0.0	0.0	0.3	1.2
Spinal cord						
D_{max}	-1.4	3.1	0.0	0.0	0.1	0.4
CI (absolute diff.)	0.25	0.58	0.00	0.00	0.03	0.16

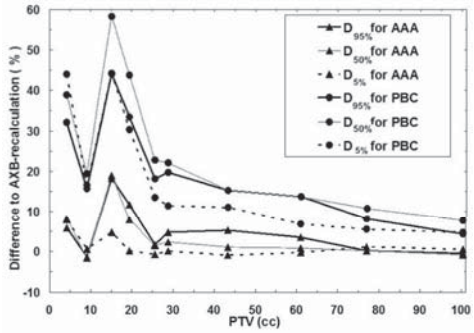

FIG. 2. Comparison of the results for the algorithms as a function of the PTV size. Lines with triangles represent the differences for $D_{95\%}$, $D_{50\%}$, and $D_{5\%}$ between the AAA and the AXB-recalculated AAA plan, and lines with circles represent the differences for $D_{95\%}$, $D_{50\%}$, and $D_{5\%}$ between the PBC algorithm and the AXB-recalculated PBC plan. Solid lines are for $D_{95\%}$, grey lines for $D_{50\%}$, and dashed lines for $D_{5\%}$.

the decreasing size of the PTV, which is also visualized in Fig. 2. Also, the PBC algorithm produces larger discrepancies than the AAA throughout the PTV size range. The largest discrepancies between the PBC and AXB algorithms, and the AAA and the AXB algorithms in $D_{50\%}$ are 58.3% and 19.1%, respectively, which both occur in a plan with the PTV size of 15.1 cc. The largest discrepancies are located in the cranial and caudal parts of the PTV margin, where the PBC algorithm and the AAA consistently produce larger dose values than present in the AXB-recalculated plans.

The parameter D_{2cm} showed also larger dose deviations for the small-sized PTVs, which is visualized in Fig. 3. The dose differences at a distance from the PTV are more pronounced with the smaller sized PTVs, while with the two smallest PTVs the discrepancies decrease. The largest discrepancies between the PBC and AXB algorithms and the AAA and the AXB algorithm were 25.7% and 6.5%, respectively, and they occurred in a plan with the PTV of 15.1 cc.

In the lung, the dose differences are smaller in general, when compared to discrepancies in the PTV-related DVH parameters and in D_{2cm}. Only in plans with smallest PTVs, the $V_{30\%}$

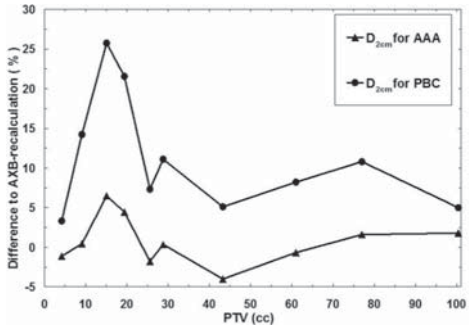

FIG. 3. Comparison of the results for the algorithms as a function of the PTV size. Solid line with triangles represents the difference in D_{2cm} between the AAA and the AXB-recalculated AAA plan, and solid line with circles represents the differences in D_{2cm} between the PBC algorithm and the AXB-recalculated PBC plan.

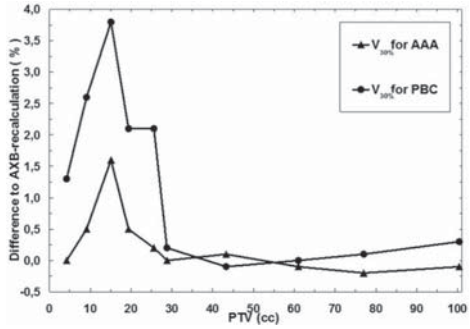

FIG. 4. Comparison of the results for the algorithms as a function of the PTV size. Solid line with triangles represents the difference in $V_{30\%}$ for the ipsilateral lung with the GTV subtracted between the AAA and the AXB-recalculated AAA plan, and solid line with circles represents the difference for the same DVH parameter between the PBC algorithm and the AXB-recalculated PBC plan.

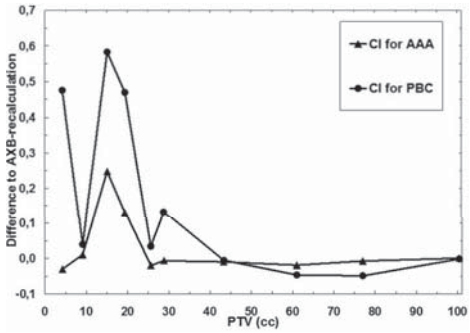

FIG. 5. Comparison of the results for the algorithms as a function of the PTV size. Solid line with triangles represents the difference in CI between the AAA and the AXB-recalculated AAA plan, and solid line with circles represents the differences for the CI between the PBC algorithm and the AXB-recalculated PBC plan. The reader should note the absolute scale used.

DVH parameter shows considerable dose differences, being maximally 3.8% with the PBC algorithm and about 1.6% with the AAA. The mean values for the differences with both algorithms were small, although slightly larger for the PBC algorithm. The differences for the $V_{30\%}$ are visualized in Fig. 4.

For the spinal cord, no dependence on the size of PTV was found and the maximum and mean values for the differences were comparable to the results for the $V_{30\%}$ parameter, with the maximum difference for the PBC algorithm being 3.1% and 1.4% for the AAA, while the mean differences were negligible.

The achieved values for CI for different plans in this study ranged from 0.60 to 0.80, values closer to 0.60 for the plans with small PTVs and values closer to 0.80 for the plans with large PTVs (not shown). The differences in CI (Fig. 5) show similar behavior as a function of the size of the PTV, as do DVH parameters for the PTV, $V_{30\%}$ and D_{2cm}. With the PBC algorithm, the largest absolute differences are more than twice larger than with the AAA and with both the differences increase with decreasing size of the PTV in the plan. The relative discrepancies are drastic, especially for the PBC algorithm, for which the value for CI was nearly thirteenfold (0.63 vs. 0.05) that obtained for the AXB-recalculated PBC-plan in the plan with PTV size of 15.1 cc. For this plan, the CI for the AAA was only 1.5-fold (0.70 vs. 0.46), when compared to the AXB-recalculated AAA-plan.

The computation times for all the plans were in the range from 24 sec to 30 sec, 29 sec to 43 sec and 3 min 57 sec to 4 min 13 sec for the PBC algorithm, the AAA, and the AXB algorithm, respectively. In the calculations, the distributed calculation framework (DCF) of the Eclipse TPS was used. In each calculation, the DCF distributed one field per calculation node. In the AXB algorithm calculations, "the field dose" option was selected.

IV. DISCUSSION

A. The AXB algorithm vs. the full MC model

The results for the comparison between the AXB algorithm and the full MC model indicate that the AXB algorithm can be used as a baseline for the other two TPS algorithms with reserve. In gamma analysis applied to plan verification, which is usually performed in 2D, the threshold criteria is very often set to 3%/3 mm, which is also recommended by the American Association of Physicists in Medicine (AAPM) Task Group Report TG-119[38] for the quality assurance of intensity-modulated radiotherapy (IMRT) that contains fields with large dose gradients produced by small field segments. In this study, the gamma analysis with aforementioned threshold criteria was performed in 3D, for which the achieved agreement levels of higher than 95.5% for all four plans suggests that the differences between the AXB algorithm and the MC model are clinically acceptable. The more stringent threshold criteria of 2%/2 mm reveals differences increasing in an expected manner (i.e., with the decreasing size of the PTV) and especially for the plan with the PTV of 15.1 cc, for which the largest discrepancies occurred also between the TPS algorithms.

In the DVH parameters, the differences between the AXB algorithm and the MC model showed the largest discrepancies in the dose calculation for the mean ($D_{50\%}$) and near minimum ($D_{95\%}$) dose values of the PTV, except for the plan with the smallest PTV, for which the largest discrepancy occurred in areas of near maximum doses ($D_{5\%}$). The largest differences occurring in the $D_{50\%}$ and $D_{95\%}$ parameters imply that the discrepancies occur in the PTV margin, which is demonstrated in Fig. 1(b). With decreasing PTV size, the proportion of the margin volume increases relative to the total PTV volume and, therefore, these discrepancies become larger in plans with decreasing PTV size. In addition to inherent sources of systematic error in the AXB algorithm due to discretization of solution variables, as described in Failla et al.,[10] a presumable explanation for aforementioned differences is the considerably higher electron transport energy cutoff value used in the AXB algorithm (1.011 MeV) compared to the value

used with the MC model (0.521 MeV). This leads to the lower dose values in the PTV margin towards the periphery of the PTV in the AXB-calculated dose distributions. The difference is largest near the field edge and the contributions from the fields accumulate to the same part of the PTV margin in the cranial and caudal ends of the PTV. In the other parts of the PTV margin the difference is partially compensated by central parts of the other fields.

Contribution for the difference may also arise from how different materials are assigned in the AXB algorithm and in the MC model calculations in this study. The density of the material in the PTV margin is less than unity, falling steeply to density ranges of adipose and lung tissues. In the AXB algorithm, the upper limit of the density range of the adipose tissue extends nearly to unity, contrary to the MC model calculations. With the MC model, the adipose tissue is replaced by extending the density range of the skeletal muscle (ICRUTISSUE521ICRU) down to the upper limit of the lung tissue, which is the same as in the AXB algorithm. In the plan with the smallest PTV, the HU values of the GTV in the average intensity projection CT dataset fall into range of the adipose and the lung tissue limit, which is due to the blurred HU values of the very small tumor moving with respiration. This is contrary to the much higher density GTVs in the centers of PTVs in the other plans. The increased contribution of differences in material assignments between the calculations, alongside the different cutoff energies, might be the reason for the largest discrepancy occurring in the areas of highest doses ($D_{5\%}$) in the plan with the smallest PTV.

B. The performance of the TPS algorithms

In plan comparison assessing the accuracy of the AXB algorithm using the MC model, the dose report mode was $D_{m,m}$, which is an inherent default option for both calculation methods. This was the motive to perform the comparison using $D_{m,m}$ mode, whereas, in TPS algorithm comparison, the dose report mode $D_{w,m}$ of the AXB algorithm was used to allow the mutual comparison of the AXB algorithm to the AAA and the PBC algorithm. Since the purpose of this study was to assess the performance and reveal discrepancies between different algorithms in clinical practice, setting the dose report mode to the same was a natural choice for a fair comparison. The accuracy of the AXB algorithm in heterogeneous media using both dose report modes in other contexts than SBRT has been assessed.[12-15]

The comparison between the TPS algorithms showed levels of discrepancies that are likely to influence the treatment outcomes. According to Report of AAPM Task Group No. 105, dose differences as low as 5%–10% are reported to be clinically detectable, and may result in 10%–20% changes in tumor control probability or 20%–30% changes in normal tissue complication probability.[17] For the PTV, the DVH parameters differed nearly 60% between the PBC algorithm and the AXB algorithm for the plan with the most central PTV of 15.1 cc with a distance of at least 2 cm from the surrounding high-density structures. The overall performance of the PBC algorithm decreased considerably when the sizes of the PTVs fell below 25 cc. The differences from the AXB-recalculated dose distributions were larger than 5% for the whole PTV size range. The AAA showed discrepancies less than 5% for the PTV size range down to 25 cc, being maximally less than 20% for the plan with the most central PTV of 15.1 cc. From the viewpoint of tumor control, the results indicate the known fact that the PBC algorithm should not be used in the clinical dose calculation for the lung SBRT. The discrepancies between the AAA and the AXB algorithm with plans having PTVs smaller than 20–25 cc, in connection with discrepancies between the MC model and the AXB algorithm, imply that the plans need further verification prior to treatment (e.g., against full MC dose calculation and/or measurements).

For the D_{2cm} parameter characterizing the dose spillage to the surroundings of the PTV, both the PBC algorithm and the AAA perform better than with the DVH parameters related to the PTV, although the maximum discrepancies still are at an unacceptable level. The mean deviation of D_{2cm} was 11.2% for the PBC algorithm and only 0.8% for the AAA, indicating that the heterogeneity correction applied in the AAA is able to predict the dose much more

accurately than the PBC algorithm. For the $V_{30\%}$ parameter, the maximum differences were 3.8% and 1.6%, and mean differences were 1.2% and 0.3%, for the PBC algorithm and the AAA, respectively. The reason for these relatively small discrepancies is that the volume of the healthy lung tissue through which the beams travel is small compared to the volume of the whole lung. The discrepancies for the spinal cord were even smaller, which is because the absolute dose levels in spinal cord were very low, since it is avoided in the treatment planning. The last parameter describing the discrepancies between different algorithms was CI, which combines the PTV coverage and the dose spillage to the surroundings of the PTV. The CI is a step to a more clinically-relevant quality parameter for plan comparison purposes, especially applicable to SBRT, where extremely high conformality with high-dose gradients and minimal coverage in the healthy tissue is sought. The results revealed how large differences may occur in lung SBRT with small-size PTVs between dose calculation algorithms from three generations and attests also to the applicability of the CI to represent a sensitive quality parameter for SBRT plan comparison.

The intention of this study was to choose plans with tumors not in contact with the surrounding high-density anatomical structures to minimize the contribution of scattered radiation from these structures to dose distributions and, thus, to enable a fair comparison between the plans. Regardless of that, we noticed that the differences in the DVH parameters are sensitive to the anatomical location of the PTV. Varying distances of higher density tissues affected the quantitative DVH parameter values of the PTVs insomuch that the dependence of the calculation differences on the size of PTV was compromised. An example of this behavior can be seen with the PTV of 9.1 cc (Figs, 2 and 5), where the PTV locates centrally in the lung, but the distance to the posterior thoracic wall and to the caudal end of the lung are small. As a consequence, the discrepancies for both the PBC algorithm and the AAA are notably smaller than those of the other plans in the same PTV size range. On the contrary, in the plan with the PTV of 15.1 cc, for which the largest deviations occurred, the PTV was located the most centrally of all the studied patient cases and additional difficulty for the dose calculation was introduced by the complex-shaped bronchus located partially inside the PTV. As a conclusion, it is difficult to find an explicit relation for the location of a PTV. The similar behavior of the parameters can also be seen in a comprehensive comparison for the type ‘a’ and type ‘b’ algorithms by Hurkmans et al.[8] The results in this study represent mostly the worst case scenario of the discrepancies between the algorithms concerning small targets locating centrally in the lung.

The purpose of this study was not to show the inapplicability of the PBC and other type ‘a’ algorithms for lung SBRT dose calculation, which has been shown by numerous research groups and discouraged by the most recent clinical trial and protocol reports.[6-8] The intention was firstly to produce dosimetric data for the radiotherapy community to transfer dose prescription and normal tissue tolerance protocols based on type ‘a’ algorithm calculations for type ‘b’ dose calculation algorithms, such as the AAA, and secondly, to aid the community further in converting the SBRT protocols for the most recent type ‘c’ algorithm. This study also demonstrates that, until general conclusions on the improved accuracy of a new dose calculation algorithm over previous generation algorithms can be drawn, extensive benchmarking also with clinical patient datasets including various anatomical sites and treatment techniques has to be performed, albeit other studies using homogeneous and heterogeneous virtual phantoms have shown excellent results. In the light of this study, further development is needed to achieve even better congruence between the AXB algorithm and the MC model. This requires an access to the most recent version of the AXB algorithm (version 11), where enhancements to the low-energy electron transport and low-density material assignment have been incorporated.[14] We aim to extend the scope of our investigation to MC-based VMAT SBRT.

V. CONCLUSIONS

The accuracy of a type 'c', the AXB algorithm, in dose report mode $D_{m,m}$, was assessed against full MC simulations for clinical lung SBRT plans with varying sized centrally located PTVs. We observed high level of agreement, especially with 3D gamma analysis. The AXB algorithm, in dose report mode $D_{w,m}$, was used as the baseline in TPS algorithm comparison against a type 'a', the PBC algorithm, and a type 'b' algorithm, the AAA. The results showed large discrepancies for the PBC algorithm and notable differences between the AAA and the AXB algorithm, especially for plans with small PTVs. Some results even implied that the AAA produced dose distributions closer to the MC model than the AXB algorithm. This work encourages the application of further plan verification methods, such as full MC dose calculation and/or measurements, when the AAA or the AXB algorithm are used in lung SBRT having PTVs smaller than 20–25 cc. Also more comprehensive benchmarking of the version 10.0.28 of the AXB algorithm is needed prior to clinical commissioning. However, the calculated data from this study, in addition to further contribution from scientific community in the form of similar studies, can be used in converting the SBRT protocols based on type 'a' and/or type 'b' algorithms for the most recent generation type 'c' algorithms, such as the AXB algorithm.

ACKNOWLEDGMENTS

This study was financially supported by the legacy (allotted to the development of cancer treatment) of Seppo Nieminen.

REFERENCES

1. Lax I, Blomgren H, Näslund I, Svanström R. Stereotactic radiotherapy of malignancies in the abdomen. Methodological aspects. Acta Oncol. 1994;33(6):677–83.
2. Chang BK and Timmerman RD. Stereotactic body radiation therapy: a comprehensive review. Am J Clin Oncol. 2007;30(6):637–44.
3. Taylor ML, Kron T, Franich RD. A contemporary review of stereotactic radiotherapy: Inherent dosimetric complexities and the potential for detriment. Acta Oncol. 2011;50(4):483–508.
4. Timmerman RD, Galvin J, Michalski J, et al. A phase II trial of stereotactic body radiation therapy (SBRT) in the treatment of patients with medically inoperable stage I/II non-small cell lung cancer. RTOG 0236. Philadelphia, PA: RTOG; 2009.
5. Timmerman RD, Galvin J, Edelman MJ, et al. A Phase II Trial of Stereotactic Body Radiation Therapy (SBRT) in the Treatment of Patients with Operable Stage I/II Non-Small Cell Lung Cancer. RTOG 0618. Philadelphia, PA: RTOG; 2012.
6. Bezjak A, Papiez L, Bradley J et al. Seamless Phase I/II Study of Stereotactic Lung Radiotherapy (SBRT) for Early Stage, Centrally Located, Non-Small Cell Lung Cancer (NSCLC) in Medically Inoperable Patients. RTOG 0813. Philadelphia, PA: RTOG; 2012.
7. Videtic GMM, Singh AK, Parker W, et al. A randomized phase II study comparing 2 stereotactic body radiation therapy (SBRT) schedules for medically inoperable patients with stage I peripheral non-small cell lung cancer. RTOG 0915. Philadelphia, PA: RTOG; 2012.
8. Hurkmans CW, Cuijpers JP, Lagerwaard FJ, et al. Recommendations for implementing stereotactic radiotherapy in peripheral stage IA non-small cell lung cancer: report from the Quality Assurance Working Party of the randomised phase III ROSEL study. Radiat Oncol. 2009;4:1.
9. Benedict SH, Yenice KM, Followill D, et al. Stereotactic body radiation therapy: the report of AAPM Task Group 101. Med Phys. 2010;37(8):4078–101.
10. Failla GA, Wareing T, Archambault Y, Thompson S. Acuros XB advanced dose calculation for the Eclipse treatment planning system. Palo Alto, CA: Varian Medical Systems; 2010.
11. Vassiliev ON, Wareing TA, McGhee J, Failla G, Salehpour MR, Mourtada F. Validation of a new grid-based Boltzmann equation solver for dose calculation in radiotherapy with photon beams. Phys Med Biol. 2010;55(3):581–98.
12. Bush K, Gagne IM, Zavgorodni S, Ansbacher W, Beckham W. Dosimetric validation of Acuros XB with Monte Carlo methods for photon dose calculations. Med Phys. 2011;38(4):2208–21.
13. Han T, Mikell JK, Salehpour M, Mourtada F. Dosimetric comparison of Acuros XB deterministic radiation transport method with Monte Carlo and model-based convolution methods in heterogeneous media. Med Phys. 2011;38(5):2651–64.

14. Fogliata A, Nicolini G, Clivio A, Vanetti E, Cozzi L. Dosimetric evaluation of Acuros XB Advanced Dose Calculation algorithm in heterogeneous media. Radiat Oncol. 2011;6:82.
15. Han T, Mourtada F, Kisling K, Mikell J, Followill D, Howell R. Experimental validation of deterministic Acuros XB algorithm for IMRT and VMAT dose calculations with the Radiological Physics Center's head and neck phantom. Med Phys. 2012;39(4):2193–202.
16. Rana S, Rogers K, Lee T, Reed D, Biggs C. Verification and dosimetric impact of Acuros XB algorithm for stereotactic body radiation therapy (SBRT) and RapidArc planning for non-small-cell lung cancer (NSCLC) patients. Int J Med Phys Clin Eng Radiat Oncol. 2013;2:6–14.
17. Chetty IJ, Curran B, Cygler JE, et al. Report of the AAPM Task Group 105: Issues associated with clinical implementation of Monte Carlo-based photon and electron external beam treatment planning. Med Phys. 2007;34(12):4818–53.
18. Ding GX, Duggan DM, Lu B, et al. Impact of inhomogeneity corrections on dose coverage in the treatment of lung cancer using stereotactic body radiation therapy. Med Phys. 2007;34(7):2985–94.
19. Moiseenko V, Liu M, Bergman AM, et al. Monte Carlo calculation of dose distribution in early stage NSCLC patients planned for accelerated hypofractionated radiation therapy in the NCIC-BR25 protocol. Phys Med Biol. 2010;55(3):723–33.
20. Haedinger U, Krieger T, Flentje M, Wulf J. Influence of calculation model on dose distribution in stereotactic radiotherapy for pulmonary targets. Int J Radiat Oncol Biol Phys. 2005;61(1):239–49.
21. Fragoso M, Wen N, Kumar S, et al. Dosimetric verification and clinical evaluation of a new commercially available Monte Carlo-based dose algorithm for application in stereotactic body radiation therapy (SBRT) treatment planning. Phys Med Biol. 2010;55(16):4445–64.
22. Chen H, Lohr F, Fritz P, et al. Stereotactic, single-dose irradiation of lung tumors: a comparison of absolute dose and dose distribution between pencil beam and Monte Carlo algorithms based on actual patient CT scans. Int J Radiat Oncol Biol Phys. 2010;78(3):955–63.
23. Li J, Galvin J, Harrison A, Timmerman R, Yu Y, Xiao Y. Dosimetric verification using Monte Carlo calculations for tissue heterogeneity-corrected conformal treatment plans following RTOG 0813 dosimetric criteria for lung cancer stereotactic body radiotherapy. Int J Radiat Oncol Biol Phys. 2012;84(2):508–13.
24. Dieterich S and Sherouse GW. Experimental comparison of seven commercial dosimetry diodes for measurement of stereotactic radiosurgery cone factors. Med Phys. 2011;38(7):4166–73.
25. Storchi P and Woudstra E. Calculation of the absorbed dose distribution due to irregularly shaped photon beams using pencil beam kernels derived from basic beam data. Phys Med Biol. 1996;41(4):637–56.
26. Storchi PR, van Battum LJ, Woudstra E. Calculation of a pencil beam kernel from measured photon beam data. Phys Med Biol. 1999;44(12):2917–28.
27. Webb S and Fox RA. Verification by Monte Carlo methods of a power law tissue-air ratio algorithm for inhomogeneity corrections in photon beam dose calculations. Phys Med Biol. 1980;25(2):225–40.
28. Ulmer W and Harder D. A triple Gaussian pencil beam model for photon beam treatment planning. Z Med Phys. 1995;5:25–30.
29. Ulmer W and Harder D. Applications of a triple Gaussian pencil beam model for photon beam treatment planning. Z Med Phys. 1996;6:68–74.
30. Ulmer W, Pyyry J, Kaissl W. A 3D photon superposition/convolution algorithm and its foundation on results of Monte Carlo calculations. Phys Med Biol. 2005;50(8):1767–90.
31. Rogers DW, Faddegon BA, Ding GX, Ma CM, We J, Mackie TR. BEAM: a Monte Carlo code to simulate radiotherapy treatment units. Med Phys. 1995;22(5):503–24.
32. Ojala J, Hyödynmaa S, Barańczyk R, Góra E, Waligórski M. Performance of two commercial electron beam algorithms over regions close to the lung-mediastinum interface, against Monte Carlo simulation and point dosimetry in virtual and anthropomorphic phantoms. Phys Med. 2013. [E-pub ahead of print]
33. Popescu IA, Shaw CP, Zavgorodni SF, Beckham WA. Absolute dose calculations for Monte Carlo simulations of radiotherapy beams. Phys Med Biol. 2005;50(14):3375–92.
34. Ojala J, Hyödynmaa S, Pitkänen M. BEAMnrc Monte Carlo modelling of linear accelerator using parallel computing grid — validation of a common, fixed geometry model for photon and electron beams. Proceedings of XVIth ICCR. Amsterdam, The Netherlands; ICCR; 2010.
35. van't Riet A, Mak ACA, Moerland MA, Elders LH, van der Zee W. A conformation number to quantify the degree of conformality in brachytherapy and external beam irradiation: application to the prostate. Int J Radiat Oncol Biol Phys. 1997;37(3):731–36.
36. Deasy JO, Blanco AI, Clark VH. CERR: a computational environment for radiotherapy research. Med Phys. 2003;30(5):979–85.
37. Spezi E, Lewis DG, Smith CW. A DICOM-RT-based toolbox for the evaluation and verification of radiotherapy plans. Phys Med Biol. 2002;47(23):4223–32.
38. Ezzell GA, Burmeister JW, Dogan N, et al. IMRT commissioning: multiple institution planning and dosimetry comparisons, a report from AAPM Task Group 119. Med Phys. 2009;36(11):5369–73.

Publication III

Ojala, J., Kapanen, M., Sipilä, P., Hyödynmaa, S., Pitkänen, M.

The accuracy of Acuros XB algorithm for radiation beams traversing a metallic hip implant – comparison with measurements and Monte Carlo calculations.

ACCEPTED FOR PUBLICATION
to J Appl Clin Med Phys on 1 May 2014.

Publication IV

Ojala, J., Hyödynmaa, S., Barańczyk, R., Góra, E., Waligórski, M.P.R.

Performance of two commercial electron beam algorithms over regions close to the lung-mediastinum interface, against Monte Carlo simulation and point dosimetry in virtual and anthropomorphic phantoms.

Phys Med, 30(2014)2, pp. 147-54.

Performance of two commercial electron beam algorithms over regions close to the lung-mediastinum interface, against Monte Carlo simulation and point dosimetry in virtual and anthropomorphic phantoms

J Ojala[1,2], S Hyödynmaa[1,2,3], R Barańczyk[4], E Góra[5] and M P R Waligórski[5,6]

[1] Department of Oncology, Unit of Radiotherapy, Tampere University Hospital, P.O. Box 2000, FI-33521 Tampere, Finland
[2] Department of Biomedical Engineering, Tampere University of Technology, P.O. Box 527, FI-33101 Tampere, Finland
[3] Department of Medical Physics, Medical Imaging Center, Tampere University Hospital, P.O. Box 2000, FI-33521 Tampere, Finland
[4] Radiation Protection Unit, Directorate-General for Energy, European Commission, L-2920 Luxembourg
[5] Centre of Oncology, Kraków Division, ul. Garncarska 11, 31-115 Kraków, Poland
[6] Institute of Nuclear Physics, Polish Academy of Sciences, ul. Radzikowskiego 152, 31-342 Kraków, Poland

E-mail: jarkko.ojala@pshp.fi

Abstract. Electron radiotherapy beams are applied to treat the chest wall close to the mediastinum. We investigated the performance of a commercial treatment planning system (TPS) in this region. The calculation accuracy of the GGPB and eMC algorithms implemented in the Varian Eclipse™ TPS were studied for 9 and 16 MeV electron beams, against BEAMnrc Monte Carlo (MC) code simulations, point dosimetry in a water phantom and dose distributions calculated in virtual phantoms. For the 16 MeV electron beam, the accuracy of these algorithms was also compared over the lung-mediastinum interface region of an anthropomorphic phantom, against MC calculations and thermoluminescence dosimetry (TLD). In the phantom with a slab of lung-equivalent material the results of all calculations were generally congruent, the eMC results for the 9 MeV beam slightly overestimating the lung dose, and the GGPB results for the 16 MeV beam underestimating the lung dose. Over the simulated lung-mediastinum interface, for 9 and 16 MeV beams, the GGPB code underestimated the lung dose and overestimated the dose in water close to the lung, compared to the congruent eMC and MC results. In the anthropomorphic phantom, results of TLD measurements and MC and eMC calculations agreed, while the GGPB code underestimated the lung dose. Good agreement between TLD measurements and MC calculations in the anthropomorphic phantom attests to the accuracy of "full" MC simulations as a reference for benchmarking codes used in commercial TPSs. Application of the GGPB code in chest wall electron beam therapy planning may result in significant underestimation of dose to the lung and overestimation of dose to the mediastinum, affecting therapy plan optimization over volumes close to the lung-mediastinum interface, such as the lung or heart.

Performance of two electron beam algorithms in chest wall radiotherapy

1. Introduction

Electron beams can be applied in external beam radiotherapy to treat tumour volumes adjacent to the skin or at shallow depths, to best exploit the depth-dose characteristics of such beams [1]. In modern treatment planning systems (TPSs) most of the algorithms used to calculate dose distributions from electron beams are based either on pencil beam or on Monte Carlo (MC) principles. The pencil beam algorithms used most frequently are the Generalized Gaussian Pencil Beam (GGPB) [2], the Gaussian Pencil Beam [3] and the Redefinition pencil beam algorithms [4]. In MC algorithms of commercial TPSs several techniques are used to speed up their calculations. In the Macro Monte Carlo (MMC) algorithm, pre-calculated small volume elements [5][6] are applied. The voxel Monte Carlo algorithm [7][8] uses a collection of variance reduction techniques and different approximations in modelling various interaction processes. When tested against measurements in homogeneous phantoms at standard source-to-surface distances (SSD), the accuracy of most of these algorithms is satisfactory. However, MC-based algorithms are reported to show better accuracy in more complex heterogeneous geometries. [1][9][10][11]

The accuracy of electron beam dose calculation algorithms used in commercial TPSs has been tested against measurements and results of "full" MC calculations in small air cavities, small bone prisms, local outer contour variations (step, nose contour, etc.), the tracheal cavity, or the vertebrae [11][12][13][14][15]. Photon beam intensity-modulated radiotherapy has by now widely replaced electron beams in the clinical treatment of such sites, yet in treating the chest wall (post-mastectomy or intact chest) application of electron beams may still offer a clinical advantage. The accuracy of TPS electron beam algorithms over adjacent lung volumes has been tested, but mainly for slab-like geometries [16][17][18]. To compare the heart and lung doses associated with chest wall irradiation of patients undergoing electron beam boost therapy, Coleman et al. [19] validated an implementation of the pencil beam principle (Fermi-Eyges-Hogstrom-algorithm) against an MC calculation in chest wall treatment of an anthropomorphic phantom by a 12 MeV electron beam. In treatment of the thoracic section of an anthropomorphic phantom using a 16 MeV electron beam, Waligorski et al. [17] compared the accuracy of two electron pencil beam algorithms against thermoluminescence dosimetry (TLD). In another more recent study, Aubry et al. [20] compared calculation results of the Varian TPS implementation of the MMC algorithm (eMC) for electron beams of energies ranging between 6 and 18 MeV in slab-like geometry and anthropomorphic lung-mediastinum interface geometries, against an MC computation and film measurements. During the past decade, advanced MC codes, especially EGSnrc/BEAMnrc, MCNP and PENELOPE, have established their applicability in quality assurance (QA) and benchmarking calculations in radiotherapy [9][10]. Offering "full" MC simulations, these codes are now able to deliver reference-quality three-dimensional (3D) dose distributions in complex heterogeneous geometries.

In this work we studied the calculation accuracy of the GGPB algorithm (based on the pencil beam principle) and of the eMC algorithm (based on the MMC principle), implemented in the Varian Eclipse™ TPS. Both algorithms were applied to treat the region of the chest wall and lung close to the mediastinum (in non-slab geometry), using 20x20 cm^2 fields of 9 or 16 MeV electron beams. We first calculated dose distributions in a homogeneous water-equivalent phantom and in a slab phantom with water- and lung-equivalent materials. Results of these calculations were compared against results of a simulation using the BEAMnrc MC code package, and validated against measurements in a water phantom with an ionization chamber (IC) and using radiochromic film. Next, we compared results obtained in a heterogeneous water-equivalent phantom in which a semi-infinite lung-equivalent slab was immersed to represent the lung-mediastinum boundary, covering half of the area perpendicular to the beam axis and extending from the edge of the phantom to the beam central axis (CAX). Finally, both electron beam algorithms were applied to calculate clinically relevant dose distributions from a 15x15 cm^2 field of a 16 MeV electron beam in a CT-based anthropomorphic phantom, for comparison against results of a BEAMnrc MC reference calculation and against in-phantom TLD measurements. The differences between calculated and measured dose values were then analysed to assess the performance, in terms of accuracy, of the tested TPS algorithms applied to calculate electron beam dose distributions over areas close to the lung-mediastinum interface.

2. Materials and Methods

2.1. Electron beam dose calculation algorithms

The tested algorithms, GGPB (version 8.6.15) and eMC (version 8.6.15), are implemented in the Eclipse™ 8.6 TPS by Varian Medical Systems, Inc. (Palo Alto, California, USA). Commissioning of the respective algorithms was performed according to manufacturer's manuals, using the same measurement data where applicable. The analytical GGPB algorithm is based on the Fermi-Eyges electron multiple scattering theory. The uncertainty of the GGPB algorithm can be estimated to be 1% in water-equivalent medium and 3% in large heterogeneous volumes, such as the lung [16]. The eMC algorithm, a Varian specific implementation of MMC in Eclipse™ TPS, utilizes a large library of pre-calculated kernels using accurate MC simulations for spherical volumes of varying sizes, materials and energies. The kernels are then used in the MC simulation within the global CT-based patient geometry and the dose calculation is performed with an adaptive step-size algorithm [5].

The nominal energies of the electron beams used in this study were 9 MeV ($\bar{E}_0$ = 8.4 MeV, $E_{p,0}$ = 8.8 MeV, R_p = 4.3 cm) and 16 MeV ($\bar{E}_0$ = 15.6 MeV, $E_{p,0}$ = 16.4 MeV, R_p = 8.1 cm), where $\bar{E}_0$ is the mean energy at the phantom surface, $E_{p,0}$ is the most probable energy at the phantom surface and R_p is the extrapolated range of the electron beam [21]. The SSD was 100 cm. Application of 9 MeV electron beams is typical for treating the post-mastectomy chest wall, while beams of higher energy (up to 16 MeV) are often applied in boost therapy of conservatively operated breast cancer. The calculation grid sizes for GGPB and eMC codes for 9 MeV were 1.5 and 1.25 mm (closest matching calculation grid size with small voxel dimensions), respectively, and 2.5 mm for 16 MeV, in both algorithms. The larger grid was selected for 16 MeV beam in order to use identical grids in both algorithms and because over less steep gradients larger calculation voxels could be used. The eMC algorithm contains several options. The following options were selected for this study: *Accuracy* = 1% (average statistical uncertainty in the high dose region); *Maximum number of particle histories* = 0 (automatically determined to reach *Accuracy*); *Smoothing method* = No smoothing [22]. As reported by Ding et al. [12] or Popple et al. [22], results of eMC calculations may strongly depend on the selection of calculation parameters, such as, e.g. , the size of the calculation grid, accuracy, or smoothing.

A homogeneous water-equivalent phantom (P1) was first created within the Eclipse™ TPS, and a comparison was made of dose distributions calculated for 9 and 16 MeV electron beams using the two algorithms. The electron applicator size was A20, producing a 20x20 cm^2 field at 100 cm SSD. Percent depth-dose (PDD) curves along the CAX, calculated for each energy, were compared.

Next, a virtual heterogeneous water-equivalent phantom (P2) was created, containing a slab of lung-equivalent material (mass density 0.32 g cm^{-3}, equal to the mass density of lung material in the anthropomorphic Rando-Alderson™ phantom). For 9 MeV beam calculations a lung-equivalent slab of 17 cm thickness was inserted at a depth of 3 cm, where the water-equivalent thickness of 3 cm represents a 1 cm thick water-equivalent bolus to increase the surface dose to 90%, and a post-mastectomy chest wall of 2 cm water-equivalent thickness. For 16 MeV beam calculations, the slab was placed at a depth of 4.5 cm (representing a water-equivalent bolus of 0.5 cm thickness to increase the surface dose to 95%, and a chest wall of 4 cm water-equivalent thickness). The effect of the ribs with mass density and atomic composition of bone was included in the water-equivalent chest wall thickness, as heterogeneities in the dose distribution due to the rib structure, prominent just below the ribs, are markedly reduced at the depths of interest in this study [18][23]. The total thickness of the P2 phantom was therefore equal to 20 or 21.5 cm, for the 9 and 16 MeV electron beam calculations, respectively. Again, the A20 electron beam applicator was used in these calculations.

At the third stage, calculations using the two TPS electron beam algorithms were performed in yet another phantom geometry (P3) with the slab of lung-equivalent material (mass density 0.32 g cm^{-3}) immersed at depths of 3 cm (for the 9 MeV beam) or 4.5 cm (for the 16 MeV beam), covering half of the area perpendicular to the beam axis. As shown in figure 1, the slab extended from the edge of the phantom to the CAX, and the lung-water interface was parallel to the beam axis. The A20 electron applicator, previously used in the P1- and P2-calculations, was also applied here. Two cross-plane profiles through the CAX, at depths where largest differences between the two TPS electron beam algorithms occur, were chosen for comparison.

FIGURE 1

Finally, dose distributions over the anterior chest wall of a heterogeneous anthropomorphic Rando-Alderson™ phantom (P4) treated by a 16 MeV electron beam with an A15 electron applicator, were calculated using the two TPS electron beam algorithms and the "full" MC model (see below). Results of these calculations were compared against TLD-measured values of absorbed dose at selected positions inside the lung and mediastinum areas of the anthropomorphic phantom. The anthropomorphic phantom geometry used in the calculations and the positions of TLD detectors were reconstructed from a set of 3 mm thick CT slices of the phantom, at 3 mm slice spacing.

2.2. The BEAMnrc MC code package

"Full" MC model simulations were performed using the BEAMnrc code package (version V4-2.3.1, or BEAMnrc 2010) based on the EGSnrc MC code which simulates coupled electron-photon transport. The EGSnrc-based phantom dose calculation is performed with DOSXYZnrc, also included in the BEAMnrc code package. This code package was installed on the calculation grid of the Tampere Centre for Scientific Computing (TCSC) at the Tampere University of Technology (TUT). The grid consists of 360 cores [24].

The geometry model of the linear accelerator treatment head was based on the Varian Clinac® 2100C/D medical linear accelerator. The manufacturer provided the authors with a confidential proprietary "Monte Carlo Data Package: High Energy Accelerator (2009)" containing information on parameters describing the geometry and materials, required in the modelling process [25]. The model included the primary collimator, the vacuum exit window, dual scattering foils, dual ionization chambers, the field mirror with its frame surrounded by the lead shielding plate, jaws, the fully retracted multileaf collimator, the light field reticle, the accessory mount and the electron applicator with a square cutout. Most of the geometry data were implemented from the manufacturer's data package, but readily accessible treatment head components were also re-measured with a caliper. In addition to the default PEGS4 cross section data for various materials included in BEAMnrc, custom material files were created following material specifications of the data package. Elimination of some obvious errors, discrepancies and deficiencies in the MC data package required interpretation and added additional degrees of freedom to the model.

After an iterative initial electron beam parameter tuning process, the initial electron beam was selected to be of circular shape with a Gaussian intensity distribution of 0.6 mm FWHM and 0.7 mm FWHM, for the 9 and 16 MeV beams respectively. The initial electron beam energy spectrum was assumed to be Gaussian with mean energies 9.97 and 17.69 MeV and 3% FWHM spread at the X-ray target level in the treatment head. No variance reduction techniques were used. The number of particle histories was 800 x 10^6 per simulation for each energy and the resulting particle data were collected into a phase space file at 100 cm SSD. The following EGSnrc parameters were used in all simulations: *ECUT* = *AE* = 0.521 MeV; *PCUT* = *AP* = 0.01 MeV; *ESTEPE* = 0.25; *XIMAX* = 0.5; *Boundary crossing algorithm* = *EXACT*; *Skin depth for BCA* = 3; *Electron-step algorithm* = *PRESTA-II*; *Spin effects* = *On*; *Brems angular sampling* = *KM*; *Brems cross sections* = *NIST*; *Bound Compton scattering* = *norej*; *Compton cross sections* = *default*; *Pair angular sampling* = *KM*; *Pair cross sections* = *BH; Photoelectron angular sampling* = *On; Rayleigh scattering* = *On; Atomic relaxations* = *On; Electron impact ionization* = *On; Photon cross sections* = *xcom* [26][27].

The above-discussed phase space data was used as input for dose calculations in the phantoms, applying the DOSXYZnrc code. At each beam energy, the number of particle histories was 1.5 x 10^9 per simulation, which required the particles to be recycled several times. The sizes of the calculation voxels were adapted to be smaller in regions of high dose gradients. In order to maintain high resolution throughout the depth dose and profile curves, the voxel sizes were varied between 0.1 and 0.2 cm. Over regions of interest, the MC calculation voxel sizes were comparable to the calculation grid sizes applied in the GGPB and eMC algorithms. The random nature of particle transport is expressed by determining statistical uncertainties for the calculated dose values within each voxel. In BEAMnrc and DOSXYZnrc simulations the values are calculated using the history-by-history method [28]. These relative errors were typically less than 0.2%, but somewhat exceeded this value near the surface along the Z-axis and at distal ends of the profiles. The

EGSnrc parameters were those used in the treatment head simulations. Phantoms similar to those created for the TPS algorithms were created within the DOSXYZnrc, using PEGS4 cross-section data for various materials (*VACUUM, AIR521ICRU* and *H20521ICRU*). The *LUNG521ICRU* data were modified to match the mass density of the lung material used in the eMC calculations. The initial electron beam tuning process and beam parameter selection are discussed elsewhere [29][30][31][32][33]. As a result of the tuning process (Ojala et al 2010 [29]), when comparing results of PDD measurements in water to MC model calculations, the maximum relative differences at depths beyond the depth of dose maximum (d_{max}) were 0.7% and 0.4%, for the 9 and 16 MeV beams, respectively. In profiles at d_{max} (2.0 and 3.0 cm for 9 and 16 MeV beams, respectively) the maximum distance to agreement (DTA) values in the penumbrae were 0.6 and 0.4 mm, average dose differences in the high dose region were 0.2% and 0.2%, and average dose differences in out-of-field regions were 0.2% and 0.4% for the 9 and 16 MeV beams, respectively. For this study, sets of dose distribution data similar to those obtained using the commercial TPS algorithms were extracted for comparison.

The MC dose calculation in the Rando-Alderson™ phantom was carried out for a 16 MeV electron beam with an A15 applicator (which had been earlier used in measurements [17]), and SSD = 100 cm in a CT-based phantom geometry reconstructed from a set of 3 mm-thick CT slices with the CTCREATE code in DOSXYZnrc. The CT number-to-material and mass density conversion curve were defined using the RMI Gammex 467 Tissue Characterization Phantom (Middleton, WI, USA) and PEGS4 cross-section data for Rando-Alderson™ lung and tissue materials [34].

2.3. Comparative measurements and methods of data analysis

Measurements to verify the P1 phantom calculations were performed using an ionization chamber (IC) in a MP3 water phantom with a scanning system (PTW Freiburg GmbH, Germany). The PDD curve was established according to the IAEA TRS 398 protocol [35] using a PTW 34001 Roos parallel plate ionization chamber of 0.35 cm^3 volume, with an empirically corrected effective point of measurement (EPOM). The depth-dose distribution over the build-up region and the R_{50} depth (depth at which 50% of relative dose is deposited) were point-verified in solid water with Gafchromic® EBT radiochromic film. The PDD curves were also used as a part of configuration data for eMC and GGPB in the Eclipse™ TPS.

Measurements in the anthropomorphic Rando-Alderson™ phantom were performed in the thorax section of this phantom at eleven selected positions in the lung and the mediastinum regions (figure 6(e)), where TLD detectors ($Li_2B_4O_7$:Mn,Si) were placed. The TLD detectors were calibrated using a 6 MV photon beam in a solid water phantom at the depth of dose maximum. The detailed procedure of TLD measurements is described elsewhere [17]. At selected points within the phantom slice, three stacked TLD detectors were placed centrally in the 5 mm diameter holes, and held in place by tissue-equivalent rods [17]. The TLD-measured point dose values were based on mean values of two independent exposures of the Rando-Alderson™ phantom. Over the electron beam energy range 4-16 MeV, the measured intrinsic energy dependence (or relative effectiveness) of $Li_2B_4O_7$:Mn,Si TLD detectors (with respect to absorbed dose in water of 6 MV photons), remains within 1.03 ± 0.02 [36], obviating the need to introduce any electron energy correction to the TLD readouts.

The data were analysed and plotted using a custom-made VBA-based code operating within the Microsoft Excel 2003 (Redmond, Washington, USA) spread-sheet application. For dose comparisons concerning the P1 phantom, the MC-calculated PDDs were normalized to coincide with the measured PDD curves at d_{max}. For dose comparisons in the P2 and P3 phantoms the above-determined P1 phantom normalization factors were used. The VBA-based code was also used to calculate relative differences between dose values from the data sets compared.

3. Results

3.1. Homogeneous phantom (P1)

Measurements of the PDD curves were performed as a combination of film point measurements over the dose build-up region and measurements using a parallel plate ionization chamber with corrected EPOM. Results of these measurements served as accurate configuration data for the commercial algorithms and as reference data for the MC model. The PDD curves, normalized to 100% at d_{max}, are shown in figure 2 for 9 MeV and in figure 3 for 16 MeV electron beams. The overall agreement between the different calculation models and measurements is good. The accuracy of the MC beam model with A15 applicator size (used for phantom P4) was confirmed in exactly the same manner as that used for the A20 applicator, with identical results (not shown).

FIGURE 2

FIGURE 3

3.2. Heterogeneous phantom (P2)

In calculations performed for the P2 heterogeneous phantom, the results of the MC calculation were considered as reference, since no measured data were available. Over the heterogeneity region the MC results show more detail in the PDD than do the eMC or GGPB results, which is due to the dose calculation principles and to differences in grid sizes. For the 9 MeV beam (figure 2), overestimation by the eMC algorithm of the dose in the lung-equivalent material increases with increasing depth, the largest discrepancy, of about 5.0% of dose at d_{max} (D_{max}), occurring at the depth of 7.0 cm. The 9 MeV GGPB calculation produces a PDD curve closely matching that calculated by the MC code. For the 16 MeV beam (figure 3), the GGPB calculation produces a PDD curve with irregularities in the lung-equivalent material, and dose values are lower by about 5.0% of D_{max} throughout the PDD curve excluding the photon "tail". The 16 MeV eMC calculation produces a PDD curve closely matching that calculated by the MC code.

3.3. Heterogeneous phantom (P3)

The results of eMC, GGPB and MC calculations in the P3 phantom are shown in figure 4 for 9 MeV and in figure 5 for 16 MeV beams. Depths of profiles in the CAX plane are chosen so that curves intersect at locations of largest differences between results of eMC and GGPB calculations. The profiles in the CAX plane are at depths of 4.4 and 5.2 cm for 9 MeV and 7.4 and 10.0 cm for 16 MeV beams. The depths are stated with the respective bolus thicknesses included. For results concerning the P3 phantom, the output of MC calculations serves as reference, as was the case for the P2 phantom.

For the 9 MeV beam (figure 4) the dose profiles calculated with the eMC code show similar shapes as those calculated by MC, but in the lung-equivalent material the dose values calculated by the eMC code are 3-5% of D_{max} higher than the reference results of MC calculations. In the profile at shallower depth the eMC code results overestimate the dose also over the water-equivalent part, by up to about 4% of D_{max}. In the results of the GGPB calculation the presence of heterogeneity correction leads to a dose distribution closer to the MC results, compared to results obtained from eMC calculations over regions where the dose gradient is small, i.e., further away from the material boundary. In the vicinity of the material boundary (figure 4) some deviations are seen in the GGPB results - over the lung-equivalent region, the GGPB-calculated dose is 6-12% of D_{max} lower than in the MC-calculated dose profile, and over the water-equivalent region it is higher by about 12% of D_{max}.

FIGURE 4

For the 16 MeV beam results (figure 5) the dose profiles calculated with the eMC code again show similar shapes to those calculated using the MC code, but in the lung-equivalent material the eMC-calculated dose is 3-5% of D_{max} higher than that resulting from MC calculations. The GGPB-calculated profile shapes differ from those calculated by MC and eMC codes, with matching dose values at certain points, but generally either under- or over-estimating the dose against the MC results, especially in profile shoulders calculated over regions close to the material boundary (figure 5). In the lung-equivalent material the GGPB-calculated

dose is lower that calculated by the MC code, by 3-14% of D_{max}. Over the water-equivalent part, in the profile at larger depth, this overestimation exceeds 15% of D_{max}.

FIGURE 5

3.4. Rando-Alderson™ anthropomorphic phantom (P4)

Results of MC calculations performed for the 16 MeV beam with an A15 applicator served here as reference, together with results of in-phantom TLD measurements. The numbered positions of TLDs inside the anthropomorphic phantom are shown by white dots in figure 6(e). Four PDD curves calculated using the MC, eMC and GGPB codes were extracted for comparison. The PDD distributions were calculated over axes parallel to the CAX, offset along the central plane of the thorax segment of the Rando-Alderson™ anthropomorphic phantom to intersect the measurement positions of TLD detectors located inside the phantom. The calculated PDD curves and TLD-measured point doses (6 TLD readouts per point), together with their error bars (1 SD), are shown in figures 6(a)-6(d).

It can be seen in figures 6(a)-6(d) that the MC-calculated dose distribution generally coincides with results of TLD measurements (within their error bars) at selected points, with a few exceptions, as seen in figure 6(b) and figure 6(c).

Comparing the dose distributions calculated by the eMC and GGPB codes against reference MC-calculated and TLD-measured distributions, we observe better congruence of eMC results than of those calculated using the GGPB algorithm. In general, within statistical uncertainties of results of the two MC-based algorithms, the eMC calculations slightly overestimate the reference PDDs, by no more than 5% of D_{max} (the maximum overestimation at depth of 4.5 cm in figure 6(b)). In many regions the GGPB calculation underestimates the reference PDDs, especially in the lung (by up to 15% of D_{max}), but gives more accurate results in the tissue-equivalent part of the anthropomorphic phantom (figure 6(d)). In the dose-volume histogram (DVH) for the lung in the phantom, assuming the prescribed dose of 50 Gy to be 100%, V_{20Gy} values (volume fraction with absorbed dose higher than 20 Gy) were 23.3% and 28.2% for the GGPB and eMC, respectively. No tools to extract "reference" organ-specific DVH data from the MC calculations were available.

FIGURE 6

4. Discussion

In this study, comparisons in the P1 water phantom showed that the GGPB and eMC algorithms implemented in the Varian Eclipse™ TPS produced PDD curves which agreed very well with those measured and calculated with the MC code. The P2 phantom (slab geometry) was designed to study in more detail the manner in which the heterogeneity is handled by GGPB and eMC algorithms. In the P2 phantom geometry, the MC code and the eMC algorithm calculate dose-to-medium (lung), while the GGPB algorithm calculates dose-to-water. The difference in the absorbed dose calculation between the two approaches is thus related to the manner in which the water-to-lung stopping power ratio is accounted for. For this reason the GGPB-calculated dose in the lung is lower, the difference at the water-lung interface being approximately 3% of D_{max}. This feature of the GGPB code has also been reported by Ding et al. [23]. The most probable energy of the electrons at the depth of the lung-water interface z_i, may be approximated by $E_{p,0}(z_i) = E_{p,0}\,(1 - z_i / R_p)$, resulting in 2.6 and 7.3 MeV for the nominal beam energies of 9 and 16 MeV, respectively [21]. For the 9 MeV electron beam the water-to-medium stopping power ratio increases from 0.97 to unity over a short range of z, as $E_{p,0}(z)$ decreases from 2.6 MeV to zero, making the difference between dose-to-medium and dose-to-water values negligible [37]. For the 16 MeV beam the difference persists over a broader range of z in the lung.

In the results of the P2 phantom calculations for the 9 MeV beam over the lung part (figure 2), the GGPB- and MC-calculated PDD curves agree, while the eMC-calculated PDD exceeds them, the difference increasing towards the end of the electron range. This might be caused by the slightly different values of stopping power used in these calculations, though the difference between the standard lung mass density

(0.30 g cm^{-3}) used in eMC calculations and the mass density used in this study is small (by 0.02 g cm^{-3}). A similar overestimation of the absorbed dose in the lung by the eMC algorithm, especially at 9 MeV, but not for 6, 12 and 18 MeV beams, has been reported by Aubry et al. [20], where a considerably lower value of lung mass density (0.21 g cm^{-3}) was used. For the 16 MeV beam, immediately after the water-lung interface, the dose difference between the GGPB-calculated PDD curve and the MC- and eMC-calculated curves is explained by the dose-to-water vs. dose-to-medium difference between the calculations, but the relative difference between those results diminishes as the absolute dose decreases. With increasing depth the energy of electrons in the beam diminishes and consequently, the stopping power ratio approaches unity. Taking into account the dose-to-water vs. dose-to-medium difference, the GGPB-calculated curve agrees with those calculated by eMC and MC, to within the above-estimated uncertainty, except for the underestimation at larger depths.

In the more clinically relevant half-slab P3 phantom geometry, which also included boluses of appropriately chosen thicknesses, the differences between results of calculations are more evident. The relative dose is notably higher in the material of lower mass density, since more scattering occurs in the adjacent higher mass density material. The “surplus dose”, due to lateral scattering close to the water-lung interface is then deposited within the lower mass density material. When comparing the results of eMC and GGPB calculations, on the lung-equivalent side the dose distributions further away from the interface match fairly well, showing differences similar to those observed in the P1 or P2 phantoms. However, close to the lung-water interface and to the midline of the phantom, the differences are quite large. In the results for the 16 MeV beam the GGPB algorithm markedly underestimates the dose in the lung. This effect is less visible in the profile at larger depth. The reason for this discrepancy is due to the GGPB algorithm overestimating the energy scattered from the lung to the water-equivalent part. In turn, the dose distribution calculated by the GGPB algorithm on the water-equivalent side at depths larger than the practical beam range in water, is grossly overestimated. This is again due to the above-mentioned GGPB-assumed lateral scattering from the lung-equivalent side. Results of P3 calculations for the 9 MeV beam demonstrate similar features with respect to regions of over- and underestimation in the GGPB-calculated depth-dose dependences, except that the distances to which these differences persist are approximately half of those seen in the 16 MeV beam results, due to the shorter range of lateral scatter in a 9 MeV electron beam. For both beam energies the limited size of the phantom may result in inaccurately calculated dose distributions over the penumbra region, but this is not considered here.

For the 16 MeV beam, the eMC-calculated dose to the lung in the P3 phantom is slightly higher than that calculated by the MC code, while in the slab geometry (P2 phantom) both codes produced identical results. This may result from the different approaches taken in the two codes to account for large-angle scatter from the water-equivalent side. Most likely, by the same mechanism, over regions far from the interface the GGPB algorithm calculates higher doses to the lung than does the MC code. At the lung-water interface in the P3 phantom the dose values calculated by the three codes agree very well at both beam energies.

The choice of 16 MeV electron beam energy to treat the Rando-Alderson™ anthropomorphic phantom may be somewhat excessive of the typical energy of such beams used clinically. However, this choice was made for easier comparison with results of our calculations in virtual phantoms. We note the difference in electron beam applicators (A15, versus A20 in the virtual phantom calculations), resulting from experimental considerations. When analysing TLD results, we note that the TLD pellets of 4.5 mm diameter and 3 x 0.8 mm thickness were oriented with their axes perpendicular to the beam direction [17]. Since the TLD-read dose value is taken to be measured at the central point of the TLD assembly and the TLD readout of each of the three pellets in the assembly represents the absorbed dose averaged over their respective volumes, some discrepancy may be expected if the TLD pellet assemblies are exposed in regions of large dose gradients. The TLD measurements in the anthropomorphic phantom confirm that dose in the lung is underestimated by the GGPB algorithm, while the dose distributions calculated by eMC and MC codes and measured by TLDs agree very well. The underestimation of the dose distribution by the GGPB algorithm over the lateral part of the lung seen in figure 6(a), is also quite large due to the closeness of the lateral edge of the lung. As shown in figure 6(b), similar underestimation is seen over the medial part of the lung. The "full" MC calculation shows the dose distribution in much more detail, including modifications by other heterogeneities, such as bones. The commercial algorithms do not show such detail, partly due to the larger voxel size applied in their

calculations. In the mediastinum (figure 6(d)) all methods of dose calculation show similar results, except for the GGPB algorithm, which overestimates the dose beyond the maximum electron range. Along the TLD positions which lie very close to the lung-mediastinum interface (figure 6(c)) the GGPB calculation also underestimates the dose while, according to results of P3 phantom calculations, good agreement could be expected, as all calculations gave the same results in this region (figure 5). The GGPB algorithm discrepancy may be due to the slight divergence of the electron beam at these points. Underestimation of the dose by GGPB algorithm resulted in a DVH-calculated V_{20Gy} value lower by 4.9 %, compared to that obtained from eMC calculations (V_{20Gy}= 23.3% versus 28.2% for the GGPB and eMC calculations, respectively). Since the eMC-calculated PDD curves in the phantom were nearly congruent with the MC calculation, the observed differences in the GGPB- and eMC-calculated DVHs may be clinically relevant, despite the somewhat artificial geometry of the P3 phantom. The close agreement, within measurement uncertainties, of the TLD measurements with results of MC calculations, attests to TLD measurements being a reliable method for dose measurements in the lung region of the anthropomorphic phantom, at least at higher electron beam energies. For reasons discussed earlier, over regions of steep dose gradients characteristic of electron beams of lower energies, evaluation of absorbed dose at the central point of the TLD detector assembly placed inside the anthropomorphic phantom may be burdened by a higher uncertainty.

In general, our results agree with those of Coleman et al. [19] who compared dose distributions in the lung calculated by the pencil beam algorithm against MC computations for 12 MeV electron beams. They concluded that the pencil beam calculation tended to underestimate the penetration of the electron beam in the lung, and that the calculated dose to the lung and the heart was underestimated. Ding et al [12] compared eMC-calculated dose distributions from 9 and 18 MeV electron beams, to measurements in water and around a 1 cm thick slab of lung placed at 1 cm depth and extending from the CAX outwards. Their results showed the dose-to-water vs. dose-to-lung difference more clearly because the comparison was made at a shallow depth, where the energy is higher and the water/lung stopping power ratio further deviates from unity. They also showed that the modification of the dose distribution below the lung slab due to its presence is accurately calculated by the eMC algorithm. However, the test arrangement, where the lung slab is close to the surface does not represent the lung-mediastinum interface. For the anthropomorphic geometry Aubry et al. [20] reported the largest discrepancy between eMC calculations and film measurements occurring at the lung-mediastinum interface beyond the depth of electron range in water. This discrepancy was largest for 9 MeV electron beams. As seen in figure 4, our results support these conclusions. However, the normalization procedure used by Aubry et al. [20] does not necessarily give the absolute difference accurately enough.

The clinical implications of the observed discrepancies between dose distributions calculated by different algorithms are relevant mainly to chest wall irradiation associated, e.g., with post-mastectomy breast cancer radiotherapy (where the chest-wall thickness is typically lower, so electron beams of lower energies need to be used) or to boost electron therapy (where the thickness of the breast tissue is typically larger, and part of the chest wall is included in the PTV, requiring the use of electron beams of higher energies). In these techniques the anterior electron field may extend over the mediastinum and the lung-mediastinum interface is over some depths close to being parallel to the direction of the beam. The outcome is that the GGPB algorithm will underestimate the dose to the lung close to the mediastinum, which may have a slight effect on the calculated DVH, by lowering the average dose. Underestimation of dose to the lung in our slab geometry at higher electron beam energies would have a similar effect. At the high electron beam energy of 16 MeV this effect of underestimation is quite evident, but it may also be seen at the lower electron beam energy (9 MeV), yet confined to a shorter range and smaller volume in the lung. Underestimation of the dose in the lung by the GGPB algorithm would imply that if similar DVH constraints (e.g. for V_{20Gy}) were applied in planning with both algorithms, the dose delivered to the lung would be higher if the GGPB algorithm is applied. The dose very close to the lung-mediastinum interface where, e.g., the coronary arteries are located, would be fairly correctly estimated by either algorithm. With respect to the dose to the myocardium, the GGPB algorithm clearly overestimates it, as shown in figures 4 and 5. The eMC algorithm calculates the dose close to the interface with better accuracy, especially over the water-equivalent side, but gives slightly higher dose values in the lung (by some 3-5%), compared to the reference MC calculations.

5. Conclusions

The dose distributions calculated by the eMC code in the phantom geometries used in this study were close to those resulting from MC calculations, the eMC code slightly overestimating the dose in the lung-equivalent tissue. In chest wall electron beam therapy, the known differences in the heterogeneity and lateral scattering calculations present in the GGPB code may lead to significant underestimation of the actual dose delivered to the lung, and to overestimation of the dose to the mediastinum at certain depths. This may affect the optimization of such plans in terms of DVHs over volumes close to the lung-mediastinum interface, such as the myocardium or coronary arteries. Good agreement between TLD measurements and BEAMnrc calculations in the anthropomorphic phantom attests to the accuracy of this "full" MC code and its applicability as a reference for benchmarking codes used in commercial radiotherapy planning systems.

Acknowledgements

This study was supported by the Pirkanmaa Hospital District Elna Kaarina Savolainen Fund (Grant No. 145211).

Conflict of interest statement

The authors declare that they have no conflicts of interest. The authors alone are responsible for the content and writing of the paper.

References

[1] Hogstrom KR, Almond PR. Review of electron beam therapy physics. Phys Med Biol 2006;51:R455-R89.

[2] Lax I. Development of a generalized Gaussian model for absorbed dose calculation and dose planning in therapeutic electron beams. Ph.D. Thesis. University of Stockholm 1986.

[3] Hogstrom KR, Mills MD, Almond PR. Electron beam dose calculation. Phys Med Biol 1981;26:445-59.

[4] Boyd RA, Hogstrom KR, Starkschall G. Electron pencil-beam redefinition algorithm dose calculations in the presence of heterogeneities. Med Phys 2001;28:2096-104.

[5] Neuenschwander H, Mackie TR, Reckwerdt PJ. MMC - A high-performance Monte Carlo code for electron beam planning. Phys Med Biol 1995;40:543-74.

[6] Janssen JJ, Korevaar EW, van Battum LJ, Storchi PR, Huizenga H. A model to determine the initial phase space of a clinical electron beam from measured beam data. Phys Med Biol 2001;46:269-86.

[7] Kawrakow I, Fippel M, Friedrich K. 3D electron dose calculation using a Voxel based Monte Carlo algorithm (VMC). Med Phys 1996;23:445-57.

[8] Kawrakow I. VMC++, electron and photon Monte Carlo calculations optimized for radiation treatment planning. Proc. Monte Carlo 2000 Meeting, Lisbon, Portugal, 2000.

[9] Reynaert N, van der Marck SC, Schaart DR, Van der Zee W, Van Vliet-Vroegindeweij C, Tomsej M, Jansen J, Heijmen B, Coghe M, De Wagter C. Review: Monte Carlo treatment planning for photon and electron beams. Radiat Phys Chem 2007;76:643-86.

[10] Chetty IJ et al. Report of the AAPM Task Group 105: Issues associated with clinical implementation of Monte Carlo-based photon and electron external beam treatment planning. Med Phys 2007;34:4818-53.

[11] Ding GX, Cygler JE, Yu CW, Kalach NI, Daskalov G. A comparison of electron beam dose calculation accuracy between treatment planning systems using either a pencil beam or a Monte Carlo algorithm. Int J Radiat Oncol Biol Phys 2005;63:622-33.

[12] Ding GX, Duggan DM, Coffey CW, Shokrani P, Cygler JE. First macro Monte Carlo based commercial dose calculation module for electron beam treatment planning--new issues for clinical consideration. Phys Med Biol 2006;51:2781-99.

[13] Tertel J, Wulff J, Karle H, Zink K. Verification of a commercial implementation of the Macro Monte Carlo electron dose calculation algorithm using the virtual accelerator approach. Z Med Phys 2010;20:51-60.

[14] Glegg MM. Electron dose calculations: a comparison of two commercial treatment planning computers. Med Dosim 2003;28:99-105.

[15] Cygler JE, Daskalov GM, Chan GH, Ding GX. Evaluation of the first commercial Monte Carlo dose calculation engine for electron beam treatment planning. Medy Phys 2004;31:142-53.

[16] Samuelsson A, Hyödynmaa S, Johansson K-A. Dose accuracy check of a 3D electron beam algorithm in a treatment planning system. Phys Med Biol 1998;43:1529-44.

[17] Waligórski MPR, Baranczyk R, Hyödynmaa S, Eskola J, Lesiak J, Rozwadowska-Bogusz B, Kołodziejczyk A. A TL-based anthropomorphic benchmark for verifying 3-D dose distributions from external electron beams calculated by radiotherapy treatment planning systems. Radiat Prot Dosimetry 2006;120:74-7.

[18] Seuntjens J, Van der Plaetsen A, Thierens H. Comparison of measured and calculated dose distributions in lung after electron beam treatment of the chest wall. Med Phys 1994;21:1959-68.

[19] Coleman J, Park C, Villarreal-Barajas JE, Petti P, Faddegon B. A Comparison of Monte Carlo and Fermi-Eyges-Hogstrom estimates of heart and lung dose from breast electron boost treatment. Int J Radiat Oncol Biol Phys 2005;61:621-8.

[20] Aubry J-F, Bouchard H, Bessières I, Lacroix F. Validation of an electron Monte Carlo dose calculation algorithm in the presence of heterogeneities using EGSnrc and radiochromic film measurements. J App Clin Med Phys 2011;12:2-14.

[21] International Commission on Radiation Units and Measurements (ICRU). Radiation Dosimetry: Electron Beams with Energies Between 1 and 50 MeV, ICRU Report 35. 1984.

[22] Popple RA, Weinberg R, Antolak JA, Ye S-J, Pareek PN, Duan J, Shen S, Brezovich IA. Comprehensive evaluation of a commercial macro Monte Carlo electron dose calculation implementation using a standard verification data set. Med Phys 2006;33:1540-51.

[23] Ding GX, Cygler JE, Zhang GG, Yu MK. Evaluation of a commercial three-dimensional electron beam treatment planning system. Med Phys 1999;26:2571-80.

[24] Rogers DWO, Faddegon BA, Ding GX, Ma CM, We J, Mackie TR. BEAM: a Monte Carlo code to simulate radiotherapy treatment units. Med Phys 1995;22:503-24

[25] Varian Medical Systems. Monte Carlo Data Package - High Energy Accelerator. Confidential Report. 2009.

[26] Rogers DWO, Walters B, Kawrakow I. BEAMnrc User's Manual. NRCC Report PIRS-0509(A)revK. 2009.

[27] Kawrakow I, Mainegra-Hing E, Rogers DWO, Tessier F, Walters BRB. The EGSnrc Code System: Monte Carlo Simulation of Electron and Photon Transport. NRCC Report PIRS-0701. 2009.

[28] Walters BRB, Kawrakow I, Rogers DWO. History by history statistical estimators in the BEAM code system. Med Phys 2002;29:2745-2752.

[29] Ojala J, Hyödynmaa S, Pitkänen M. BEAMnrc Monte Carlo modelling of linear accelerator using parallel computing grid - validation of a common, fixed geometry model for photon and electron beams. Proc. of XVIth ICCR, Amsterdam, Netherlands, 2010.

[30] Antolak JA, Bieda MR, Hogstrom KR. Using Monte Carlo methods to commission electron beams: A feasibility study. Med Phys 2002;29:771-86.

[31] Bieda MR, Antolak JA, Hogstrom KR. The effect of scattering foil parameters on electron-beam Monte Carlo calculations. Med Phys 2001;28:2527-34.

[32] Huang VW, Seuntjens J, Devic S, Verhaegen F. Experimental determination of electron source parameters for accurate Monte Carlo calculation of large field electron therapy. Phys Med Biol 2005;50:779-86.

[33] Verhaegen F, Mubata C, Pettingell J, Bidmead AM, Rosenberg I, Mockbridge D, Nahum AE. Monte Carlo calculation of output factors for circular, rectangular, and square fields of electron accelerators (6–20 MeV). Med Phys 2001;28:938-49.

[34] Walters B, Kawrakow I, Rogers DWO. DOSXYZnrc User's Manual. NRCC Report PIRS-0794revB. 2007.

[35] Andreo P, Burns DT, Hohlfeld K, Huq MS, Kanai T, Laitano F, Smyth VG, Vynckier S. IAEA International Atomic Energy Agency. Absorbed Dose Determination in External Beam Radiotherapy: An International Code of Practice for Dosimetry Based on Standards of Absorbed Dose to Water. Technical Reports Series no. 398. 2004.

[36] Nahajowski D, Góra E, Rozwadowska-Bogusz B, Lesiak J, Polak, B, Kabat D, Zawadzki P, Waligórski MPR. Evaluation of the relative effectiveness of LiF-based TL detectors for electron radiotherapy beams over the energy range 6-20 MeV. Radiat Meas 2008;43:879-82.

[37] International Commission on Radiation Units and Measurements (ICRU). Photon, Electron, Proton and Neutron Interaction Data for Body Tissues, ICRU Report 46. 1992.

Figure captions

Figure 1. The P3 phantom: A semi-infinite lung-equivalent slab is immersed in a water-equivalent phantom at the depth of 3 cm (9 MeV beam) (a) or 4.5 cm (16 MeV beam) (b), extending from the wall of the phantom to the CAX. Locations of planes selected for calculating profiles chosen for comparison, are also shown. The length of the side of the phantom not shown in the figure is 24 cm, in both cases.

Figure 2. PDD curves for the 9 MeV electron beam at the CAX in the P1 phantom, calculated by: MC (blue, solid line), eMC (purple, circles) and GGPB (green, triangles) algorithms and results of measurements (asterisks). Also shown are results calculated at CAX in the P2 phantom, by MC (blue, solid line), eMC (purple, circles) and GGPB (green, triangles) algorithms. The vertical boundary at depth 3 cm indicates the surface of the lung slab in phantom P2.

Figure 3. PDD curves for the 16 MeV electron beam at the CAX in the P1 phantom, calculated by: MC (blue, solid line), eMC (purple, circles) and GGPB (green, triangles) algorithms, and results of measurements (asterisks). Also shown are results calculated at CAX in the P2 phantom, by MC (blue, solid line), eMC (purple, circles) and GGPB (green, triangles) algorithms. The vertical boundary at depth 4.5 cm indicates the surface of the lung slab in phantom P2.

Figure 4. Dose profiles for the 9 MeV beam through the CAX in the P3 phantom at depths 4.4 and 5.2 cm, calculated by the MC (blue, solid line), eMC (purple, circles) and GGPB (green, triangles) algorithms.

Figure 5. Dose profiles for the 16 MeV beam through the CAX in the P3 phantom at depths 7.4 and 10.0 cm, calculated by MC (blue, solid line), eMC (purple, circles) and GGPB (green, triangles) algorithms.

Figure 6(a)-(e). PDD curves along axes parallel to the CAX, offset along the central plane of the thorax segment of the Rando-Alderson^{TM} anthropomorphic phantom (P4) to intersect the measurement positions of TLD detectors located inside the phantom, shown in (e). The PDD curves shown were calculated by MC (blue, solid line), eMC (purple, circles) and GGPB (green, triangles) algorithms. The point dose values (red, diamonds), shown with their error bars, are based on TLD-measurements at point locations shown (e).

Figure1a_1b_color

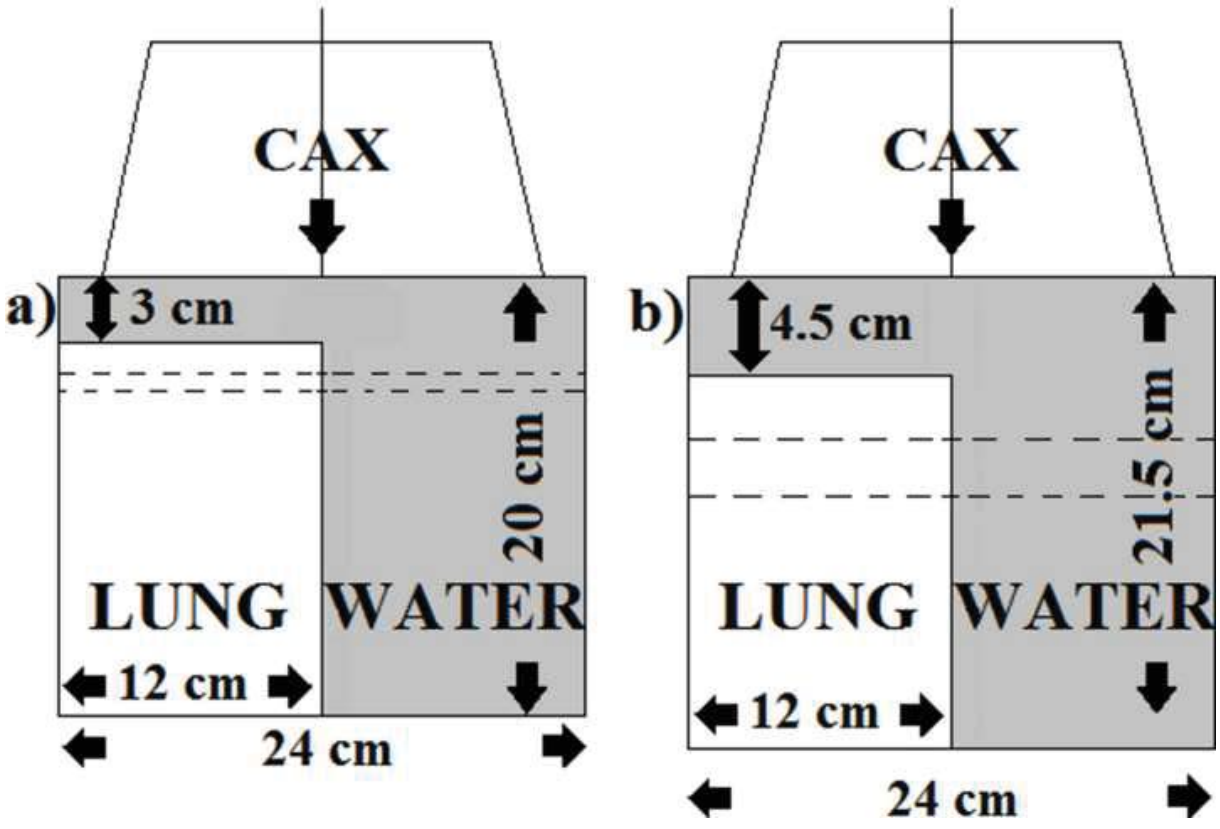

Figure2_color

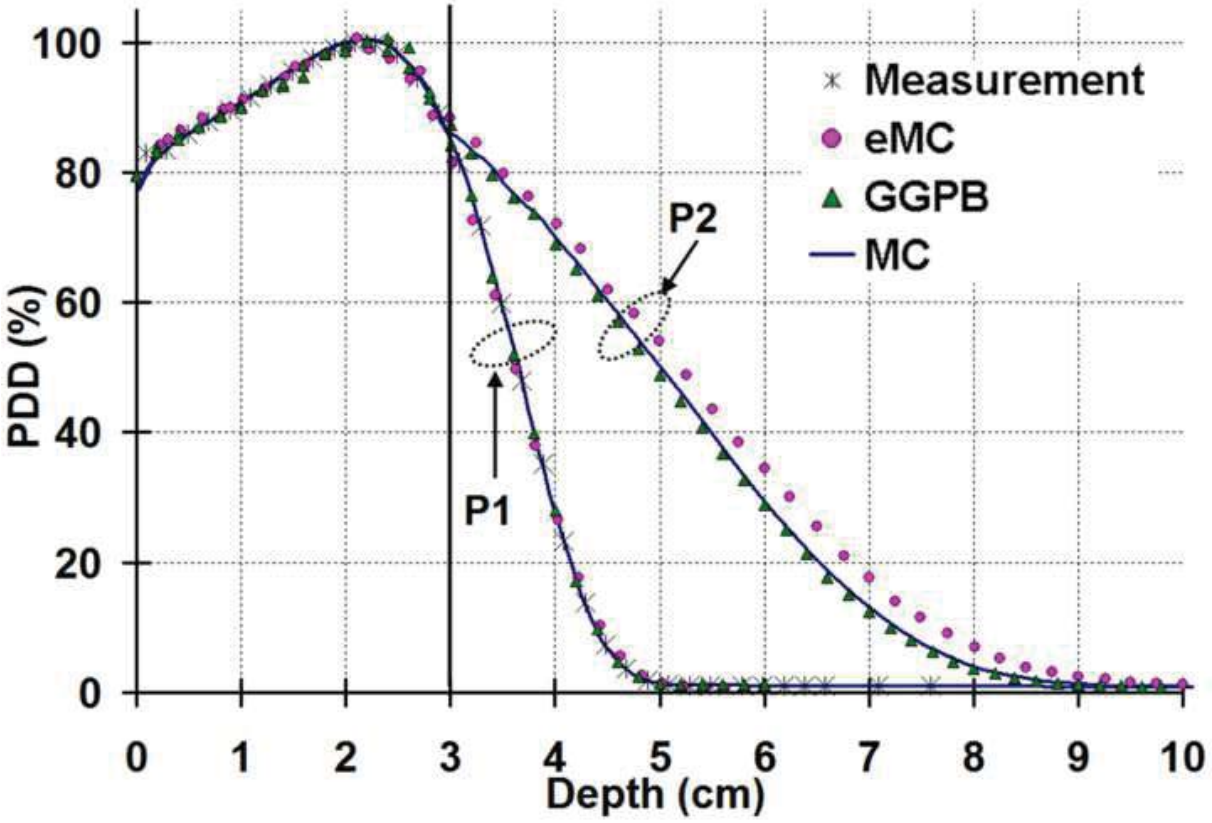

Figure3_color

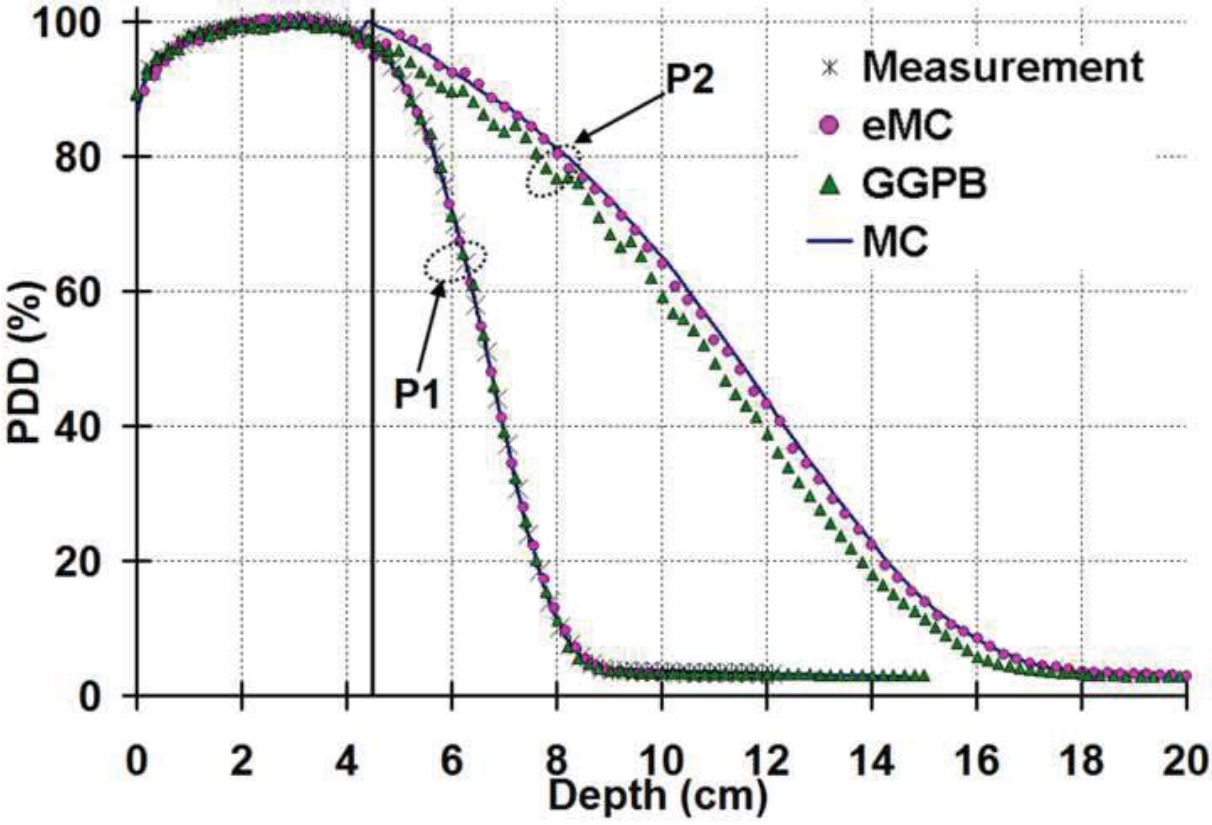

Figure4_color

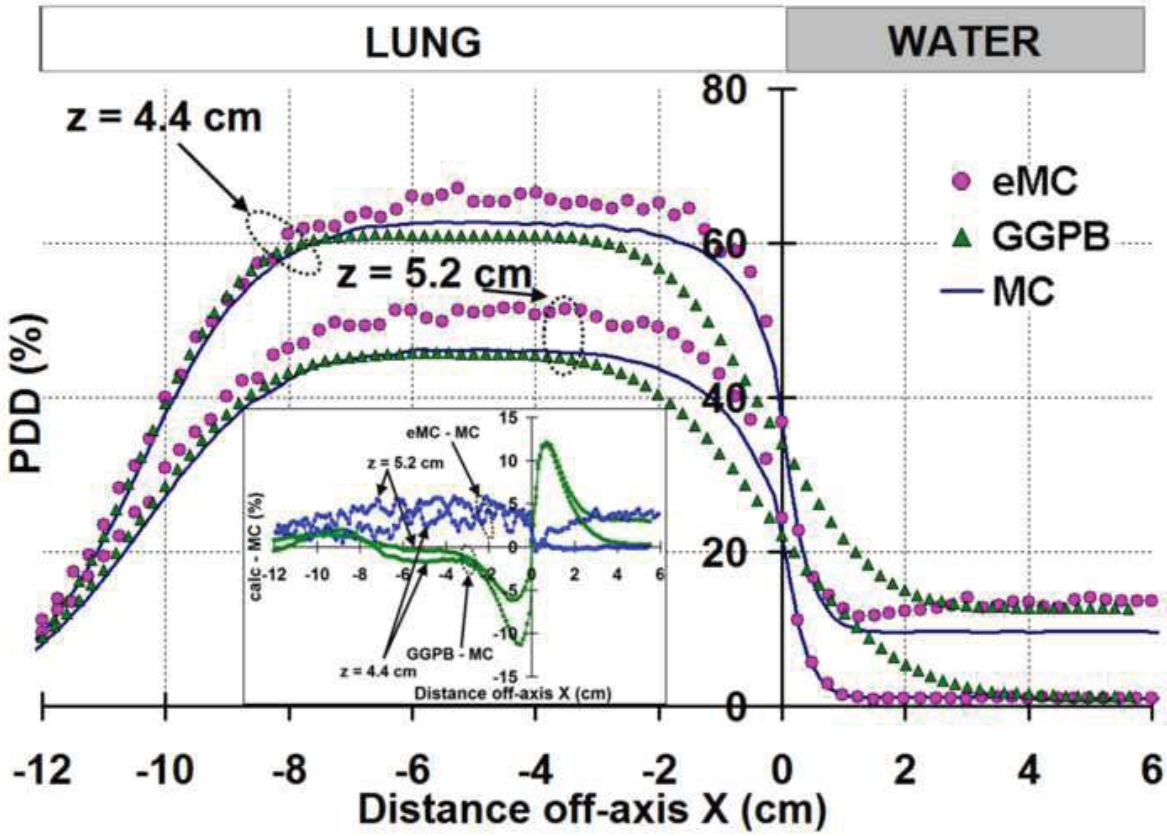

Figure5_color

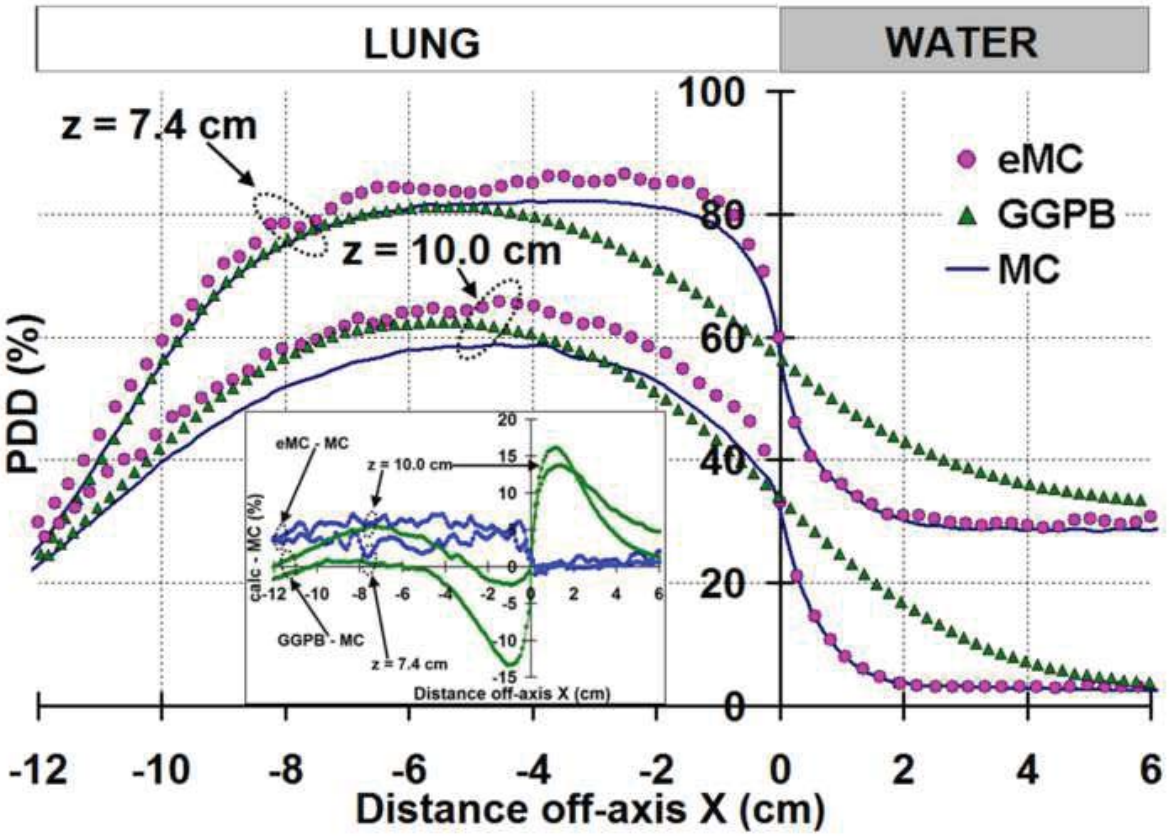

Figure6a_6e_color

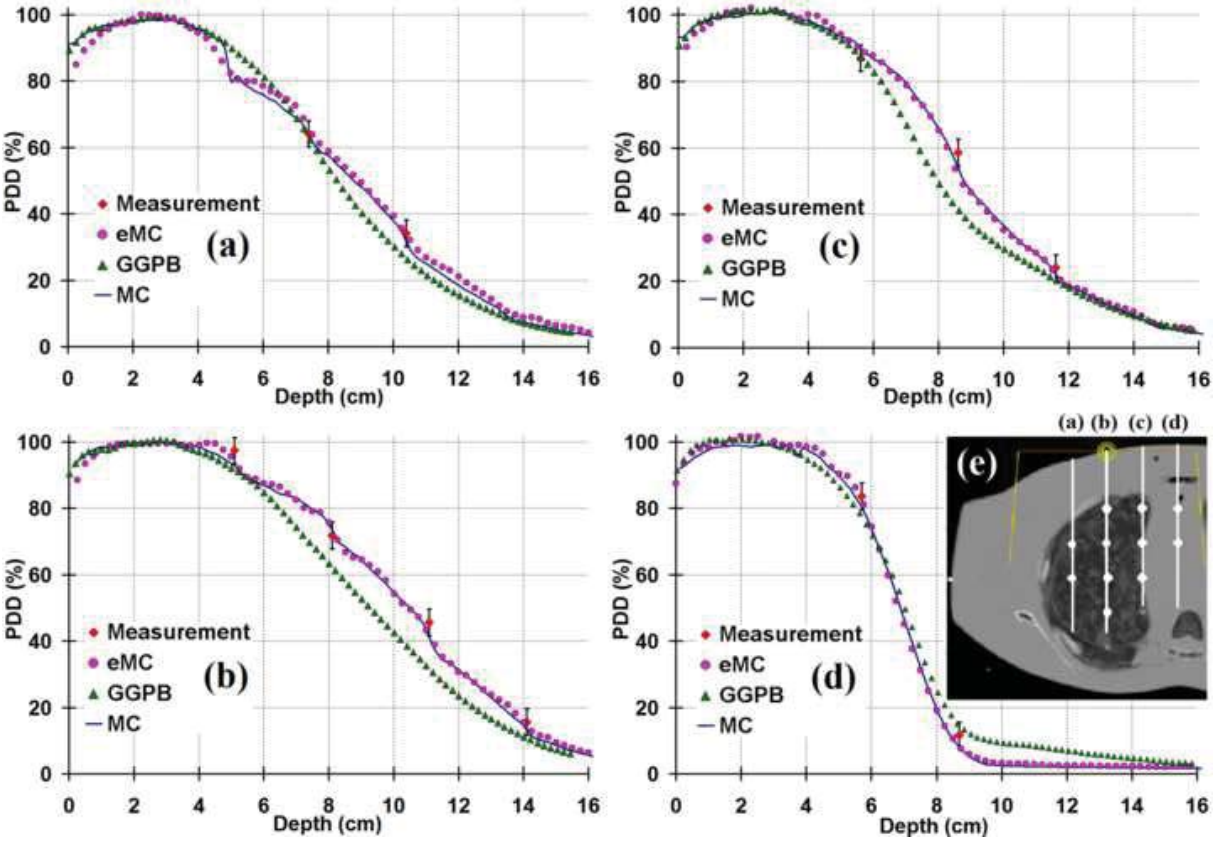

Tampereen teknillinen yliopisto
PL 527
33101 Tampere

Tampere University of Technology
P.O.B. 527
FI-33101 Tampere, Finland

ISBN 978-952-15-3317-4
ISSN 1459-2045